Diss. ETH No. 14833

Detection of defects in cylindrical structures using a time reverse numerical simulation method

A dissertation submitted to the
SWISS FEDERAL INSTITUTE OF TECHNOLOGY ZURICH
for the degree of
Doctor of Technical Sciences

presented by

TOBIAS F. LEUTENEGGER

Dipl. Masch.-Ing. ETH
born May 7, 1971
citizen of Chur, GR

accepted on the recommendation of
Prof. Dr. J. Dual, examiner
Prof. Dr. W. Sachse, co-examiner

Zürich, 2002

ACKNOWLEDGEMENTS

TABLE OF CONTENTS

ABSTRACT

In this thesis, a new method for non-destructive testing (NDT) of cylindrical structures is developed. The aim is the detection of defects as well as the determination of their positions. In order to avoid the time-consuming scanning of the whole structure, as it is done in classical ultrasonic testing methods, guided elastic waves are used instead. Structural waves are excited and propagated along the sample. These waves interact with a possible defect which results in a scattered wave field. This field is measured at different locations distributed equally around a circumference at a fixed axial coordinate. Instead of analyzing these complex time signals to determine the presence and position of a defect as is done in many other NDT methods, the recorded signals are evaluated with a time reverse numerical simulation (TRNS). This new combination of experiment, time reversal method and numerical simulation provides a fast and valuable tool for the NDT of large structures.

The main idea of the method is the time reversal of the wave propagation phenomena. This is applicable because the equations describing the wave propagation are time-reversal-invariant. If the time histories of a wave experiment with a point source are reversed in time and played back in the identical structure, the waves travel back the same path and interfere constructively which leads to an amplitude increase at their origin. This means that if one plays back the scattered field, generated by a defect, the retransmitted waves interfere exactly at the position of the defect.

Therefore, an experiment is performed in a defective tube and the displacements of the scattered field are measured at several points along the circumference at one end. Since the TRNS method only works if all three displacement components are played back, a three-dimensional vibrometer is built. The laser beam of a commercial interferometer is divided into three beams using two beamsplitters. Then, the three beams are guided from different directions onto one spot on the surface of the structure.

Instead of playing back the time histories in the experiment as is done in common time reversal applications, this step is replaced by a simulation. The main advantage of this new approach is the determination of the position of the interference and the maximum amplitude. While in an experiment, one would have to scan the structure to find the maximum, in a numerical simulation the displacement and stress components can easily

be monitored. Another benefit is that the accurate excitation of all three displacements in the corresponding points is very difficult in an experiment but easy in the numerical simulation.

To perform the simulations, the structure is implemented in a numerical code. Even if no defect is present in the simulated sample, the played back displacement histories interfere, and the maximum amplitude is reached at the exact position where the defect was located during the experiment. This works as long as the simulated structure and the sample used in the experiment are identical in terms of material and geometrical parameters and boundary conditions.

Due to the non-axisymmetric scattered fields and the implementation of part-through notches, a three-dimensional code in cylindrical coordinates is used in the present work. The applied algorithm is a displacement-stress finite-difference code. In order to determine the exact axial and circumferential position of the defects, the numerical simulation must be of high accuracy. Special care must be taken to eliminate errors due to numerical dispersion. Even though the implementation of a second-order accurate code is much easier, especially for the boundary conditions, a fourth-order algorithm is used. This is due to the fact that the fine grid, which is required for an accurate second-order code exceeds the computational hardware. Therefore, a three-dimensional code in cylindrical coordinates which is fourth-order accurate in axial and circumferential direction, and second-order accurate in radial direction and time has been implemented for the first time.

To verify the applicability of the TRNS method to the NDT of tubes, the entire procedure is simulated. This eliminates the errors caused by the experimental measurements and the uncertainties of the material and geometrical parameters of the test samples. The obtained result verifies the concept of the TRNS method.

Then, different experiments are performed with axial and circumferential notches as well as a notch that is orientated at a 45 degree angle with respect to the axis of the tube. The defects are at a distance of 0.8 m from the measurement position and are only part-through the thickness of the tubes. The waves are excited with an axisymmetric piezo-electric element glued to one end of the tube. However, since the time signals are not analyzed directly, there is no need to excite specific wave modes. Basically, any excitation that generates a scattered field at the defect can be applied.

The experimental results show that the defects are detected in all cases and that the axial, as well as the circumferential positions and the orientation of the defect could be determined with great accuracy. Even for very small defects with only 0.3% of the cross-sectional area removed, the TRNS method still provides good results.

The new NDT method of the present thesis is developed and tested for the case of cylindrical structures and homogeneous isotropic material. However, the idea can be applied to structures with other geometries and material behavior as well.

ZUSAMMENFASSUNG

In dieser Arbeit wird eine neue Methode zur zerstörungsfreien Detektion von Defekten in zylindrischen Strukturen entwickelt und vorgestellt. Im Gegensatz zur klassischen Ultraschallprüfung werden hier geführte, elastische Wellen verwendet. Dadurch kann das zeitaufwendige Abtasten der gesamten Struktur vermieden werden. Die Strukturwellen werden an einem Ende angeregt und breiten sich entlang des Probestückes aus. Im Falle eines Fehlers interagieren die Wellen mit dem Defekt, und es entsteht ein gestreutes Wellenfeld. Diese Verschiebungen werden an verschiedenen Punkten, entlang einem Umfang an einer fixen axialen Stelle, in Funktion der Zeit gemessen. Auf Grund der vielen Wellenmoden sind diese Zeitsignale sehr kompliziert und schwierig zu interpretieren. Deshalb werden sie, im Gegensatz zu vielen anderen Methoden, nicht direkt analysiert, sondern mit Hilfe einer numerischen Simulation der Zeitumkehr-Methode (*time reverse numerical simulation, TRNS*) ausgewertet um den Fehler zu detektieren und seine Position zu bestimmen. Diese neuartige Kombination von Experimenten, der Zeitumkehr-Methode und Simulationen liefert ein schnelles und wertvolles Werkzeug für die zerstörungsfreie Prüfung grosser Strukturen.

Die Methode basiert auf der zeitlichen Umkehr von Wellenausbreitungsphänomenen. Wenn man die aufgenommenen Zeitsignale aus einem Wellenexperiment mit Punktanregung zeitlich umkehrt und in derselben Struktur zurückspielt, laufen die Wellen den gleichen Weg zurück und interferieren konstruktiv an ihrem Ursprung, was zu einer detektierbaren Amplitudenüberhöhung führt. In Bezug auf gestreute Wellenfelder von Defekten bedeutet dies, dass die zurückgespielten Wellen an der Stelle des Fehlers fokussiert werden.

Zuerst werden in einem Experiment mit Hilfe eines piezoelektrischen Elementes Strukturwellen in einem fehlerhaften Rohr angeregt. Die Verschiebungen des gestreuten Wellenfeldes werden in mehreren Punkten entlang einem Umfang aufgenommen. Eine Voraussetzung für ein korrektes Interferieren in der Zeitumkehr-Simulation ist, dass alle drei Verschiebungskomponenten zurückgespielt werden müssen. Deshalb wurde ein Vibrometer gebaut, das drei Verschiebungsrichtungen messen kann. Der Laserstrahl eines herkömmlichen Laserinterferometers wird durch zwei Strahlteiler in drei Strahlen aufgeteilt, welche dann mittels Spiegeln von drei verschiedenen Richtungen auf einen

Punkt der Struktur fokussiert werden.

Anstatt die zeitlich umgekehrten Wellen wieder in dem Experiment zurückzuspielen, wie dies üblicherweise bei Zeitumkehr-Experimenten der Fall ist, wird dieser Schritt durch eine Simulation ersetzt. Dieser neue Ansatz hat die beiden folgenden Vorteile. Die Anregung aller drei Verschiebungsrichtungen in den entsprechenden Punkten des Prüfkörpers ist im Experiment sehr schwierig, in der Simulation jedoch einfach zu realisieren. Ausserdem müsste man im Experiment die gesamte Oberfläche der Struktur während dem Zurückspielen abgetasten, um den Ort der Amplitudenüberhöhung zu finden. Dieses Abtasten kann eliminiert werden, da die Verschiebungs- und Spannungskomponenten in der Simulation einfach visualisiert und beobachtet werden können.

Dazu wird das Testobjekt mittels einem numerischen Modell beschrieben. Solange sowohl Geometrie, als auch Materialdaten und Randbedingungen der simulierten Struktur genau mit denjenigen des Testobjektes übereinstimmen, interferieren die zurückgespielten Wellen genau an der Stelle, wo der Fehler im Experiment war, auch wenn gar kein Fehler in der Simulation implementiert wird. Aufgrund des nicht axialsymmetrischen, gestreuten Feldes ist ein dreidimensionaler Algorithmus in Zylinderkoordinaten notwendig. Hier wurde ein Verschiebungs-Spannungs-Finite-Differenzen Code verwendet. Um die genaue Position der Fehler zu bestimmen, muss der Algorithmus eine hohe Genauigkeit aufweisen. Insbesondere müssen die Fehler aufgrund der numerischen Dispersion klein gehalten werden. Da das feine Gitter, welches für eine genügende Genauigkeit des 2. Ordnung-Codes notwendig wäre, an die Grenzen der Computerleistungen stösst, wird eine Approximation höherer Ordnung verwendet. Dazu wurde zum ersten Mal ein dreidimensionaler Algorithmus in Zylinderkoordinaten mit einer Genauigkeit von 4. Ordnung in axialer und tangentialer Richtung und 2. Ordnung in radialer Richtung und der Zeit implementiert.

Zur Überprüfung der Anwendbarkeit der TRNS-Methode zur zerstörungsfreien Prüfung von Rohren, wird der gesamte Ablauf, d.h. auch der experimentelle Teil, simuliert. Die genauen Resultate verifizieren das Prinzip der entwickelten TRNS-Methode.

Experimente an Aluminiumrohren mit verschiedenen Nuten, welche in Bezug auf die Wandstärke nicht durchgehend sind, wurden durchgeführt. Die Defekte befinden sich jeweils etwa 0.8 Meter von der Mess- und Anregungsstelle entfernt. Obwohl in den Experimenten ein axialsymmetrisches Piezoelement verwendet wurde, kann im Prinzip eine beliebige Anregung verwendet werden. Dies ist möglich, da die Zeitsignale nie direkt analysiert werden müssen und darum keine definierten Wellenmoden notwendig sind. Die experimentellen Resultate zeigen, dass nicht nur alle Nuten erkannt wurden, sondern dass sowohl deren axiale, als auch tangentiale Position und die Orientierung der Fehler genau bestimmt werden können. Sogar bei sehr kleinen Nuten, wo nur gerade 0.3% der Querschnittsfläche entfernt wurde, kann die Position bestimmt werden.

Diese neue Methode zur zerstörungsfreien Prüfung, welche in der vorliegenden Arbeit anhand von homogenen, isotropen Rohren hergeleitet und getestet wurde, kann natürlich auch auf Strukturen andere Geometrien und Materialien angewendet werden.

LIST OF SYMBOLS

A	coefficient matrix for stability analysis
C_{lmpq}	stiffness element
E	Young's modulus, elastic modulus
E, F	measurement planes
E1, E2, E3	intersection points with plane E
F1, F2, F3	intersection points with plane F
$F(n, m)$	flexural wave modes
G	amplification matrix
G	shear modulus
I	imaginary unit $\sqrt{-1}$
I	3x3-identity matrix
$L(0, m)$	longitudinal wave modes
N	number of points of digitized signals
R	radius of midplane
T	recording duration
$T(0, m)$	torsional wave modes
U_r	radial displacement amplitude
U_φ	circumferential displacement amplitude
U_z	axial displacement amplitude
a, b, c	adjustable distances for three-dimensional vibrometer
a_r, a_φ, a_z	coefficient vectors for explicit displacement equations
b_{rr}	coefficient vector for explicit stress equation
c_g	group velocity
c_{max}	maximum wave velocity
c_p	primary wave velocity
f_s	sampling frequency
g	constant for general von Neumann condition
h	wall thickness
i	circumferential index

j	axial index
k	radial index
k	wave number
$\boldsymbol{k}$	wave vector
k_r, k_φ, k_z	components of the wave vector $\boldsymbol{k}$
l	length of tube
l	index for r, φ, and z
m	index for r, φ, and z
m	index for eigenvalues 1,...,6
m	wave mode number
n	circumferential order of non-axisymmetric wave modes
n	time index
p	index for r, φ, and z
q	index for r, φ, and z
r	radial coordinate
r_k	discrete radius of k-th layer
r_{max}, r_{min}	maximum, minimum discrete radius
s	stability factor
t	time
t_{exc}	excitation duration
t_{sim}	simulation duration
$\boldsymbol{u}_{new}$	displacement component matrix at time step n+1
$\boldsymbol{u}_{now}$	displacement component matrix at time step n
$\boldsymbol{u}_{old}$	displacement component matrix at time step n-1
u_1, u_2, u_3	measured displacement components of beam one, two, and three
u_r, u_φ, u_z	radial, circumferential, and axial displacement
$\tilde{u}_r$, $\tilde{u}_\varphi$, $\tilde{u}_z$	radial, circumferential, and axial displacement at measurement point
$\boldsymbol{u}_s$	vector with surrounding displacement components
$\boldsymbol{u}_s$	scattered wave field
$\boldsymbol{u}_{TR}$	time reversed wave field
$\hat{u}_\xi$	amplitudes of harmonic wave ansatz
$\boldsymbol{w}$	amplitude vector for stability analysis
w	transversal displacement
z	axial coordinate
Λ_m	eigenvalue of amplification matrix
α, β, γ	angles of three-dimensional vibrometer
$\Delta 1$, $\Delta 2$, $\Delta 3$	distances between intersection points
Δr_{EF}	distance between planes E and F
Δr, $\Delta\varphi$, Δz	radial, circumferential, and axial grid steps
Δt	time step
Δt_g	time difference to determine group velocity
Δx_1, Δx_2, Δx_3	space increments

Δz_g	distance to determine group velocity
δ_{lm}	Kronecker symbol
ε_{pq}	mechanical strain component
ζ	index for time shifts
ζ_{max}	number of time shifts for maximum convolution
λ_{min}	minimum wavelength
λ	Lamé constant
μ	Lamé constant
ν	Poisson's ratio
ξ	index for r, φ, and z
ρ	mass density
σ_{lm}	mechanical stress component
$\boldsymbol{\sigma}_{now}$	stress component matrix at time n
$\boldsymbol{\sigma}_s$	vector with surrounding stress components
φ	circumferential coordinate
ψ_x, ψ_y	rotation angles
ω	angular frequency
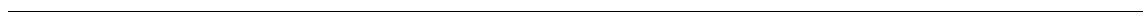
LIST OF ABBREVIATIONS

ABC	absorbing boundary condition
EMAT	electromagnetic acoustical transducer
GPIB	general purpose interface bus
FDM	finite-difference method
FDTD	finite-difference time domain
FEM	finite element method
FIT	finite integration technique
NDT	non-destructive testing
PML	perfectly matched layer
QNDE	quantitative non-destructive evaluation
TRM	time reverse mirror
TRNS	time reverse numerical simulation
UT	ultrasonic testing
VS-FD	velocity-stress finite-difference

1. INTRODUCTION

1.1 Motivation

The extensive use of pipes in many applications and installations demands non-destructive testing (NDT) methods to ensure the safety of the environment. The integrity of pipeline systems is not only vital to the industry but also crucial in terms of water, oil, gas, chemical, or nuclear leakage. The increasing application of tubes asks for fast and simple NDT methods. Therefore, quality control requires that structures are tested on-line during the manufacturing process, which is described in detail in [58]. To monitor the conditions during the service, field inspections are performed periodically. In the last decades, a variety of NDT procedures, such as eddy-current testing, radiography, ultrasonic testing, thermography, magnetic particle examination, and many others, have been developed and used. The various operating methods are explained in [58], while Bar-Cohen provides a good overview of the techniques currently applied in [3]. The method most frequently used on pipelines is the ultrasonic testing (UT). In traditional UT, mechanical waves in the MHz range are used to test the structures. Since these high-frequency waves are damped out quickly, the method can only be applied to inspect the area below or adjacent to the transducer. Therefore, the probe must be moved over the whole surface of the object to be tested, which is very time-consuming and requires overall access.

An alternative method for single location measurements is the use of guided elastic waves which propagate along the structure. The wavelengths of these structural waves are several times the thickness of the structure (e.g. a beam, plate, or shell) and are at least an order of magnitude larger than the ones used in traditional UT. In spite of the large wavelength, small defects can still be detected as shown by Dual et al. [12] who use guided waves for the detection of defects in rods. The

advantage of guided waves is that they travel many wavelengths along a structure, depending on material and geometry. This enables fast long-range testing and eliminates the need to scan the whole sample. Since structural waves propagate along the structure, even normally inaccessible regions can be tested and the removal of any insulation can be avoided.

Motivated by the existing know-how of elastic wave propagation in cylindrical structures at the Center of Mechanics at the ETH Zurich, which was achieved by the dissertations of Dual [10], Vollmann [56], and Gsell [22], the goal of the present work is the development of a NDT method for the detection of defects in cylindrical structures using guided waves. Displacement measurements taken from only a few positions are analyzed to inspect a large part of the structure and to determine the axial as well as the circumferential position of the notches and their orientation.

1.2 Guided waves in cylindrical tubes

Guided waves appear if an elastic wave propagates between two boundaries, e.g. in plates or shells. The superpositions of compression and shear waves caused by multiple reflections from the boundaries lead to interference patterns which form guided wave packets. These different modes propagate along the structure at different velocities.

The first paper on an exact theoretical investigation of guided wave propagation in hollow circular cylindrical structures in the isotropic case was written by Gazis in 1959 [18]. The displacement components of non-axisymmetric harmonic waves, travelling in the axial direction, can be written in cylindrical coordinates (r, φ, z) in the form

$$
\begin{aligned}
u_r &= U_r(r) \cdot cos(n\varphi) \cdot cos(\omega t + kz) \\
u_\varphi &= U_\varphi(r) \cdot sin(n\varphi) \cdot cos(\omega t + kz) \\
u_z &= U_z(r) \cdot cos(n\varphi) \cdot sin(\omega t + kz)
\end{aligned}
\tag{1.1}
$$

where u_r, u_φ, and u_z denote the displacement components in radial, circumferential, and axial direction, respectively. U_r, U_φ, and U_z are the corresponding displacement amplitudes which can be composed of Bessel functions. $n = 0,1,2,...$ is the circumferential order, k the axial wave number, and ω the angular frequency.

Three different classes of modes can be recognized in infinitely long pipes, all propagating along the axis of the tube. Gazis showed that there are a doubly infinite number of modes for a circular cylinder, which includes an infinite number of torsional modes, an infinite number of longitudinal modes, and a doubly infinite number of flexural modes. Following the notation of Meitzler [35], Silk and Bainton [47], and Rose [40], they are designated as follows

- longitudinal modes: $L(0, m)$ (axisymmetric modes)

- torsional modes: $T(0, m)$ (axisymmetric modes)

- flexural modes: $F(n, m)$ (non-axisymmetric modes)

with mode number $m = 1,2,3,...$ and circumferential order $n = 1,2,3,...$ for the flexural modes. The longitudinal and torsional modes for which $n = 0$ are axisymmetric. For the other circumferential orders the displacements are no longer axisymmetric and the occurring modes are the non-axisymmetric flexural modes.

Dispersion diagrams are an effective means to visualize the dispersive behavior of the structure and to anticipate what modes to expect at a particular frequency. Dispersion means, that the velocity of a wave is a function of its frequency or wavelength. The modes depend on material properties and characteristic geometrical parameters of the waveguide, such as radius and wall thickness in the case of pipes.

In Fig. 1.1 one method for representing the dispersion relation of an isotropic aluminum tube with a radius of midplane $R = 0.016 \, \text{m}$ and a wall thickness $h = 2 \, \text{mm}$ is depicted. The exact material parameters are given in Table A.1 in Appendix A.1. The wave numbers of the different modes are plotted versus the frequency up to $1 \, \text{MHz}$. The first three longitudinal and two torsional modes (circumferential order $n = 0$), which are axisymmetric modes, are plotted as dashed black curves. The solid gray lines correspond to the first five non-axisymmetric flexural modes with $n = 1$. The flexural modes with circumferential order higher than one are not plotted.
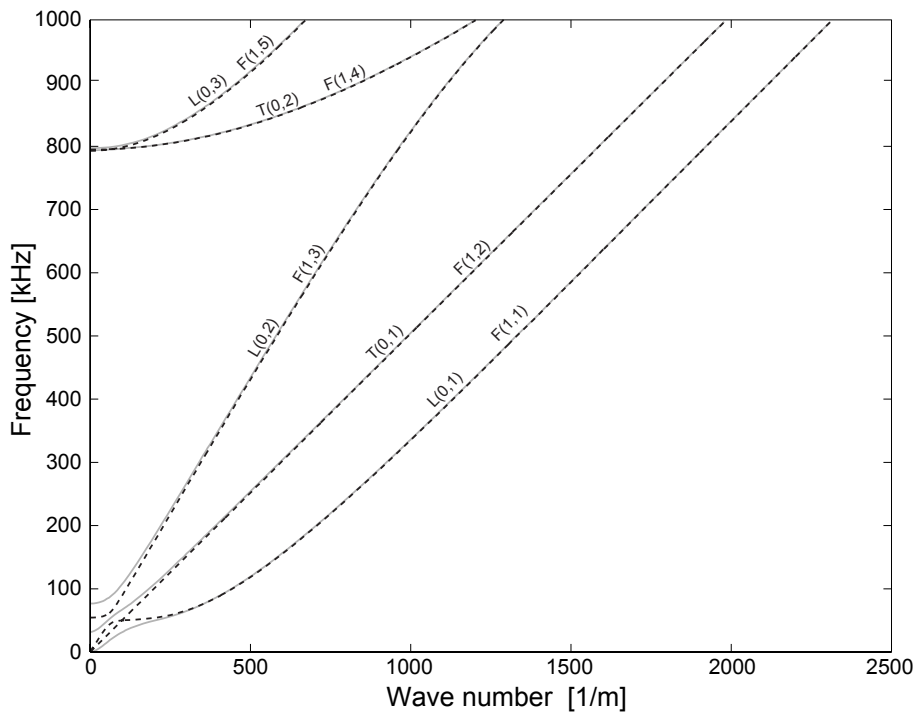
Figure 1.1: Frequency spectrum for an aluminum tube (data see Table A.1 in Appendix A.1). The axisymmetric longitudinal and torsional wave modes for $n = 0$ (dashed black curves) and the flexural modes for $n = 1$ (solid gray lines) are plotted.

Another method to display the various wave modes is shown in Fig. 1.2, where the phase velocities of the modes are given as a function of frequency.
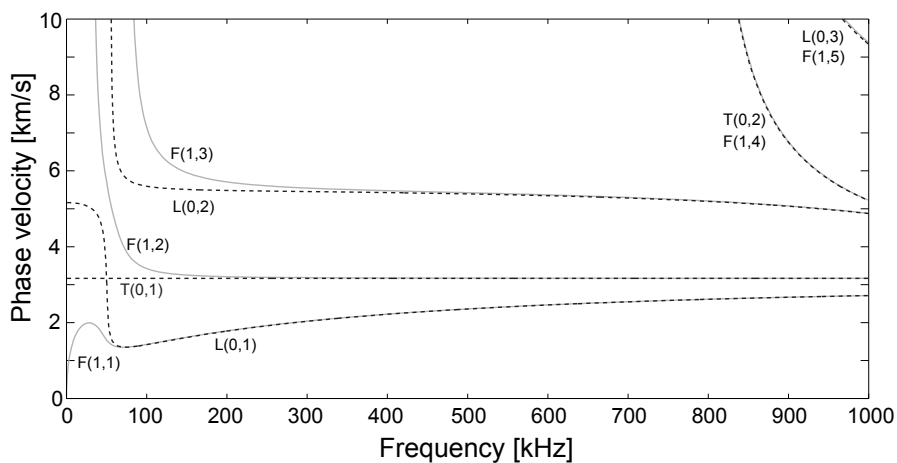
Figure 1.2: Phase velocity dispersion curves for an aluminum tube (data see Table A.1 in Appendix A.1). The axisymmetric modes (longitudinal and torsional) are plotted as dashed black lines while the gray curves correspond to the flexural modes with $n = 1$.

In the third frequently used dispersion diagram the group velocity curves are plotted versus frequency (Fig. 1.3) or wave number. The group velocity is defined as

$$c_g = \frac{d\omega}{dk} \tag{1.2}$$

The group velocity corresponds to the propagation velocity of a group of waves of similar frequency. It can also be understood as the velocity at which the energy of a wave packet travels.
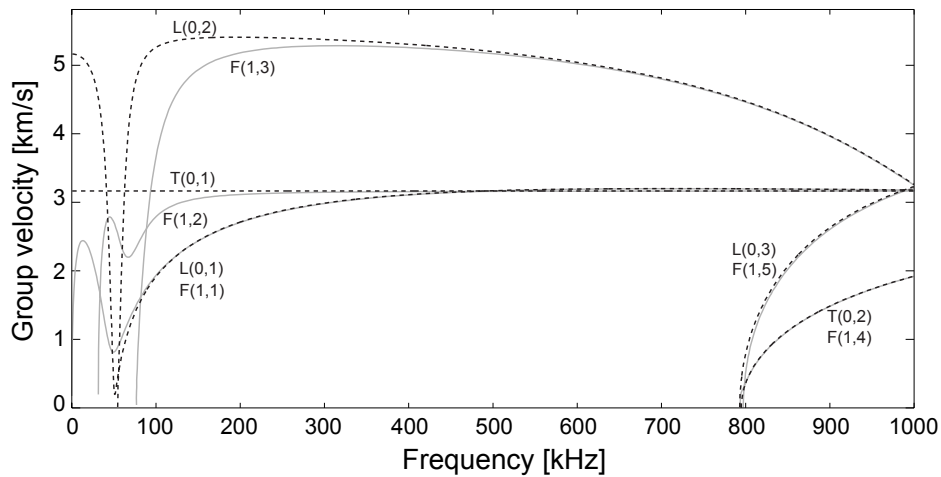
Figure 1.3: Group velocity dispersion curves for an aluminum tube (data see Table A.1 in Appendix A.1) for longitudinal L(0,m) and torsional T(0,m) modes (shown as dashed black lines), and flexural F(1,m) modes (solid gray curves).

The dispersion diagrams are generated using a numerical analytical method (NAM) described by Nelson et al. [38], which is based on the variational principle of the mechanical energy. Therefore, the functions for the displacements from Eq. (1.1) are used to calculate the kinetic and strain energies. The three functions $U_r(r)$, $U_\varphi(r)$, and $U_z(r)$ are approximated by linear finite elements. The variation of the total energy leads to a generalized eigenvalue problem for each wave number k. The natural frequencies at the particular wave number can be calculated from the resulting eigenvalues and the eigenvectors correspond to the displacements of the nodes. For a detailed description of this effective and fast method for the determination of dispersion diagrams, the reader is referred to the dissertation by Gsell [22].

While in the case of longitudinal modes $L(0, m)$ the radial and axial particle motions are coupled and no tangential displacements exist, the only occurring displacements for torsional modes $T(0, m)$ are circumferential. The reason is that the equation of motion in circumferential direction is uncoupled from the equations of motion in radial and axial directions. With non-axisymmetric modes $F(n, m)$ all three particle motions are coupled to one another.

To illustrate the coupling of radial and axial displacements of the longitudinal modes, the normalized displacements are plotted versus the tube thickness for the modes L(0,1) and L(0,2) in Fig. 1.4.
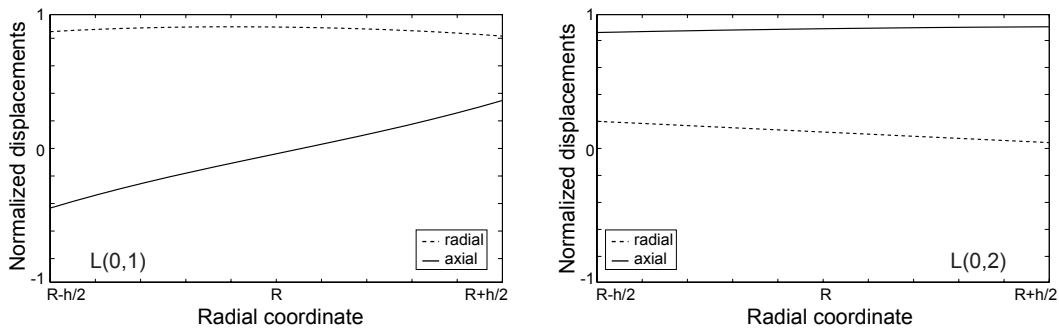
Figure 1.4: Radial (dashed line) and axial (solid line) displacements of the longitudinal modes L(0,1) [left, k ≈ 586 m^{-1}] and L(0,2) [right, k ≈ 172 m^{-1}] at 150 kHz for an aluminum tube (data see Table A.1 in Appendix A.1). The displacements are normalized and plotted versus the radial coordinate. Due to the curvature, the displacements are not symmetric with respect to the midplane.

Compared to guided waves in plates, the displacements are no longer symmetric with respect to the midplane of the wall (with Radius R). The reason is the curvature of the tube. Especially at higher frequencies the cross-sections do not remain plane and the displacements are neither constant over the thickness of the tube nor a linear function of r (Fig. 1.5), which justifies the use of the three-dimensional theory instead of the shell theory.
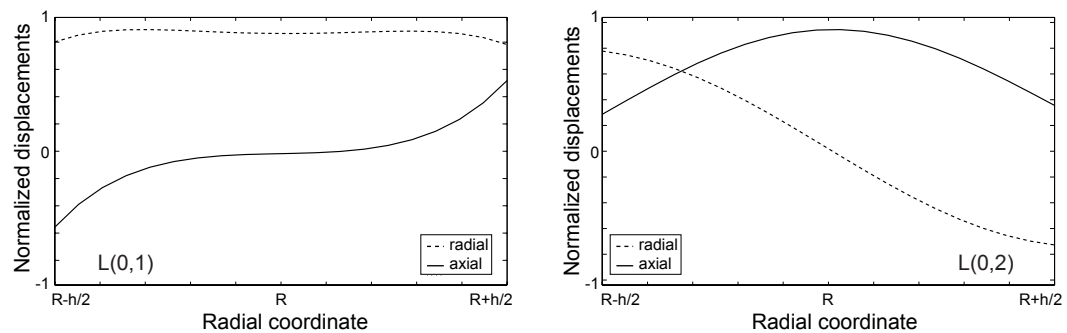
Figure 1.5: Radial (dashed line) and axial (solid line) displacements of the longitudinal modes L(0,1) [left, $k \approx 2320$ m^{-1}] and L(0,2) [right, $k \approx 1290$ m^{-1}] at 1 MHz for an aluminum tube (data see Table A.1 in Appendix A.1). The displacements are normalized and plotted versus the radial coordinate. Due to the curvature, the displacements are not symmetric with respect to the midplane.

1.3 Common NDT approaches using guided waves

The idea of using guided waves for improved inspection efficiency has been around for many years. The nature of the guided waves is such that they propagate along the tube for many wavelengths before being attenuated. Any potential defects within this range reflect some of the incident waves and the displacements of these scattered waves are recorded and interpreted to detect the flaws. Rose et al. [42] list the main advantages of this technique compared to the normal beam ultrasonic or eddy current methods as follows:

- The ability to simultaneously inspect a large length of tubing thus greatly increasing the cost-effectiveness of inspections.

- The ability to simultaneously inspect the entire cross-section of the tubes, resulting in 100% coverage.

- No need for complicated and expensive insertion or rotation devices since the probe does not have to be moved during the inspection.

- An increased sensitivity to many of the defects occurring in the tubes.

Already in 1976, Mohr and Höller [37] used electrodynamic transducers for the non-contacting excitation of the L(0,2) and T(0,1) modes in tubes for the detection

of echos in the time signals from tangential, and longitudinal notches, respectively. A survey of the history of guided wave inspection as well as early and recent guided wave pioneering work in the area of guided waves is provided by Rose [41].

The principle of the most commonly used guided wave techniques is the interpretation of reflections from faults in the time signals. However, this is a difficult task since after the interaction with a defect several wave modes are present in hollow cylinders, even with an axisymmetric excitation. Another problem is that the modes are generally dispersive, which means that the shape of a propagating wave changes with distance along the propagating path.

The concept of Alleyne et al. [1] consists in choosing one specific mode in a non dispersive frequency range which they try to excite in isolation. They use a large number of transducers (e.g. 16 for a 76 mm diameter pipe) which are distributed evenly around the circumference and driven in a parallel manner. Using multiple transducer rings of that type, mounted at intervals of the wavelength, they are able to excite mainly one axisymmetric longitudinal mode. Using the same transducers, the reflections from defects, welds and flanges are recorded. Their goal was the detection of regions of corrosion larger than $3h \times 3h$ in dimension and $h / 2$ depth (where h denotes the thickness of the wall), which they achieved in field experiments in ranges of up to 15 m with an axial accuracy of approximately 100 mm ([2]). To distinguish between axisymmetric reflections from welds and non-axisymmetric echos from defects, Lowe et al. [32] introduce an angularly dependent phase lag to each transducer element of the receiver before summing their signals.

Shin and Rose [44] use transducers placed on variable angle beam shoes for the excitation and detection of non-axisymmetric waves. The motivation is that the generation of axisymmetric waves is often hard to achieve due to limited access. For 100% inspection coverage, however, three-dimensional tuning (distance, frequency, and angle tuning) must be employed to avoid *blind spots*.

The above mentioned methods are successfully applied to locate the axial positions of defects in long range NDT. Therefore, the recorded time signals are analyzed to determine the time differences between the incident wave and the reflections. This result is distorted due to the dispersive behavior of the wave packets. The second challenge consists in the selection of the appropriate group velocity from the dispersion diagram. Even with a single-mode pulse, the waves reflected from the defects are multi-mode due to mode conversion. Hence, the determination of the corresponding modes and their velocities is no longer straightforward.

Another method for the NDT is the application of the time reverse method described by Fink [14]. The principle of this method is explained in detail in Chapter 3.1. Ing et al. [26] use the time reverse method to detect flaws in plates. The scattered field from a defect is recorded using an array of transducers. Then these signals are reversed in time and retransmitted in another experiment into the same structure. This procedure is repeated several times until the location of the defect can be determined by analyzing the time signals from the different transducers. In another experiment, they use a laser interferometer to detect the origin of a wave. Therefore, the time reversed signals measured again with the transducer array are retransmitted and the position with the maximum amplitude in the time reversed experiment is found by searching the maximum displacement with a laser.

1.4 Objective and outline of the present work

The goal of the present work consists in the development of a long-range NDT approach for cylindrical structures, which is based on guided elastic waves and not only allows the detection of the axial and circumferential position but also the orientation of defects. Instead of directly analyzing the time signals, another concept is used to detect the positions of notches. The recorded signals which are reflected from the defect are reversed in time and used as excitation signals for a simulation of waves in pipes.

For the simulations, a three-dimensional code to describe the phenomena of wave propagation in hollow cylinders is necessary. The technique applied in the present thesis is based on the finite-difference method (FDM) and is described in detail in Chapter 2. A three-dimensional code in cylindrical coordinates which is fourth-order accurate in axial and tangential, and second-order accurate in radial direction and time is implemented for the first time.

Compared to commonly used time reverse methods, the recorded signals are not played back in another experiment on the defective structure, but are used as input data for a numerical simulation. This is a new approach and eliminates the time-consuming scanning of the structure and the interpretation of the time signals. The principle of the time reverse method and its verification is discussed in Chapter 3. One of the benefits is that even small reflections that are barely visible in the time signals can be used to find defects. Since there is no need to assign the reflections in the time signals to a specific mode, any method for generating scat-

tered fields from the defects can be used. A complicated setup for generating only one specific wave mode is not necessary. The experimental results for different notches, the evaluation procedure, and the testing setup are presented in Chapter 4.

The combination of experimental measurements, the time reversal method, and numerical simulations, which is done for the first time to the authors knowledge, provides a new tool for the fast NDT of large structures. In the present thesis, the method is developed and tested for the case of cylindrical structures and homogeneous isotropic material. However, the idea can also be applied to structures with other geometries and material behavior.

2. NUMERICAL SIMULATION OF WAVE PROPAGATION

2.1 Introduction

Numerical simulations are very useful methods to describe wave propagation phenomena in more complex structures. While analytically, it is very difficult to find an exact solution for the interaction of waves with a defect in a tube, the scattered wave fields that occur can be calculated more easily numerically. The numerical treatment of complicated three-dimensional problems is becoming increasingly popular due to the fast development of computational hardware and the decline of computing costs. In order to solve a problem numerically, the area is divided into many small cells, and the appropriate equations and boundary conditions are fulfilled for each cell.

Today, the following three numerical methods are used predominantly for the simulation of wave propagation in linear elastic media.

In the finite integration technique (FIT) (see Marklein [34] and Schubert et al. [43]), the basic laws of physics of the problem are spatially discretized by an integration of the differential equations over a certain control volume or integration cell. The temporal discretization is done by using second-order central differences in time, which leads to an explicit scheme.

The second procedure is the finite-difference time domain method (FDTD), which was introduced in 1966 by Yee [59] to discretize the differential form of Maxwell's equations. The algorithm was applied for the first time to the elastic equations for homogeneous isotropic material in two dimensions by Madariaga in 1976 [33]. In the FDTD method the coupled partial differential equations which describe the physics of the problem are directly discretized in time and space by using central differences, which also results in an explicit solution.

The finite element method (FEM) which is described by Bathe [4], among others, is the third algorithm used for numerical simulations. Instead of discretizing the basic laws of physics directly, they are solved by using the variational principle to minimize the corresponding energy function. The discretization of time can either be done explicitly by central differences or implicitly by using the integration method of Newmark (see Ref. [57]).

All three methods are applied successfully in different areas, such as continuum mechanics, fluid dynamics, acoustics, and electrodynamics. Although the procedures can be implemented quite easily and in a straightforward manner, certain restrictions must be met. Errors resulting from numerical dispersion can be kept small by using a sufficiently high spatial sampling rate (see Chapter 2.4). The second crucial parameter is the time step used for the temporal discretization. In order to obtain a stable scheme, the stability criterion must be satisfied (see Chapter 2.3). The advantages and disadvantages of the FDTD and FEM procedures, especially the higher computational costs of the finite elements, are discussed by Gsell [22].

In this thesis, the FDTD method for cylindrical coordinates will be used (Chapter 2.2.1). In the last few years, the algorithm of Yee, which has second-order accuracy in space and time, was applied to many different problems. A selective survey of the finite-difference time domain literature is given by Shlager and Schneider [46]. In his original scheme, Yee distributed the electric and electromagnetic field components on a staggered grid in space and time domain. Madariaga's method, which also uses the allocation of velocity and stress components on a staggered grid, is known as the velocity-stress finite-difference method (VS-FD). The main purpose for using a staggered grid is to calculate spatial derivatives halfway between two grid points. Hence, if a component is needed between two defined grid points, its value has to be averaged. In 1984 and 1986 Virieux ([54], [55]) applied the VS-FD method to geophysical problems such as the SH- and P-SV-wave propagation in heterogeneous media in two dimensions. With increasing computer power, the simulation of three-dimensional problems gathered interest in the FDTD-related research activities. Temple [52] described the propagation and scattering of elastic waves in inhomogeneous anisotropic media in three-dimensional Cartesian coordinates in 1988. A three-dimensional code in cylindrical coordinates was published in 1998 by Chen and Chew [6].

In order to model open region problems or larger structures, it is necessary to truncate the computational domain. Therefore, absorbing boundary conditions (ABC) are implemented, which is one of the most active research area in the FDTD field. The ABC's can be grouped into two types: those that employ material absorbers and those that are derived from differential equations. The first differen-

tial techniques e.g. by Lindman [31] were improved by Higdon [25] and Liao et al. [30]. The most popular and advanced material-based ABC is called the perfectly matched layer (PML) absorbing boundary condition by Berenger [5].

2.2 Second-order finite-difference method

The first code used in this work for the simulation and visualization of the elastic wave propagation in tubes is a second-order accurate algorithm in space and time domain. It is based on a displacement-stress finite-difference method for homogeneous isotropic material. However, it can be extended to any linear material law governed by the general stress-strain relation

$$\sigma_{lm} = C_{lmpq} \cdot \varepsilon_{pq} \tag{2.1}$$

where σ_{lm} and ε_{pq} are the stress and strain components, respectively, and C_{lmpq} the stiffness elements. Einstein's summation convention is used for repeated indices.

In the VS-FD method introduced by Madariaga [33] and applied by many other authors ([6], [54], [55]), the velocity and stress components are not only staggered in space, but also in time. As shown by Gsell and Leutenegger [23], this time shift is not required to obtain a stable scheme (see also Chapter 2.3). If displacements are used instead of velocities and all components are on the same time grid, the integration of the velocities can be eliminated. This leads to the present displacement-stress finite-difference code.

The explicit calculation of the stress components can be eliminated by inserting the stress-strain relation (2.1) and the kinematic relations (2.7) into the equations of motion (2.2) before the discretization. This results in a displacement finite-difference code which is described by Gsell and the author in Ref. [23]. The elimination of the six stress components reduces the amount of variables and the required memory to approximately one third. Because no stress components need to be calculated, computational time is reduced by about 25%. In spite of these two advantages, the stresses are not eliminated in the present work and a displacement-stress code is used because the changes in the stress components are important values for the detection of defects. Also, by doing this, the implementation of boundary conditions (Chapter 2.2.3) and notches (Chapter 2.2.4) is rendered much simpler.

2.2.1 Three-dimensional code in cylindrical coordinates

The target applications of the simulation code consist in the study of the interaction between waves and notches and the playing back of reflections from defects (see Chapter 3.). For both tasks, a three-dimensional algorithm is required. The reason for this is that even with an axisymmetric excitation, the scattered wave fields are no longer axisymmetric. Since the rotation angles of the shell theory are difficult to measure experimentally, the three-dimensional theory is chosen instead. This also enables the implementation of notches with various depth, as described in Chapter 2.2.4.

If there are no external body forces, the three equations of motion in cylindrical coordinates (r, φ, z) are provided by Graff [20] as

$$\rho \cdot \frac{\partial^2 u_r}{\partial t^2} = \frac{\partial \sigma_{rr}}{\partial r} + \frac{1}{r}\frac{\partial \sigma_{r\varphi}}{\partial \varphi} + \frac{\partial \sigma_{rz}}{\partial z} + \frac{1}{r}(\sigma_{rr} - \sigma_{\varphi\varphi})$$

$$\rho \cdot \frac{\partial^2 u_\varphi}{\partial t^2} = \frac{\partial \sigma_{r\varphi}}{\partial r} + \frac{1}{r}\frac{\partial \sigma_{\varphi\varphi}}{\partial \varphi} + \frac{\partial \sigma_{\varphi z}}{\partial z} + \frac{2}{r}\sigma_{r\varphi} \qquad (2.2)$$

$$\rho \cdot \frac{\partial^2 u_z}{\partial t^2} = \frac{\partial \sigma_{rz}}{\partial r} + \frac{1}{r}\frac{\partial \sigma_{\varphi z}}{\partial \varphi} + \frac{\partial \sigma_{zz}}{\partial z} + \frac{1}{r}\sigma_{rz}$$

where u_r, u_φ, and u_z denote the radial, tangential, and axial displacements, t the time, and ρ is the mass density. In the next step, these partial differential equations (2.2) are discretized. Therefore, all of the first derivatives with respect to the spatial coordinates r, φ, and z are approximated by central differences (see e.g. Strauss [49]). For example, the second-order approximation of the first derivative of the stress component σ_{rz} with respect to the axial coordinate z at the position z_j (see Fig. 2.1) is given as

$$\frac{\partial \sigma_{rz}(z)}{\partial z}\bigg|_{z = z_j} = \frac{\sigma_{rz}\left(z_j + \frac{1}{2}\Delta z\right) - \sigma_{rz}\left(z_j - \frac{1}{2}\Delta z\right)}{\Delta z} + O[(\Delta z)^2] \qquad (2.3)$$

The order of the error depends on the number of terms considered in the Taylor expansions to derive the central differences. The derivatives could also be discretized by using forward or backward differences. However, to describe wave

propagation phenomena, central differences must be used in order to enable the waves to propagate into both directions.

The second derivatives with respect to the time t are also replaced with second-order central differences, e.g.

$$\left. \frac{\partial^2 u_r(t)}{\partial t^2} \right|_{t\,=\,t_\mathrm{n}} = \frac{u_r(t_\mathrm{n} + \Delta t) - 2 \cdot u_r(t_\mathrm{n}) + u_r(t_\mathrm{n} - \Delta t)}{\Delta t^2} + O[(\Delta t)^2] \qquad (2.4)$$

The index n denotes the time step. The three displacement and six stress components are allocated on a staggered grid as shown in Fig. 2.1. This is the only possibility for properly approximating all first derivatives of the equations of the problem with second-order central differences, which is necessary to obtain a stable scheme.
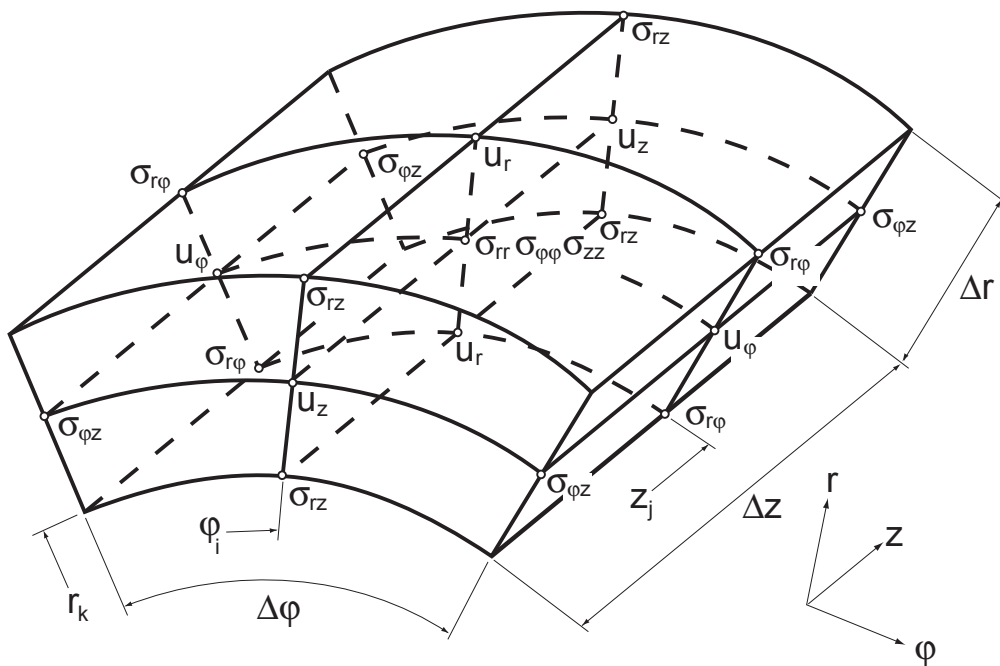
Figure 2.1: Allocation of the displacement and stress components for three-dimensional cylindrical coordinates. This distribution on a staggered grid is the only possibility to obtain a stable scheme.

Substituting the discretization rules (2.3) and (2.4) into Eqs. (2.2) and solving for the displacements at the time $t_{n+1} = t_n + \Delta t$ leads to three explicit linear equations. For example, the radial displacement u_r at the next time step n+1 is calculated as

$$
\underset{j,i,k}{u_r^{n+1}} = 2 \cdot \underset{j,i,k}{u_r^n} - \underset{j,i,k}{u_r^{n-1}} + \underset{k}{a_r^T} \cdot \underset{j,i,k}{\sigma_s^n} \tag{2.5}
$$

where the superscript T refers to the transposed vector. The superscript n denotes the index of time, with $t_n = n \cdot \Delta t$. The indices j, i, and k define the axial, circumferential, and radial positions of the corresponding components on the grid. The surrounding stress components of the grid region $j \pm 1$, $i \pm 1$, $k \pm 1$ at the time step n, which are required for the present case, are the elements of the vector σ_s. The elements of the vector a_r are functions of the discretization parameters Δr, $\Delta \varphi$, Δz, and Δt, the radius r_k, and the mass density ρ, and are used to weigh the influences of the neighboring stress values. The components of the vectors σ_s and a_r for Eq. (2.5) are given in Eqs. (A.2) and (A.3) in Appendix A.2 as an example. Since these elements depend on the radial coordinate, they must be calculated separately for each radial layer of the grid. The tangential and axial displacements at the next time step are calculated in the same manner, but with different vectors, a_φ and a_z.

The stress components at the time step n are computed using Hooke's law for isotropic linear elasticity (applying Einstein's summation convention for repeated indices)

$$
\sigma_{lm} = \lambda \cdot \varepsilon_{pp} \cdot \delta_{lm} + 2\mu \cdot \varepsilon_{lm} \tag{2.6}
$$

where ε are the strain components and δ_{lm} denotes the Kronecker symbol. The linear kinematic relations in cylindrical coordinates are given as

$$\varepsilon_{rr} = \frac{\partial u_r}{\partial r} \qquad\qquad \varepsilon_{r\varphi} = \frac{1}{2} \cdot \left(\frac{1}{r} \cdot \frac{\partial u_r}{\partial \varphi} + \frac{\partial u_\varphi}{\partial r} - \frac{u_\varphi}{r} \right)$$

$$\varepsilon_{\varphi\varphi} = \frac{1}{r} \cdot \frac{\partial u_\varphi}{\partial \varphi} + \frac{u_r}{r} \qquad\qquad \varepsilon_{rz} = \frac{1}{2} \cdot \left(\frac{\partial u_r}{\partial z} + \frac{\partial u_z}{\partial r} \right) \qquad (2.7)$$

$$\varepsilon_{zz} = \frac{\partial u_z}{\partial z} \qquad\qquad \varepsilon_{\varphi z} = \frac{1}{2} \cdot \left(\frac{\partial u_\varphi}{\partial z} + \frac{1}{r} \cdot \frac{\partial u_z}{\partial \varphi} \right)$$

The Lamé constants λ and μ will be replaced by

$$\lambda = \frac{E \cdot \nu}{(1 + \nu) \cdot (1 - 2\nu)} \qquad \mu = G = \frac{E}{2 \cdot (1 + \nu)} \qquad (2.8)$$

since the material of the experimental samples is described by Young's (or elastic) modulus E and the shear modulus G or Poisson's ratio ν.

Inserting Eqs. (2.7) into (2.6) and replacing all first derivatives of the displacements with central differences leads to six explicit equations for the stress components at the time step n. For example

$$\overset{n}{\underset{j,i,k}{\sigma_{rr}}} = \overset{T}{\underset{k}{b_{rr}}} \cdot \overset{n}{\underset{j,i,k}{u_s}} \qquad (2.9)$$

where the vector u_s contains the required surrounding displacement components at the time step n and the elements of the vector b_{rr} are functions of the geometrical, discretization, and material parameters. Due to the curvature, these elements must once again be calculated for each radial layer. The components of u_s and b_{rr} for the radial normal stress component [Eq. (2.9)] are given in Eqs. (A.5) and (A.6) in Appendix A.2. The other stress components are derived accordingly.

2.2.2 Implementation and excitation

The structure can be excited by driving either displacement or stress components with a given function. Therefore, a region of the grid is chosen as the source position, and during the excitation duration t_{exc} the corresponding stress or displacement components are replaced by the excitation value at each time step. The major steps of the implementation of the algorithm are shown in Fig. 2.2.

The displacement values at the three times $n-1$, n, and $n+1$ are labeled $\boldsymbol{u}_{old}$, $\boldsymbol{u}_{now}$, and $\boldsymbol{u}_{next}$. The stress components are only needed at the time step n and are denoted as $\boldsymbol{\sigma}_{now}$. The durations of the excitation and the simulation are given as t_{exc} and t_{sim}, respectively.
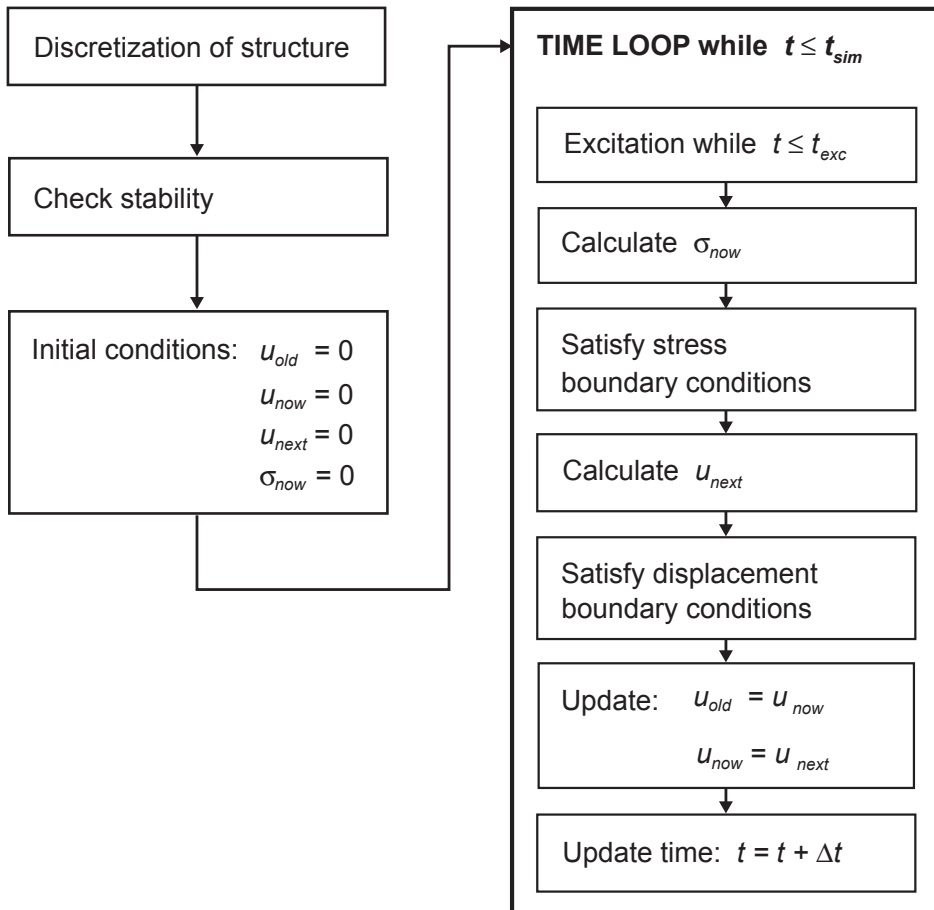
Figure 2.2: Diagram of the major steps of the implementation of the three-dimensional finite-difference algorithm in cylindrical coordinates.

2.2.3 Boundary conditions

Due to the staggered grid, one can choose where to define the structural boundaries. For example, two different radial layers can be used for the inner and outer surface of the tube, either the layer with the components u_r, $\sigma_{r\varphi}$, and σ_{rz}, or the layer with an offset of $\Delta r\,/\,2$ (see Fig. 2.1). In the case presented here, the layer with the components u_φ, u_z, σ_{rr}, $\sigma_{\varphi\varphi}$, σ_{zz}, and $\sigma_{\varphi z}$ is chosen as the structural boundary. The reason for this is that the displacements at the outer surface are measured in the experiments (Chapter 4.) and in order to increase the accuracy, as many displacement components as possible should be allocated on the outer surface of the discrete structure.

Stress-free and displacement-fixed boundary conditions can be applied. For example, the following stress components must vanish for stress-free inner and outer surfaces of the tube. In this case, the tube is assumed to be surrounded by vacuum.

$$\sigma_{rr}\left(R\pm\frac{h}{2}\right) \;=\; \sigma_{r\varphi}\left(R\pm\frac{h}{2}\right) \;=\; \sigma_{rz}\left(R\pm\frac{h}{2}\right) \;=\; 0 \qquad\qquad (2.10)$$

Here R denotes the radius of the midplane and h the wall thickness of the tube. The corresponding components which are located on the boundary of the structure, can directly be set to zero. In the present configuration this is only σ_{rr}. Since the finite-difference approach is based on the use of the values of neighboring points, the following problem arises. The remaining values on the grid points describing the structural boundaries cannot be calculated using the explicit Eqs. (2.5) and (2.9) because they are missing the appropriate neighboring points. This means that some of the elements of the vectors $\boldsymbol{u}_s$ and $\boldsymbol{\sigma}_s$ are not defined on the boundaries. To correct this, the concept of a fictitious layer next to the surfaces outside the structure is introduced as described by Harker [24]. The displacement and stress components of the fictitious grid points are calculated by solving the discretized boundary conditions. These steps are explained in detail in Chapter 2.5.1.

2.2.4 Implementation of notches

To study the influence of defects with different sizes, depths, and orientations, notches with variable axial, circumferential, and radial extents are implemented into the present FDM code. Basically, the notches are realized as empty or removed cells in the grid, while the notch boundaries are implemented as stress-free. Fig. 2.3 shows part of an implemented notch with the stress-free boundaries colored in gray.
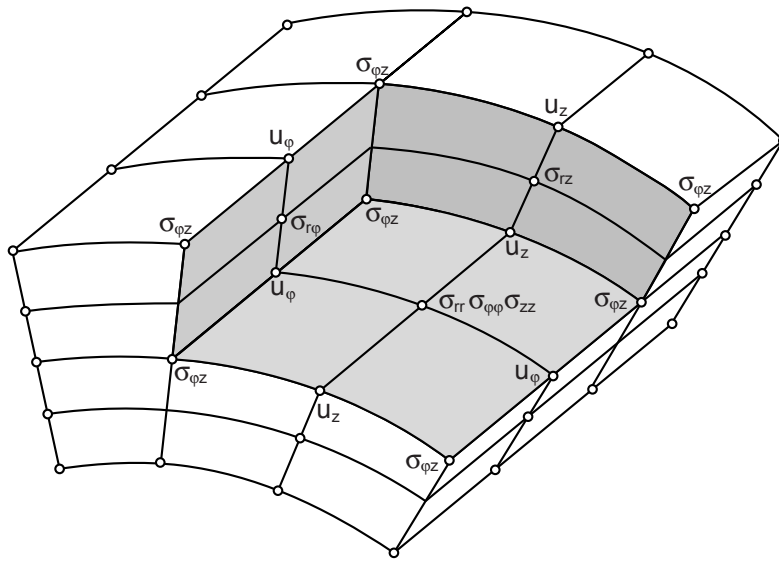
Figure 2.3: The staggered grid allows an easier implementation of stress-free boundaries (colored in gray) at the notches, which are realized as removed cells in the grid.

The goal does not consist in describing the exact interactions at a crack tip or in accurately calculating the stress field in the crack region. The use of notches instead of cracks results in a much easier realization but still enables the numerical generation of scattered fields. However, the stress fields do not match the ones caused by a real defect or notch in an experiment. The simulated wave fields are an important tool for testing the applicability and accuracy of the proposed time reverse numerical simulation method (Chapter 3.). Another reason for the implementation of slots instead of cracks is that the defects used in the experiments are also machined into the tubes using a milling cutter and have the shape of notches. Even if a crack is used in the experiments, its correct shape must not be reproduced in the simulation, since the algorithm with a notch included is only used to verify the method. For the evaluation and detection of the defect in a real experiment, the numerical code without a defect is used.

2.2.5 Numerical examples

To demonstrate the capabilities of the present finite-difference code, two numerical examples are given below.

In the first case, an aluminum tube (mass density $\rho = 2700 \, \text{kg/m}^3$, Young's modulus $E = 7.2 \cdot 10^{10} \, \text{N/m}^2$, Poisson's ratio $v = 0.33$) with a wall thickness of $h = 0.002 \, \text{m}$, a radius of midplane $R = 0.016 \, \text{m}$, and a length of $l = 0.6 \, \text{m}$, is used. The structure is excited axisymmetrically by driving all axial, tangential, and radial displacements of the cross-section at the left end.
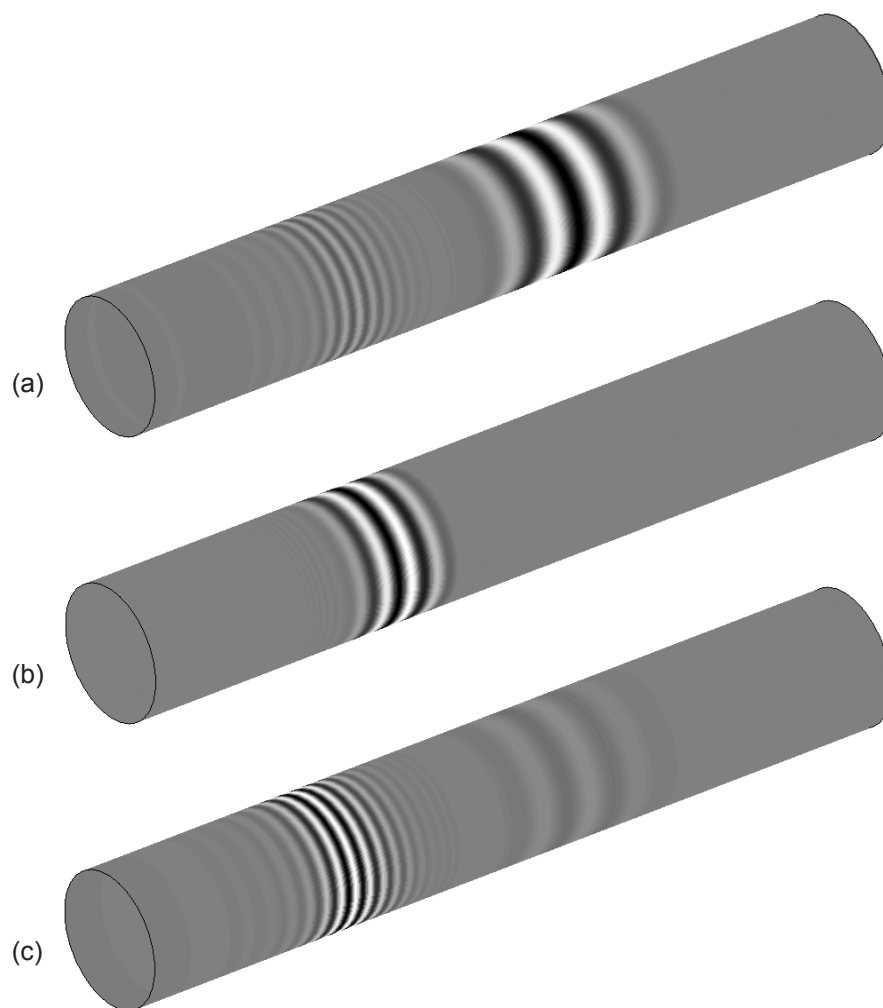
Figure 2.4: Axial (a), tangential (b), and radial (c) displacements at the outer surface of an aluminum tube (data see Table A.1 in Appendix A.1) 81 μs after the initiation of the excitation. All three displacement directions are excited at the front surface at the left end at 150 kHz. The radius is enlarged for better visualization.

The driving function consists of a sine wave with a frequency of 150 kHz multiplied by a Hanning window. In radial and axial direction, 3 and 750 cells are used, respectively (see Table A.1 in Appendix A.1). Due to the axisymmetry of the example, the number of circumferential grid cells is irrelevant. Fig. 2.4 shows the axial, tangential, and radial displacements at the outer surface of the tube 81 μs after the excitation. For the present tube at 150 kHz three axisymmetric modes exist as can be seen in the dispersion diagram Fig. 1.1 in Chapter 1.2.

While the first longitudinal L(0,1) and torsional T(0,1) modes are always present, the second longitudinal mode L(0,2) occurs only when the excitation frequency is above the first axisymmetrical cutoff frequency, which is at about 55 kHz for the present tube. While the displacement field of the torsional mode T(0,1) is only in tangential direction, the two longitudinal modes L(0,1) and L(0,2) are coupled in radial and axial directions, which is visible in Fig. 2.4 (a) and (c). The displacement of the L(0,2) mode with the higher group velocity is primarily in the axial direction, and the slower L(0,1) mode displays a dominant radial displacement field at this particular frequency.

In a second example, an aluminum tube (data see Table A.1 in Appendix A.1) with a length of $l = 0.3$ m is excited at the left end in radial direction at 200 kHz. To generate a scattered field, a notch with an axial, and circumferential length of 1 mm, and 10 mm, respectively, is implemented in the model. While the tube thickness is 2 mm, the notch is only 1 mm deep, starting at the outer surface. Therefore it is named *part-through notch*. The radial displacements at the outer surface of the tube are plotted *42 μs*, *57 μs*, and *65 μs* after the excitation in Fig. 2.5 (a), (b), and (c), respectively. Before the excited waves reach the defect [Fig. 2.5 (a)], the displacement field is axisymmetric. However, after the interaction with the notch, the generated scattered field and the initial waves are non-axisymmetric. This illustrates the need of a three-dimensional algorithm. In radial, circumferential, and axial directions, 5, 100, and 300 cells are used, respectively.
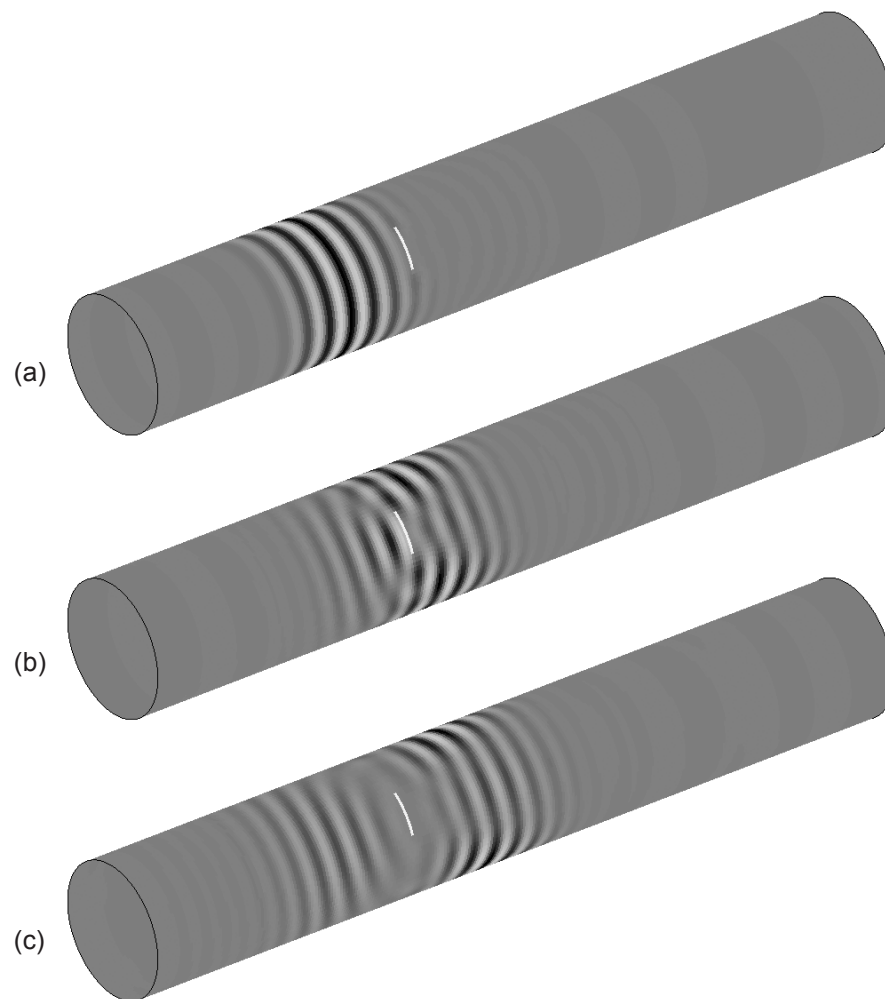
Figure 2.5: Interaction with a circumferential part-through notch in an aluminum tube (data see Table A.1 in Appendix A.1). The radial displacements at the outer surface of the tube are plotted 42 μs (a), 57 μs (b), and 65 μs (c) after the excitation. The front surface at the left end is excited in radial direction at 200 kHz. The radius is enlarged for better visualization.

2.2.6 Validity check

To test the accuracy of the present FDM code, the mechanical energy is observed for the duration of a long-term simulation. Since the implemented linear elastic model is non-dissipative, the total energy as a function of time must remain constant in the conservative system after the excitation. Therefore, the total mechanical energy which is the sum of the kinetic and the strain energy is calculated for each cell after every time step. The summation over the whole structure yields to the total energy. Several simulations with different material, geometrical, excitational, and discretization parameters are performed by Gsell and the author in [23] and show that even for simulations of 120'000 time steps, the deviation of the total energy of 0.01% is negligible.

2.3 Stability

Since finite-difference modeling approximates derivatives by numerical operators using Taylor polynomials, inaccuracies occur. These numerical errors can be separated into phase errors and amplitude errors. The first group of errors, which may also be viewed as frequency-dependent velocity errors, are called numerical dispersion. They cannot be excluded completely but can be reduced to an acceptable level. To prevent these spatial aliasing errors, the shortest wavelength λ_{min} of the propagating modes must be sufficiently sampled in space. This leads to the following criterion for a three-dimensional staggered grid in cylindrical coordinates ([43], [52]), which determines the largest dimension of a grid cell

$$\frac{\lambda_{min}}{max(\Delta r, \Delta \varphi \cdot r_{max}, \Delta z)} > 8 \qquad (2.11)$$

However, even with a spatial sampling of eight grid cells, errors in the wave velocities occur, which negatively affect the accuracy of the simulation. The impact of these errors as well as the necessary sampling rate to avoid them is discussed in Chapter 2.4.

The second group of errors are the amplitude errors. In numerical simulations it is possible that the amplitude increases exponentially with every time step. In this case, the scheme is said to be unstable. The critical value is the maximum size of the time step Δt. The correct stability examination for the original Yee algorithm was first presented by Taflove [51]. Since no exact criterion for cylindrical coordi-

nates in three dimensions can be found in the literature, the main steps of the stability investigation are given below. To determine the critical size of the time step Δt, the von Neumann stability analysis ([27], [13]) is applied to the present code.

First, the equations of motion (2.2) are expressed in terms of displacements only. Therefore, the stress components are replaced using Hooke's law (2.6) and the kinematic relations (2.7). Subsequently, all first and second derivatives of the displacements are approximated with second-order central differences. This results in three equations for u_ξ (in which ξ represents either r, φ, or z) of the form

$$\underset{j,i,k}{\overset{n+1}{u_\xi}} = - \underset{j,i,k}{\overset{n-1}{u_\xi}} + \underset{k}{\overset{T}{a_\xi}} \cdot \underset{j,i,k}{\overset{n}{u_s}} \tag{2.12}$$

Then the harmonic wave ansatz

$$\underset{j,i,k}{\overset{n}{u_\xi}} = \overset{n}{\hat{u}_\xi} \cdot e^{I \cdot (k \cdot \Delta r \cdot k_r + i \cdot \Delta\varphi \cdot k_\varphi + j \cdot \Delta z \cdot k_z)} \tag{2.13}$$

in which k_r, k_φ, and k_z are the components of the wave vector $\boldsymbol{k}$, and I represents the imaginary unit, is substituted into Eqs. (2.12). This leads to

$$\overset{n+1}{\hat{\mathbf{u}}} = -\boldsymbol{I} \cdot \overset{n-1}{\hat{\mathbf{u}}} + \boldsymbol{A} \cdot \overset{n}{\hat{\mathbf{u}}} \tag{2.14}$$

where $\boldsymbol{I}$ is the 3x3-identity matrix and $\hat{\mathbf{u}} = \{\hat{u}_r, \hat{u}_\varphi, \hat{u}_z\}^T$. Matrix $\boldsymbol{A}$ depends on material, geometrical, and discretization parameters and the wave vector $\boldsymbol{k}$. Using

$$\overset{n}{w} = \left\{ \begin{array}{c} \overset{n}{\hat{\mathbf{u}}} \\ \overset{n-1}{\hat{\mathbf{u}}} \end{array} \right\} \quad \text{and} \quad \boldsymbol{G} = \begin{bmatrix} \boldsymbol{A} & -\boldsymbol{I} \\ \boldsymbol{I} & 0 \end{bmatrix} \tag{2.15}$$

Eq. (2.14) can be expressed as

$$\overset{n+1}{w} = \boldsymbol{G} \cdot \overset{n}{w} \tag{2.16}$$

The 6x6 matrix $\boldsymbol{G}$ is called amplification matrix.

As proved by Strikwerda [50], the following condition must apply to all eigenvalues Λ_m of the amplification matrix $\boldsymbol{G}$ in order to guarantee stability

$$|\Lambda_m| \le 1 + g \cdot \Delta t \qquad m = 1, ..., 6 \tag{2.17}$$

Constant g is independent of Δr, $\Delta \varphi$, Δz, Δt, and $\boldsymbol{k}$. To the author's knowledge, its value can neither be calculated, nor is it specified in the literature. Equation (2.17) is called the general von Neumann condition [17] and must be fulfilled if the amplification matrix is a function of the discretization parameters. If $\boldsymbol{G}$ is independent of Δr, $\Delta \varphi$, Δz, Δt, the restricted von Neumann condition

$$\left| \Lambda_m \right| \leq 1 \tag{2.18}$$

must be satisfied.

Eq. (2.18) was solved by Fellinger et al. [13] for a three-dimensional code for isotropic material in Cartesian coordinates (x_1, x_2, x_3). They obtained the following criterion for the time step

$$\Delta t \leq \frac{1}{c_p \cdot \sqrt{\dfrac{1}{\Delta x_1^{\,2}} + \dfrac{1}{\Delta x_2^{\,2}} + \dfrac{1}{\Delta x_3^{\,2}}}} \tag{2.19}$$

where Δx_1, Δx_2, and Δx_3 denote the space increments and c_p the primary wave speed

$$c_p = \sqrt{\frac{\lambda + 2\mu}{\rho}} \tag{2.20}$$

The same result was derived by Taflove [51]. Chen and Chew [6] used the findings of Taflove and Fellinger [Eq. (2.19)] to achieve the following empirical condition for cylindrical coordinates

$$\Delta t \leq \frac{1}{c_{max} \cdot \sqrt{\dfrac{1}{\Delta r^2} + \dfrac{1}{(r_{min} \cdot \Delta \varphi)^2} + \dfrac{1}{\Delta z^2}}} \tag{2.21}$$

This can also be expressed as

$$s = \Delta t \cdot c_{max} \cdot \sqrt{\frac{1}{\Delta r^2} + \frac{1}{(r_{min} \cdot \Delta \varphi)^2} + \frac{1}{\Delta z^2}} \leq 1 \tag{2.22}$$

where s is called the stability factor and c_{max} is the fastest wave velocity. To verify the empirical criterion Eq. (2.21), its performance is investigated by the author.

For this purpose, the largest absolute eigenvalue $|\Lambda|_{max}$ of the amplification matrix G and the stability factor s are calculated for different time steps, and the comparison is shown in Fig. 2.6. An aluminum tube (material and geometrical parameters are given in Table A.1 in Appendix A.1) with a length of $l = 0.08\,\text{m}$, is used for the simulations. While geometrical, material, and spatial discretization parameters (6, 120, and 100 cells in radial, circumferential, and axial direction, respectively) are kept constant, the time step Δt is varied.
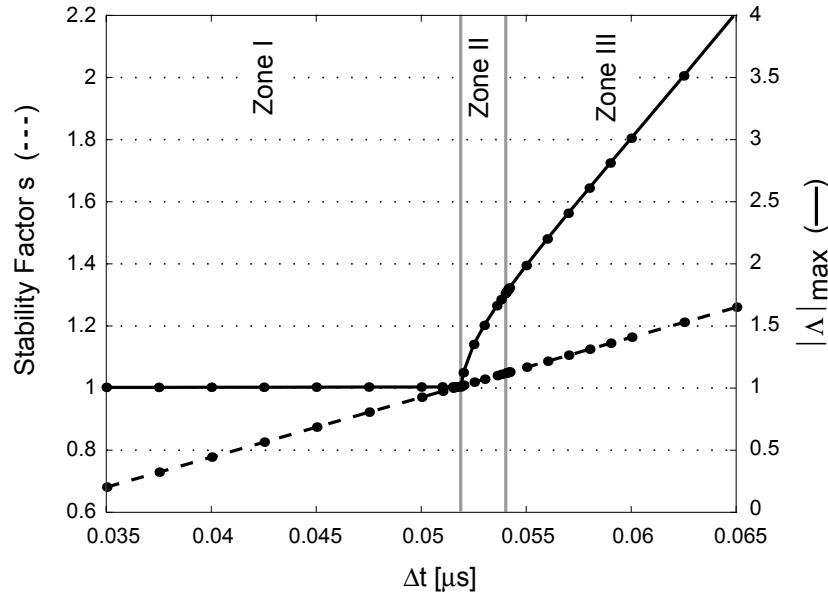
Figure 2.6: Comparison of the stability factor s (dashed line) and the largest absolute eigenvalue $|\Lambda|_{max}$ of the amplification matrix G (solid line) for different time steps Δt (dots).

For each time step, the largest eigenvalue $|\Lambda|_{max}$, which is always greater than one, and the stability factor s are calculated and plotted in Fig. 2.6 (black dots). Then, the simulations with the corresponding parameters are run and visually observed to check wether they are stable or not. As excitation all three displacement components at one point are driven with a sine wave with a frequency of 200 kHz multiplied by a Hanning window.

The region depicted in Fig. 2.6 can be divided into three zones. Zone I is the area in which the stability factor s is smaller than one and the largest absolute eigenvalues are only slightly larger than one and approximately constant. Stability is always guaranteed in this region. In zone II the eigenvalues increase remarkably

and s is larger than one. While the slope of the stability factor curve (dashed line) is more or less constant, definite changes in the gradient of the eigenvalues can be observed. The FDM scheme is still stable in region II. In zone III stability can no longer be achieved. The problem is that there is no noticeable change in the stability factor or the eigenvalue curve at the border between zone II and III.

The investigation shows that stability can even be guaranteed if the stability factor is slightly larger than one. This finding was also noticed by Chen and Chew who realized that their criterion [Eq. (2.21)] could be extended. The reason for this is that they based their stability condition on the results of Fellinger and Taflove [Eq. (2.19)] who used the restricted [Eq. (2.18)] instead of the general von Neumann criterion [Eq. (2.17)]. However, one must be careful when using stability factors larger than one. While the border between zone I and II is always situated at the time step where s equals one, the position of the border between zone II and III depends on the material, geometrical, and discretization parameters. Consequently, the upper limit for s which would still assure stability cannot be determined. Therefore, the author suggests to use Eq. (2.21) as a stability condition.

2.4 Numerical dispersion

As mentioned in Chapter 2.3, numerical dispersion (grid dispersion) is the most significant numerical problem and as such limits the usefulness of discretization schemes for wave equations. This numerical artifact causes phase speeds and group velocities to become functions of the discretization parameters. In theory, it is always possible to choose a grid size small enough to ensure that the errors due to numerical dispersion are outside the range of interest and can be neglected. In practice, the limitations on the sampling rate are determined by the computational performance of the central processing unit (CPU), the availability of memory, and the patience of the user.

The numerical dispersion relation was first investigated by Taflove [51] for the original Yee algorithm. Marklein [34] extended it to the two- and three-dimensional case of elastic waves, and Shlager et al. [45] used it to compare the dispersion error of different FD methods. Taflove showed that the numerical phase velocity diminishes with increasing grid sizes and, for coarse grids, can even sink to zero. Consequently, it can be concluded that a numerical low-pass filter is inherent in the finite-difference schemes. Waves with a very short wavelength that are sampled less than three times over a wavelength can no longer propagate.

Different sampling rates are suggested in the literature. For a second-order code, generally eight to ten grid points per minimum wavelength are required. This is the condition given in Eq. (2.11). By satisfying this restriction for the grid size, qualitatively nice wave propagation phenomena without oscillations can be simulated. However, when playing back experimental results (Chapter 4.) fulfilling Eq. (2.11), all defects were consistently attributed to a position to far away as compared to the actual position of the defect. This is indicative of deviations in the group (and phase) velocity in the simulation. Since errors in the phase and group velocity caused by numerical dispersion are cumulative, they must be lowered even more for long-term simulations in large structures. Therefore, the ratio between the group velocity and the number of grid cells per minimum wavelength is investigated in the next section for the second-order code.

2.4.1 Grid dispersion in the second-order scheme

To examine the influence of the grid size, a numerical axisymmetric example is repeated several times, varying only the axial discretization parameter Δz. An aluminum tube with material and geometrical parameters according to Table A.1 in Appendix A.1 is excited axisymmetrically in axial and radial direction at one of the free ends. The driving function for the displacements is a sine in a Hanning window at $200 \, \text{kHz}$. The axial and radial displacements are recorded as a function of time at different axial positions along the structure. Two different simulation series are performed with this configuration. In the first run, the time steps Δt are kept constant, so that stability is guaranteed for the smallest grid. The result is a time oversampling for larger Δz. In the second set, the time steps are always adjusted to obtain a stability factor just below one. The comparison of these two series showed that the time step does not affect the numerical dispersion as long as stability is guaranteed. While three cells are used in radial and circumferential directions for all simulations, the number of grid points in axial direction is variable due to the different sizes of Δz. The axisymmetry of the examples justifies the few cells in the tangential direction.

Fig. 2.7 shows the normalized axial displacements of the outer surface of the tube $0.36 \, \text{m}$ away from the excitation for two different grid sizes. Two longitudinal wave modes are visible. The faster mode L(0,2) has a wavelength of about $26 \, \text{mm}$, the second L(0,1) mode about $8 \, \text{mm}$, which corresponds to λ_{min}.
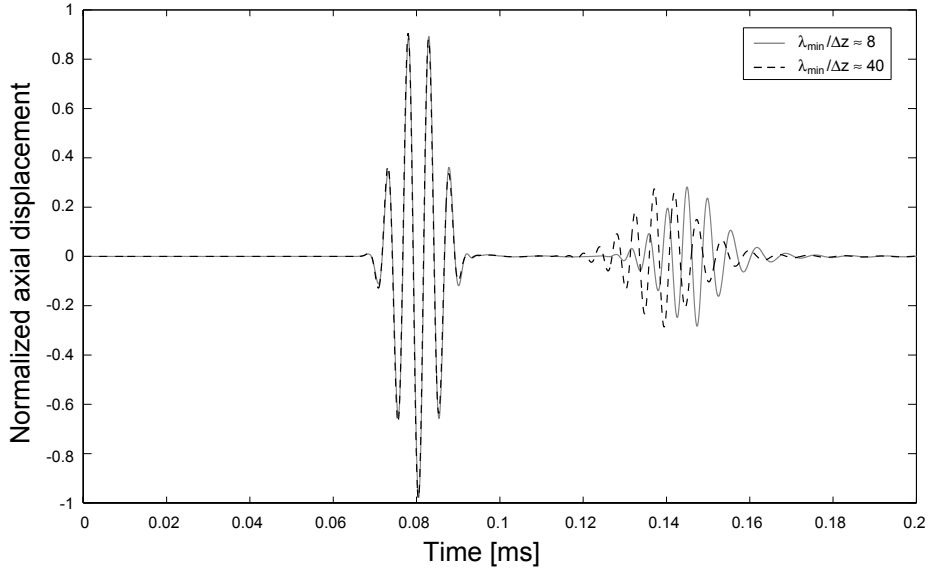
Figure 2.7: Normalized axial displacement for two different sampling rates in axial direction. In the case of the solid gray line, the shortest wavelength λ_{min} is sampled about eight times. The dashed black curve results from a sampling rate of approximately forty.

The solid gray line is the result of a simulation with $\Delta z = 1 \text{ mm}$, and the dashed black line for $\Delta z = 0.2 \text{ mm}$. While the two curves match almost perfectly for the first mode [L(0,2)], a noticeable difference is observed in the slower L(0,1) mode. This is due to the fact that the first mode with a wavelength of 26 mm is sampled sufficiently in space for both Δz with 26 and 130 cells per wavelength, respectively, whereas the sampling rate of the L(0,1) mode with the shorter wavelength $\lambda_{min} \approx 8 \text{ mm}$ becomes critical. Using the finer grid, the number of samples per wavelength is still about forty, but with $\Delta z = 1 \text{ mm}$ the sampling rate drops to approximately eight. Although this value still fulfills the criterion Eq. (2.11), the simulated wave form is no longer accurate, and big differences in the arrival times of the L(0,1) mode result. Fig. 2.7 explains the errors in the time reverse simulations of the experiments caused by the excessively slow group velocities. Simulations with different sampling rates Δz are performed and compared to the results of Fig. 2.7. The results of the L(0,1) mode shift from the solid gray curve (eight samples) towards the dashed black curve (forty samples) for increasing sampling rates. For more than forty cells per minimum wavelength, the achieved time signals remain constant and match the dashed black curve.

To establish the minimum sampling rate for accurate results, the group velocities are determined for different grids in several simulations. To this end, the displacements are recorded at different axial positions as functions of time for each spatial sampling rate Δz. In order to calculate the group velocities of a mode, the difference in the arrival times Δt_g must be determined from the signals at two positions which are Δz_g apart. Then the group velocity is defined as

$$ c_g = \frac{\Delta z_g}{\Delta t_g} \tag{2.23} $$

Due to numerical and physical dispersion of the simulated wave modes, which means that different frequencies travel at different velocities, distorsion arises. Even for a narrow-band signal, the shape of the pulse is changed slightly and one must be careful to evaluate the correct time difference Δt_g. It is not possible to measure the difference between characteristic points, such as the beginning, end or maxima of the pulse, since the corresponding points cannot be identified at two locations.

However, by applying the main idea of the Wavelet Transform (see Refs. [39], [48]), the author developed a method to determine the time differences. In this time-frequency analysis method, a wavelet with a defined frequency content is compared to a signal in a specific time range. The wavelet is a short signal which is limited in time and frequency domain. The convolution between the wavelet and the signal is calculated and the result indicates, how similar the two signals are at the corresponding time in the specific frequency range. Further information about the Wavelet Transform and its applications to wave propagation phenomena are provided by the author in Ref. [29].

This convolution method is applied to the simulated time signals from two different locations, which is explained in Fig. 2.8.
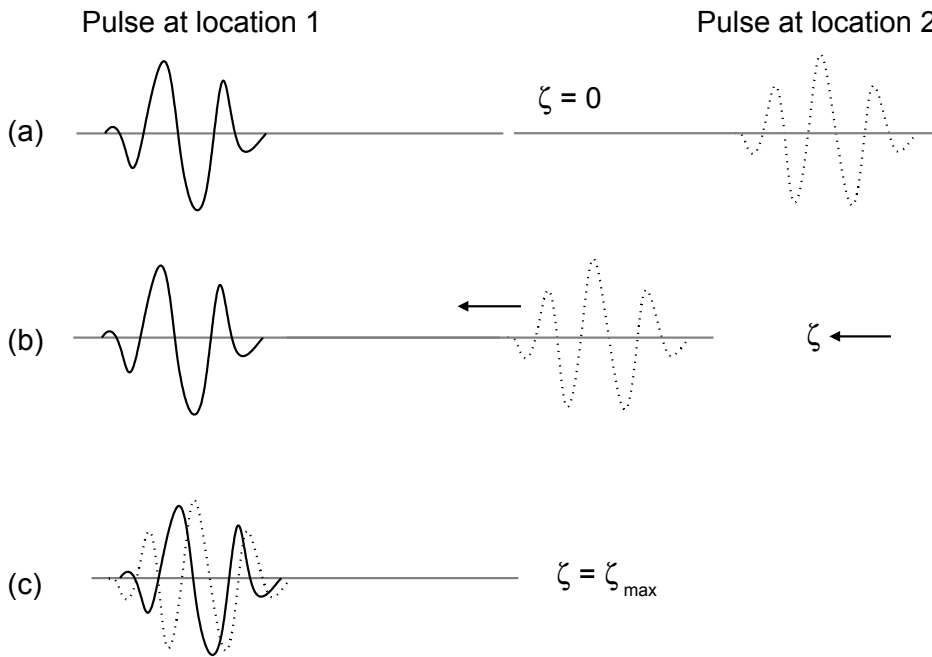
Figure 2.8: The major steps of the convolution method to determine the time difference between to dispersive signals.

The convolution of the time signals is calculated, which is the sum of the element-wise multiplication of the two discrete vectors. At the beginning, the convolution function is zero since the two signals do not overlap [Fig. 2.8(a)]. Now the second time signal (dotted line) is shifted in the time domain towards the signal at location one (solid curve), and the convolution is calculated again [Fig. 2.8(b)]. By repeating this procedure, one obtains the convolution as a function of the time shifts ζ. The convolution reaches the maximum value when the two compared signals achieve the optimal overlap [Fig. 2.8(c)]. If ζ_{max} is the number of time shifts where the maximum value of the convolution function is received, the time difference is expressed as

$$\Delta t_g = (\zeta_{max} - N) \cdot \frac{1}{f_s} \tag{2.24}$$

where N is the number of points of the digitized time signals, and f_s is the sampling frequency.

With this method, the time differences and the group velocities for the slower wave mode (with the shorter wavelength) are evaluated for different grid parameters Δz. In Fig. 2.9, the normalized group velocity is plotted versus the number of grid cells per minimum wavelength.
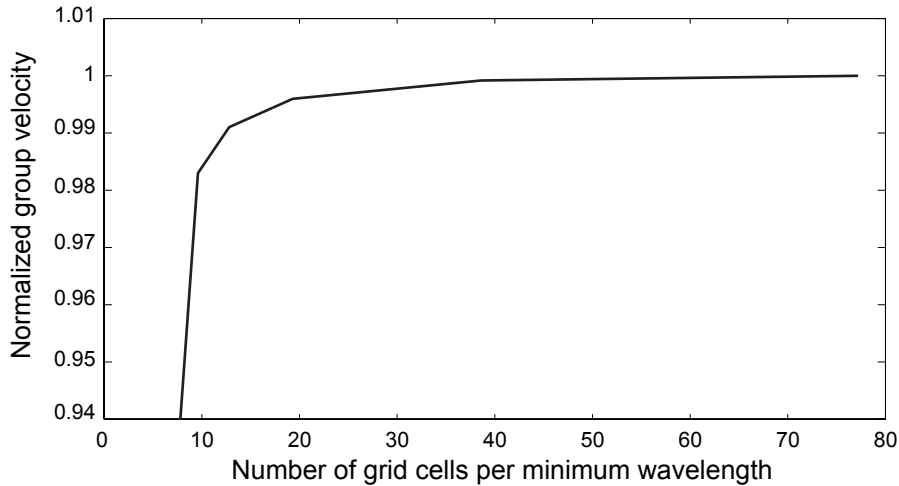
Figure 2.9: Normalized group velocity as a function of the sampling rate for the minimum wavelength for the second-order scheme.

The curve in Fig. 2.9 shows that with a sampling rate of ten the group velocity is still underestimated. To eliminate this error, at least forty cells per shortest wavelength are necessary. Therefore, a very fine grid must be chosen to obtain accurate group velocities, which is essential for large structures and long-term simulations. In addition to the tremendous amount of memory required, another problem is the size of the time step Δt. In order to satisfy the stability criterion, a very small time step is necessary for fine grids. The result is a large increase in the number of floating point operations (flops) to simulate the same period of time, which leads to very long computing times. Since the simulations of large three-dimensional structures with the second-order code exceed the computational limits of today's computers, it is inevitable to use a fourth-order accurate scheme.

2.5 Fourth-order finite-difference method

As described in the previous section, the use of second-order central differences is no longer possible for the simulation of large three-dimensional structures. Therefore, especially in the field of geophysics, where P- and S-waves are investigated and large regions must be simulated, higher-order finite-differences are used to approximate the derivatives in the wave equation. Dablain [7] showed that computational efficiency can be achieved by using higher-order differences. Particularly in simulations where a fine grid is necessary because of the cumulative errors of the numerical dispersion, rather than due to the need to resolve fine geometrical features, much coarser grids can be used with higher-order finite-differences. A disadvantage of higher-order central differences is the more complex implementation of the boundary conditions, which is discussed later.

The following algorithm is based on central differences which are second-order accurate in time and fourth-order accurate in space. Similar to the second-order finite-difference method, one starts with the equations of motion (2.2), but in this case, the first spatial derivatives are approximated by fourth-order accurate differences. Therefore, more terms of the Taylor expansions are used to approximate the first-order derivatives. E.g. the expansion for the shear stress component $\sigma_{rz}(z_j + \Delta z \, / \, 2)$ is given as

$$
\sigma_{rz}_{j+1,i,k} = \sigma_{rz}_{j,i,k} + \left(\frac{\Delta z}{2}\right) \cdot \left(\frac{\partial}{\partial z} \, \sigma_{rz}_{j,i,k}\right) + \frac{1}{2} \cdot \left(\frac{\Delta z}{2}\right)^2 \cdot \left(\frac{\partial^2}{\partial z^2} \, \sigma_{rz}_{j,i,k}\right)
$$

$$
+ \frac{1}{6} \cdot \left(\frac{\Delta z}{2}\right)^3 \cdot \left(\frac{\partial^3}{\partial z^3} \, \sigma_{rz}_{j,i,k}\right) + \frac{1}{24} \cdot \left(\frac{\Delta z}{2}\right)^4 \cdot \left(\frac{\partial^4}{\partial z^4} \, \sigma_{rz}_{j,i,k}\right) + O[(\Delta z)^5]
$$

(2.25)

The positions of the different values within the discrete structure are shown in Fig. 2.10, where part of an axial line of the staggered grid is plotted.
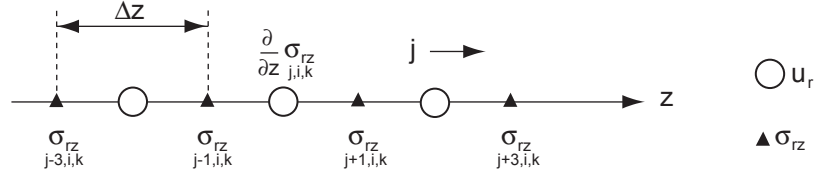
Figure 2.10: Part of an axial line of the staggered grid showing the allocation of the stress component σ_{rz} and its first derivatives with respect to the axial coordinate z.

To eliminate the second, third, and fourth derivatives in (2.25), the Taylor series for

$$\sigma_{rz}_{j-1,i,k} = \sigma_{rz}\left(z_j - \frac{1}{2}\Delta z\right) \qquad \sigma_{rz}_{j+3,i,k} = \sigma_{rz}\left(z_j + \frac{3}{2}\Delta z\right) \qquad \sigma_{rz}_{j-3,i,k} = \sigma_{rz}\left(z_j - \frac{3}{2}\Delta z\right)$$

are calculated accordingly. Solving for the first derivative with respect to z leads to the fourth-order central differences

$$\frac{\partial}{\partial z}\sigma_{rz}_{j,i,k} = \frac{1}{24\Delta z}\left[\sigma_{rz}_{j-3,i,k} - 27\,\sigma_{rz}_{j-1,i,k} + 27\,\sigma_{rz}_{j+1,i,k} - \sigma_{rz}_{j+3,i,k}\right] + O[(\Delta z)^4] \quad (2.26)$$

In Eqs. (2.2) and (2.7), all first derivatives with respect to the axial and circumferential coordinates z and φ are replaced with the corresponding fourth-order central differences. Since thin-walled structures are investigated in this thesis and the wavelength in the applied frequency range are large compared to the wall thickness, the derivatives with respect to the radial coordinate r are still approximated with second-order differences only.

Analogous to the second-order scheme, three explicit equations for the displacements at the time step $n + 1$ and six equations for the stress components result. The equations are of the same form as Eqs. (2.5) and (2.9) but the vectors $\boldsymbol{\sigma}_s$ and $\boldsymbol{u}_s$ contain the surrounding stress and displacement components of the larger grid region $j \pm 3$, $i \pm 3$, $k \pm 1$. Consequently, the calculation of the new components requires many more neighboring values, which significantly complicates the implementation. As an example, the vectors $\boldsymbol{\sigma}_s$, $\boldsymbol{u}_s$, $\boldsymbol{a}_r$, and $\boldsymbol{b}_{rr}$ [see Eqs. (2.5) and (2.9)] are given in Eqs. (A.7) - (A.10) in Appendix A.3. Since the present scheme is only fourth-order accurate in axial and circumferential but not in radial direction and the time, it would be more appropriate to call it a *quasi-fourth-order code*. However, the author refers to it as a fourth-order code, although this is not quite correct. The stability criterion Eq. (2.21) is used successfully with the fourth-order algorithm.

2.5.1 Boundary conditions for the fourth-order code

While the fourth-order scheme can manage much coarser grids, which saves computational time as well as memory requirements, there is one major drawback. Since more surrounding components are necessary, the implementation of the boundary conditions becomes a difficult task. Similar to the second-order scheme, a fictitious area which holds all additional components is introduced outside the structure. Because the region containing the necessary values for evaluating the new displacements and stresses is larger, the fictitious layers consist of three levels of grid cells in axial and one level in radial direction. In Fig. 2.11 two sectional views of the discretized structure are depicted. The sections show the inner left area of a tube (hatched) with a wall thickness h and a radius of midplane R.
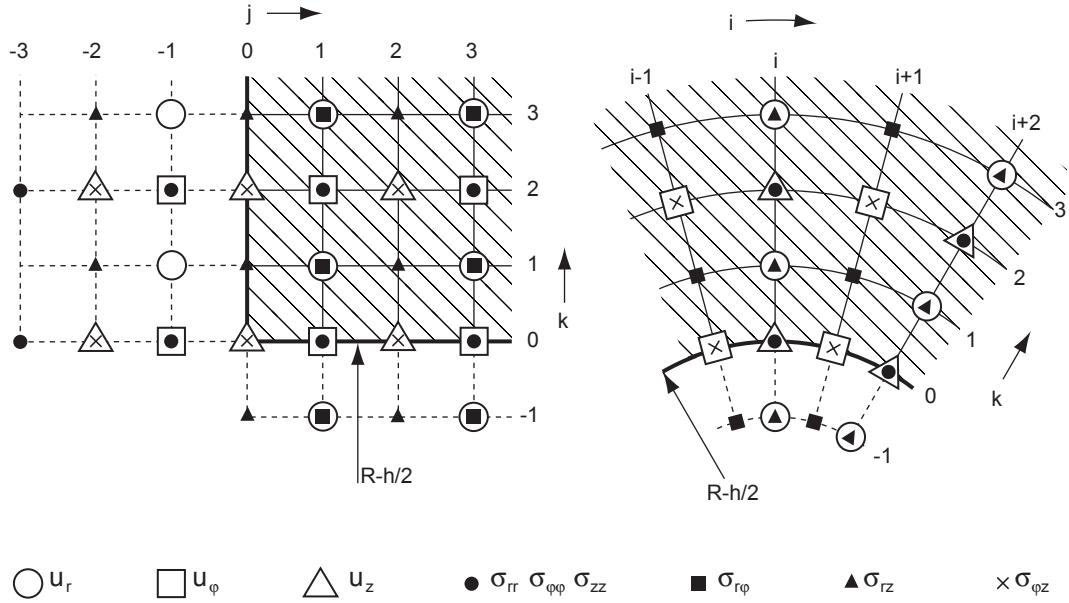
Figure 2.11: Longitudinal (left) and transverse (right) sectional views of the discretized structure (hatched area) and the necessary fictitious layers. The stress-free boundaries of the structure are marked as thick black lines.

Since the tube is closed completely in circumferential direction, no boundary conditions must be fulfilled there. However, at the left and right axial end and at the inner and outer surface of the tube, stress-free boundaries are implemented.

For the inner surface ($k = 0$) the necessary fictitious components are

$$\sigma_{r\varphi} \, , \quad \sigma_{rz} \, , \quad u_r \atop {}_{j,i,-1} \quad {}_{j,i,-1} \quad {}_{j,i,-1} \tag{2.27}$$

The indices j, i, and k (which is -1 for this particular fictitious layer) define the axial, circumferential, and radial positions of the corresponding components on the grid according to Fig. 2.11. The two stress components are calculated by using linear interpolation in radial direction and the zero stress relations (2.10), which yields

$$\sigma_{r\varphi} \atop {}_{j,i,-1} = - \sigma_{r\varphi} \atop {}_{j,i,1} \qquad \sigma_{rz} \atop {}_{j,i,-1} = - \sigma_{rz} \atop {}_{j,i,1} \tag{2.28}$$

To determine the fictitious radial displacements, Eqs. (2.6) and (2.7) are used to calculate σ_{rr}. The first derivatives are approximated in axial and circumferential directions by fourth-order, and in radial direction by second-order central differences. Then Eq. (2.10) is solved for u_r by fulfilling the boundary condition $\sigma_{rr} = 0$. This leads to an explicit equation for the calculation of the radial displacement of the fictitious layer as a function of the surrounding displacement values, the discretization parameters, the radial position r_k (which is $R - h\,/\,2$ for the inner surface), and Poisson's ratio ν.

$$
u_{r \atop j,i,-1} = f\left(\Delta r, \Delta\varphi, \Delta z, \nu, r_k, u_{r \atop j,i,1}, u_{\varphi \atop j,i-3,0}, u_{\varphi \atop j,i-1,0}, u_{\varphi \atop j,i+1,0}, u_{\varphi \atop j,i+3,0}, u_{z \atop j-3,i,0}, u_{z \atop j-1,i,0}, u_{z \atop j+1,i,0}, u_{z \atop j+3,i,0} \right) \quad (2.29)
$$

To satisfy the stress-free conditions at the left end ($j = 0$), the following fictitious values, which are also shown in Fig. 2.11, must be determined.

$$
\sigma_{zz \atop -3,i,k}, \quad \sigma_{zz \atop -1,i,k}, \quad \sigma_{rz \atop -2,i,k}, \quad \sigma_{\varphi z \atop -2,i,k}, \quad u_{r \atop -1,i,k}, \quad u_{\varphi \atop -1,i,k}, \quad u_{z \atop -2,i,k} \quad (2.30)
$$

According to Graves [21], the stress components are again evaluated by linear interpolation in axial direction, which leads to

$$
\sigma_{zz \atop -3,i,k} = -\,\sigma_{zz \atop 3,i,k} \qquad\qquad \sigma_{zz \atop -1,i,k} = -\,\sigma_{zz \atop 1,i,k} \qquad\qquad (2.31)
$$

$$
\sigma_{rz \atop -2,i,k} = -\,\sigma_{rz \atop 2,i,k} \qquad\qquad \sigma_{\varphi z \atop -2,i,k} = -\,\sigma_{\varphi z \atop 2,i,k} \qquad\qquad (2.32)
$$

For the calculation of the fictitious displacements one must again use Eqs. (2.6) and (2.7) to evaluate the stress components at the boundary. In order to determine a rule for the desired displacement components, the first derivatives in axial direction are only approximated with second-order central differences. This leads to a different order of accuracy of the scheme at the boundaries but is the only possibility for implementing the stress-free surfaces. Solving

$$
\sigma_{rz \atop 0,i,k} = 0 \qquad\qquad \sigma_{\varphi z \atop 0,i,k} = 0 \qquad\qquad \sigma_{zz \atop -1,i,k} = -\,\sigma_{zz \atop 1,i,k} \qquad\qquad (2.33)
$$

leads to similar functions as Eq. (2.29) for $u_{r \atop -1,i,k}$, $u_{\varphi \atop -1,i,k}$, and $u_{z \atop -2,i,k}$.

Special care must be taken in the *ring-regions* at the inner and outer surface at the axial ends. In these areas some of the values used to calculate the fictitious components are no longer located within the structure but become fictitious points too. They must be replaced by using the boundary conditions on the inner and outer surface.

These different rules for calculating all values of the fictitious layers illustrate the difficulties encountered by implementing the correct boundary conditions in the present code. Example: The calculation of the fictitious axial displacements at the left end involves seventeen displacement values. The situation becomes even more complicated if one applies fourth-order differences in radial direction instead of second-order approximations.

2.5.2 Grid dispersion in the fourth-order scheme

The reason for the implementation of a fourth-order algorithm is the higher accuracy which leads to smaller numerical dispersion. To verify this and to determine the minimum sampling rate, the group velocities are once again determined as a function of the axial cell size Δz. Consequently, the same numerical examples described in Chapter 2.4.1 are also performed for the present fourth-order code.
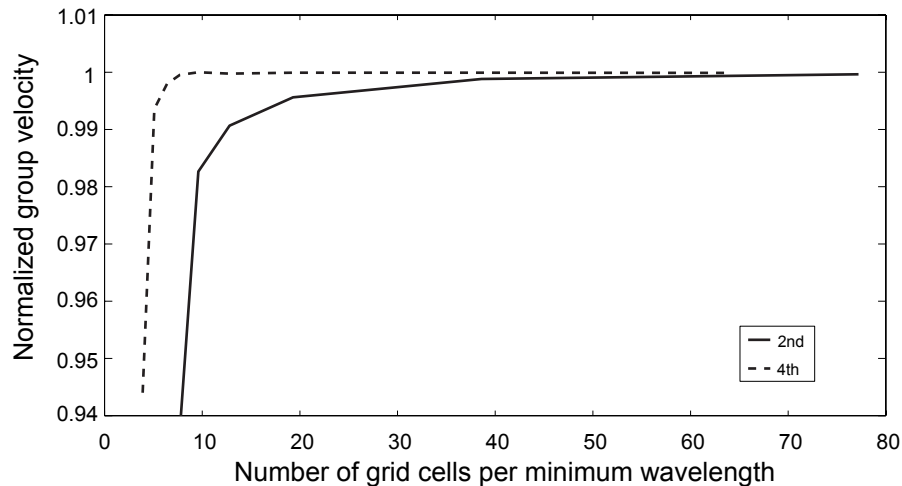

Figure 2.12: Normalized group velocity as a function of the sampling rate for the minimum wavelength for the second- (solid) and fourth-order scheme (dashed).

Fig. 2.12 depicts the normalized group velocities for the second-order (solid line) and fourth-order (dashed curve) as a function of the number of grid cells per minimum wavelength. The curves show that at a sampling rate of only about eight, one already obtains the accurate group velocity for the fourth-order scheme, while the second-order code still produces significant deviations. This implies that a much coarser grid can be used with the fourth-order scheme in order to bring about the desired reduction of computing time and memory requirement and still achieves a high accuracy. The achieved results justify the costs of implementing a higher-order algorithm.

### 2.5.3 Comparison of the second- and fourth-order algorithms

To compare the two codes with respect to accuracy and computational performance, the examples previously used to investigate the numerical dispersion (see Chapter 2.4.1 and Table A.1 in Appendix A.1) are examined again. In Fig. 2.13 the normalized radial displacements for the fourth-order code with a sampling rate of eight (thick gray line), and the two results for the second-order accurate scheme with eight (solid black line) and forty samples (dashed black line) per minimum wavelength are plotted.
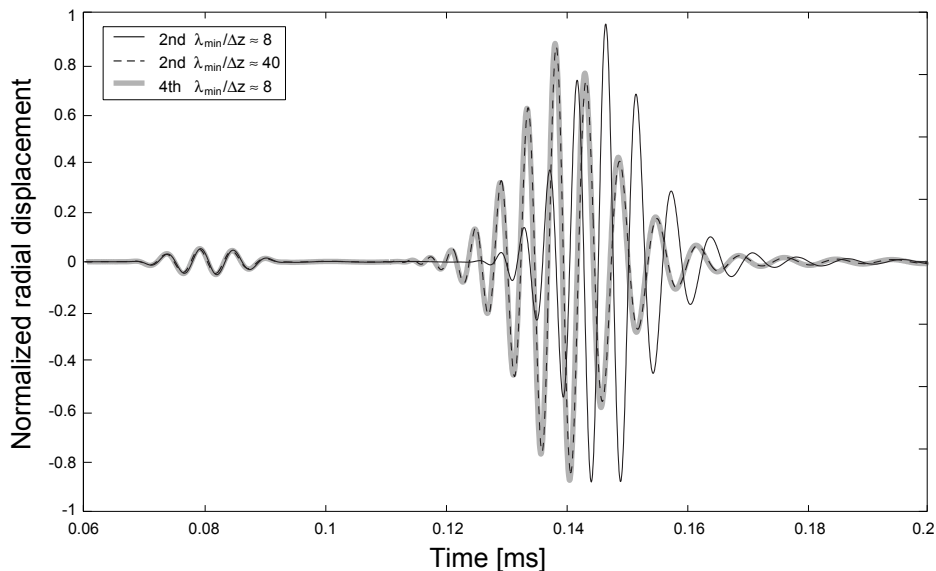
Figure 2.13: Comparison of the normalized radial displacements for the second- and fourth-order schemes. The tube (data see Table A.1 in Appendix A.1) is excited axisymmetrically in axial and radial direction at 200 kHz. The black curves result from the second-order code with an axial sampling rate of eight (solid black line) and forty (dashed black line). The thick gray line represents the result of the fourth-order algorithm where the shortest wavelength is sampled about eight times.

Very good agreement is found between the fourth-order result and the curve from the second-order code with the higher sampling rate. However, for the lower sampling rate the expected deviation appears due to undersampling in axial direction. The comparison shows that for the axisymmetric example the same results can be achieved with five times less cells in axial direction using the fourth-order code.

The resulting savings in the area of memory requirements and calculating time are even more crucial in the case of non-axisymmetric wave propagation simulations. In order to assess the actual savings with regard to floating point operations, memory usage and simulation times, a numerical experiment with a point source is first evaluated using the second-order scheme with a sampling rate of forty (in circumferential and axial directions), and then with the fourth-order code using eight cells per minimum wavelength. To generate a non-axisymmetric wave field, a point source is applied to a tube with a wall thickness $h = 0.002 \, \text{m}$, radius of midplane $R = 0.012 \, \text{m}$, and length $l = 0.15 \, \text{m}$. The material parameters are given in Table A.2 in Appendix A.1. The radial displacements at a given axial and circumferential position are excited at $200 \, \text{kHz}$, which leads to a minimum wavelength $\lambda_{min} \approx 8 \, \text{mm}$. Fig. 2.14 shows the radial displacements at the outer surface of the tube at three different times.
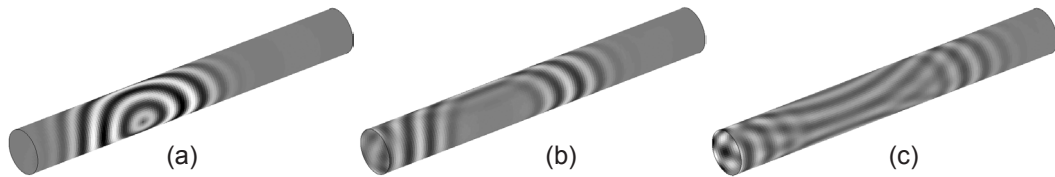
Figure 2.14: Radial displacements at the outer surface, 18 µs (a), 24 µs (b), and 32 µs (c) after the initiation of the excitation. The aluminum tube (data see Table A.2 in Appendix A.1) is excited radially in one single point at 200 kHz.

The radial displacements at the outer surface are recorded at the same circumferential position in the middle of the tube with respect to the axial direction, which is 25 mm away from the excitation. Fig. 2.15 shows part of these time signals for the two simulations. The first wave packet represents the wave propagating directly in the axial direction from the excitation to the measurement point. The second waves have travelled once around the circumference. The result of the second-order scheme is plotted as a dashed black curve, while the thick gray line represents the signal from the fourth-order code. The small deviations are caused by the group velocity of the second-order simulation, which is still slightly underestimated (see Fig. 2.12).
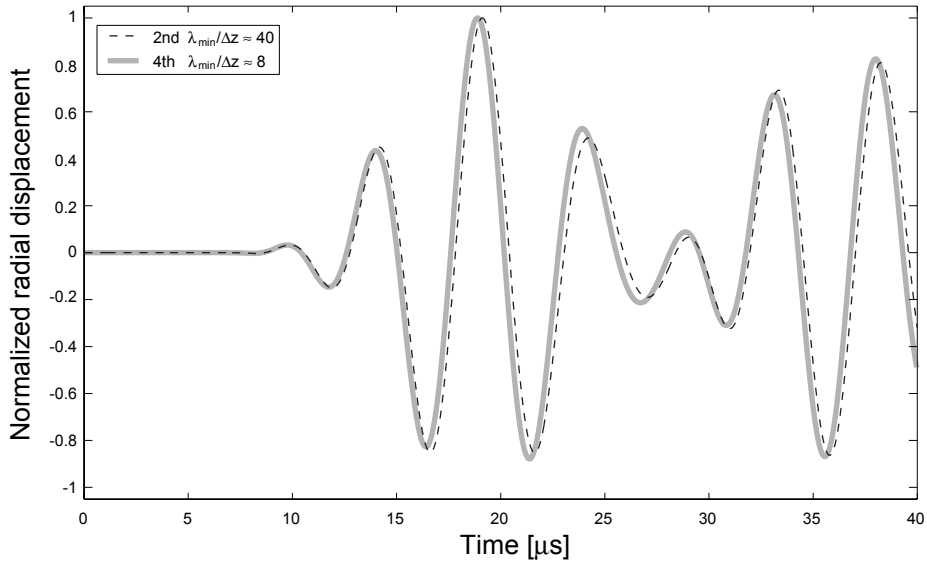
Figure 2.15: Comparison of the normalized radial displacements for the second- and fourth-order schemes. The dashed black curve results from the second-order code with a sampling rate of forty. The solid gray line represents the result of the fourth-order algorithm, where the shortest wavelength is sampled about eight times.

Since in the non-axisymmetric cases the guided waves travel mainly in two directions for the chosen frequencies, sufficiently fine grids must be used in axial and circumferential directions. Consequently, the saved memory is in proportion to the square of the ratio of the sampling rates. In the following table, the important computational parameters for the two simulations are listed.

Parameter	Second-order	Fourth-order	Percentage [%]
sampling rate	40	8	20
cells in axial direction	750	150	20
cells in tangential direction	400	80	20
cells in radial direction	3	3	100
total number of cells	900'000	36'000	4
time step Δt [s]	$1*10^{-8}$	$4*10^{-8}$	400
memory requirements [MB]	454	20	**4.4**
floating point operations	$3.5*10^{11}$	$4.9*10^{9}$	**1.4**
simulation time [min.]	351	5	1.4

Table 2.1: Comparison of the computational parameters between the second- and fourth-order finite-difference schemes. The last column shows the ratios between the values of the two codes.

42

The ratio between the parameters of the codes are listed in the last column of Table 2.1. The two most important values with respect to the simulation of large structures are the number of floating point operations (flops) and the required memory. The savings achieved by using the fourth-order code are 98.6% and 95.6%, respectively, for these two parameters, which demonstrates the significant advantage of higher-order schemes. In order to further validate the fourth-order algorithm, the mechanical energy could be observed according to Chapter 2.2.6. However, due to the good agreement between the second- and fourth-order codes, this validation was not performed in the present work.

2.6 Conclusions

The three-dimensional finite-difference code in cylindrical coordinates with second-order central differences is a valuable tool for the study and visualization of wave propagation phenomena. The implementation of notches enables the generation of scattered wave fields and the verification of the time reverse method (see Chapter 3.3). The von Neumann stability analysis explains why the stability factor can even be slightly larger than one and confirms the empirical stability criterion found in the literature. However, an accurate simulation of large structures is not possible with the second-order code because the computational requirements exceed the available hardware. This is mainly due to the very fine grid and the correspondingly small time steps which are necessary to minimize the errors caused by numerical dispersion. For this purpose, a three-dimensional quasi-fourth-order accurate scheme has been implemented in cylindrical coordinates for the first time. The comparison of the two codes shows very good agreement in the results as well as a drastic reduction - indeed more than 95% - in the areas of memory requirements and calculating time when using the higher-order scheme. This enables the long-term simulations of large structures, which is necessary for the evaluation of the experiments.
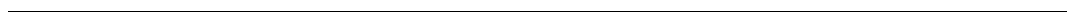
3. TIME REVERSE NUMERICAL SIMULATION

3.1 The time reversal method

3.1.1 Introduction

When a phenomenon or event is filmed, the movie can be played back in reverse, giving the impression of going back in time. Fink [14] used the following thought experiment to see if the actual event, instead of the filmed image, can also be reconstructed in reverse chronology.

For instance, can the scattered pieces of an exploded block be used to reconstitute the original structure? Imagine the block to be surrounded by a closed layer, which is crossed by all the particles after the explosion. The position, time of impact and velocity of each particle is measured and recorded when this surface is penetrated. Then, the same speed is applied in opposite direction to each particle at the appropriate time at the corresponding intersection points on the layer. If the slowest particle, i.e. the last one to arrive, is sent back first, and the fastest one last, the initial block should be reconstructed at its origin position. However, this type of experiment only works if the information (such as position, velocity, and time of impact) for each particle is resolved with infinite precision. The explanation of this is the phenomenon of chaos in classical mechanics. According to this theory, a small change in a particle's initial position can result in a major change in its final position and therefore makes such time reversal experiments impossible.

Another example described by Fink [15] uses a ball which is shot through a fixed array of randomly arranged obstacles. Even in simulation, the ball cannot be played back. Due to minor truncation errors made by the computer, the ball will miss an obstacle sooner or later, which changes the outcome completely. And in a real experiment, it is impossible to start the ball in the exact direction with the appropriate velocity.

Since wave propagation is linear, a minor change in the initial wave results only in a small change of the final wave. Therefore, time reversal can be applied to all wave phenomena, as long as the following restrictions are fulfilled.

3.1.2 Basic principles and applications

The time reversal method can be applied to every phenomenon described by equations which contain only second-order derivatives (or, more general, derivatives of even order) with respect to time t. Equations of this type are called time-reversal-invariant equations. For each solution $u(r, t)$, there exists a second solution of the form $u(r, -t)$, because the second derivative of $u(r, t)$ is identical to that of $u(r, -t)$. Another restriction for the present approach demands that the medium be non-dissipative. However, it might be possible to reverse the attenuation as well, but this was not taken into consideration in this work.

The time reversal experiments typically consist of two steps. First, a wave field is generated either by a source or by scattering at an obstacle. This wave field $u_s(r, t)$ is measured at different fixed positions (defined by r) as a function of time and stored. The duration of this recording is given by T. Next, the measurements at each position are reversed in time, which results in the time reversed signals

$$u_{TR}(r, t) \;=\; u_s(r, T-t) \tag{3.1}$$

In the second step, the measurement positions are used as sources where the time reversed signals u_{TR} are applied simultaneously. The resulting waves propagate back through the medium and interfere constructively at the position of the original source.

In the last few years, many time reversal experiments were performed and different applications presented. In 1995, Derode et al. [8] carried out the first surprising experimental demonstration of the reversibility of a multiple scattered acoustic wave. Their setup is immersed in a water tank and includes an acoustic source, a scattering medium comprised of 2000 randomly positioned steel rods and a time reversal mirror (TRM). The TRM consists of an array of receiver and transmitter transducers connected to a device to store signals. In the first step, a very short signal is excited at the point source and propagates through the scattering media. The transmitted waves are recorded at the TRM, using the transducers as receivers. Due to the multiple scattering, these signals are much longer than the initial pulse at the source. In the next step, the recorded displacement histories are reversed in time

and retransmitted through the medium by the same transducer array operating in the transmission mode. The result is a highly compressed signal with respect to time and space at the position of the initial source.

Further applications of the time reversal method, such as underwater acoustics, medical imaging and pulse-echo detection are described in Refs. [15] and [16]. In the next section, a numerical experiment is executed to demonstrate the applicability of the time reversal method to elastic wave phenomena in solids.

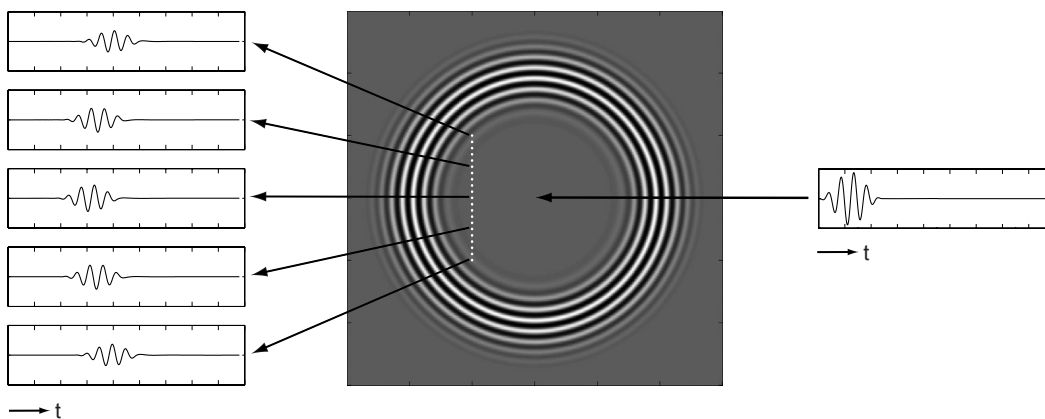### 3.1.3 Numerical time reversal experiment

In this example, flexural waves are excited in the center of an aluminum plate (material parameters according to Table A.2 in Appendix A.1). It is described using Mindlin's theory [36], which includes the influence of rotatory inertia and shear. This higher-order theory must be applied because of the small wavelengths corresponding to the applied frequency range. The plate is lying in the x, y-plane and the displacement field is described by the transversal displacement w and two rotation angles ψ_x and ψ_y. It is assumed that the in-plane displacements are proportional to the plate thickness coordinate z with constant slopes ψ_x and ψ_y, and that the out-of-plane displacement w remains independent of z. The three equations of motion (principle of linear momentum in z direction and principles of angular momentum in x and y directions) are discretized using second-order central differences (see Chapter 2.2). This yields three explicit equations for w, ψ_x, and ψ_y at the new time step $n + 1$. Although the elimination of the rotation angles would reduce the system of equations to one equation only, this step is not performed here. The reason is that the resulting equation would contain the fourth derivative in time and mixed derivatives with respect to time and space, which cannot be implemented with the finite-difference method.

The displacement w in the center of an aluminum plate (size $0.3 \, \text{m}$ by $0.3 \, \text{m}$, plate thickness $h = 0.002 \, \text{m}$) is excited at $200 \, \text{kHz}$. The boundaries of the plate are implemented as being stress-free. 600 cells are used in both directions. Snapshots of the transversal displacements w are shown in Fig. 3.1 at three different times, $20 \, \mu\text{s}$ (a), $40 \, \mu\text{s}$ (b), and $60 \, \mu\text{s}$ (c) after the initiation of the excitation.
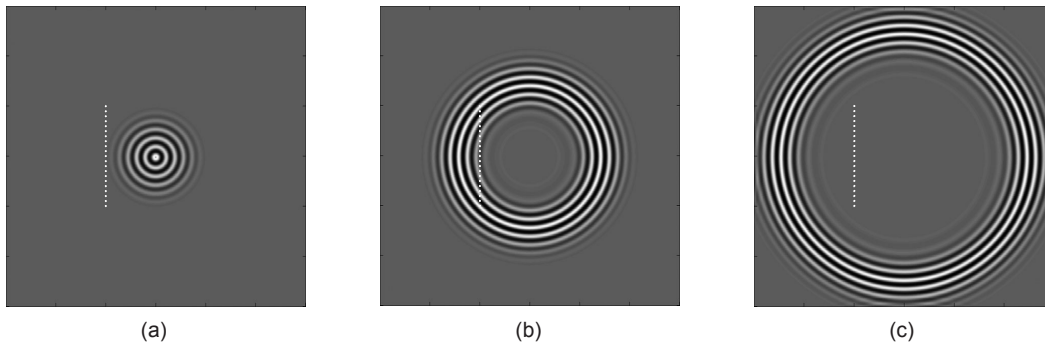
Figure 3.1: Out-of-plane displacements of a plate, 20 μs (a), 40 μs (b), and 60 μs (c), after the initiation of the excitation. The square aluminum plate (data see Table A.2 in Appendix A.1) is excited transversely in the center of the plate at 200 kHz. The white dots mark the measurement positions.

During the simulation, the transversal displacement w and the two rotation angles ψ_x and ψ_y are recorded as a function of time at 21 points. These measurement positions are marked in Fig. 3.1 and Fig. 3.2 as white dots. They are distributed in a parallel manner to one side of the plate with a spacing of 5 mm between each other. The principle of this first step is illustrated in Fig. 3.2. The measurements and the excitation in the center of the plate are started at the same time. The differences among the arrival times are clearly visible in the signals at the left, which show the recorded time signals at five different positions.


Figure 3.2: Principle of the first step of a time reversal experiment. During the excitation of the structure (right signal), the displacements are recorded at different positions (white dots) as a function of time (left signals).

In the next step, the measured signals are reversed in time. Then, the same points that were used for the recording are excited with the displacement histories in a time reverse order using an identical simulation model. To obtain the correct wave field, all components of the displacement vectors at the measuring locations must be retransmitted. The reason is that the implemented finite-difference scheme is based on all three displacement components. Therefore, the transversal displacement w and the two rotation angles ψ_x and ψ_y must be recorded and excited in this example. Another important point is that all displacements must be excited simultaneously with the appropriate time delays at the corresponding positions. This step is visualized in Fig. 3.3, where the time reversed recorded signals are shown on the left. Comparing these signals with the measured histories of Fig. 3.2 (left), the principle of last-in first-out becomes obvious. The signals that arrived last during the simulation (in this case, the signals at the top and at the bottom, which correspond to the recording positions furthest away from the source) are played back first, while the fastest signal (middle) is retransmitted last.
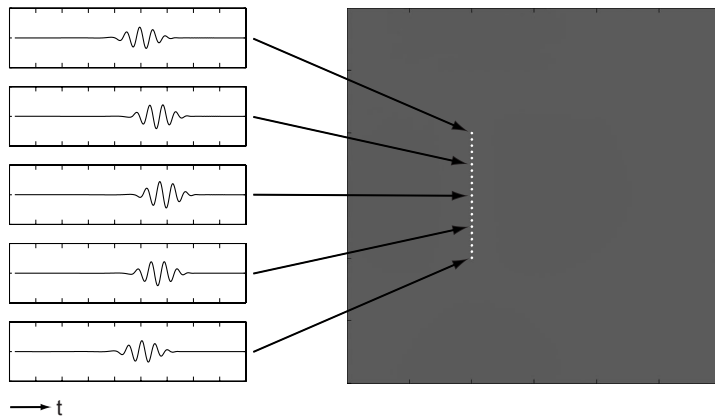
Figure 3.3: In the second step, the recorded signals are time reversed and retransmitted. Therefore, the structure is excited simultaneously at all the measurement points, with the corresponding signals and appropriate time delays.

During the simulation of the time reversed signals, each measurement point acts as a point source with the corresponding excitation signal. The waves propagate in circular motion from the points and start interfering with each other. In Fig. 3.4 the resulting wave fields are plotted for three different times, 55 μs (a), 75 μs (b), and 87 μs (c) after the playback initiation. The absolute time values are irrelevant and depend only on the used time origin, which is given by the duration T of the recording sequence.
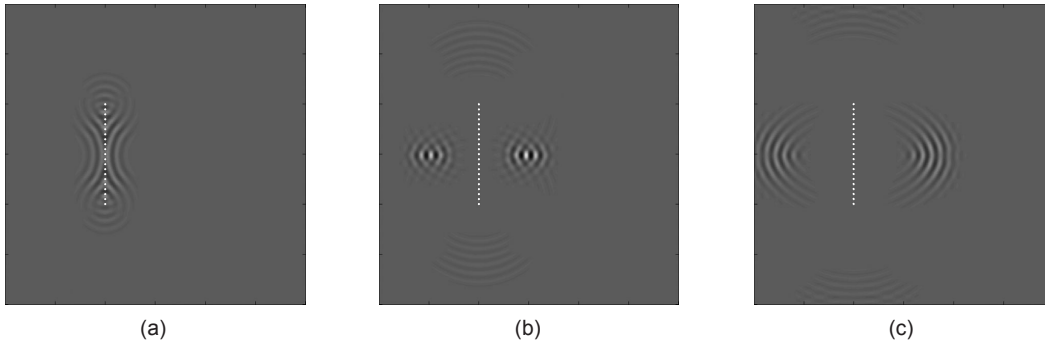
Figure 3.4: Out-of-plane displacements of an aluminum plate (data see Table A.2 in Appendix A.1), 55 µs (a), 75 µs (b), and 87 µs (c), after the initiation of the play back. The recording positions (white dots) are excited with the time reversed measured signals. The three snapshots show the wave fields before (a), after (c), and at the time (b) with the maximum interference.

If the relation between the grayscale values and the amplitudes is kept constant, one can observe the displacements during the simulation to find the time with the maximum interference, which corresponds to the brightest value in the current representation. Once the time with the maximum amplitude is determined, the displacement field at this time is evaluated in order to find the position of the maximum. The plot in the center of Fig. 3.4 corresponds to the time with the maximum interference.

Fig. 3.5 shows a three-dimensional zoom of the center area of the plate at the time with maximum amplitude. The position with the maximum displacement is found by analyzing Fig. 3.5 and has the coordinates 0.15 m and 0.15 m. This corresponds to the center of the plate, where the original pulse was initiated. The amplitude increase at the maximum interference time can be clearly distinguished from the amplitude field at other times.

The numerical example performed confirmed that the time reversal method can also be applied to wave propagation experiments, at least in simulations. As long as the displacements and the rotation angles are recorded and retransmitted at some positions, the origin of a wave field (in this case the point source in the center of the plate) can be determined, even if it is far away. This is an important finding for the application of the time reversal method for detecting defects which is explained in the next section and in [28] by the author.
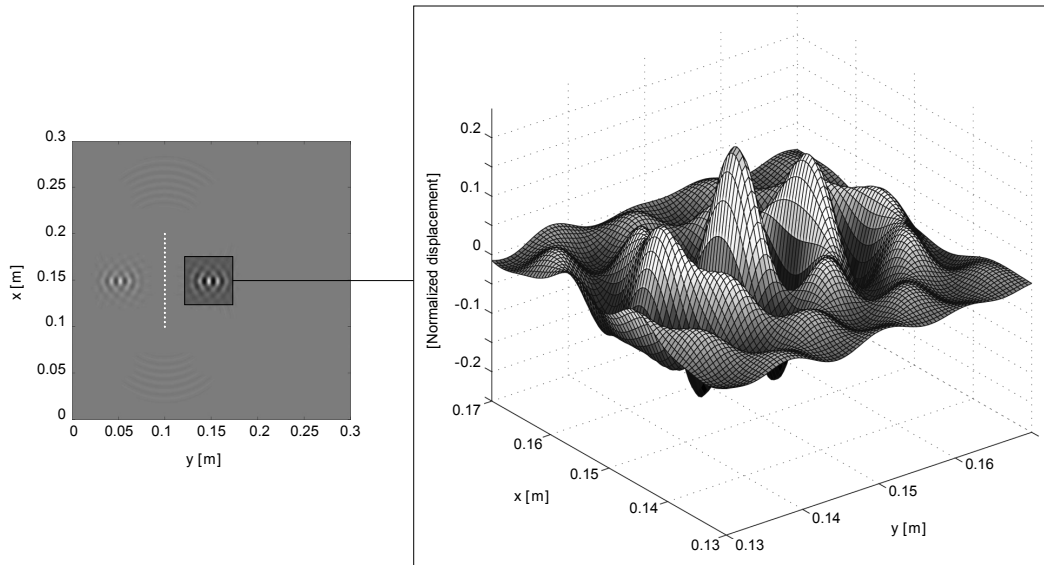
Figure 3.5: Three-dimensional zoom of the center area of the plate (darker region on the left) at the time where the interference of the played back signals is maximal. The amplitude is normalized with respect to the excitation signal used in the first step of the time reverse experiment.

## 3.2 Detection of defects using the time reversal method

The experiments of Derode et al. [8] with steel rods in water, and the numerical example of the plate described in the previous chapter show that the time reversal method can be used to detect the origin of a recorded wave field. In both cases, the waves are generated by a point source and recorded at different locations. Then, the time reversed signals are retransmitted and interfere to the maximum extent at the position of the source. Instead of using the method to determine the original source, it can also be applied to a defective structure in order to determine the presence of a defect and its exact position. This idea was developed and implemented by the author who named it *time reverse numerical simulation (TRNS) method*. This new approach is explained below.

Imagine a guided wave that propagates along a structure and interacts with a present defect. The result is a scattered field which contains a part of the energy of the initial waves. The scattered waves are then recorded at certain measuring positions. This step is outlined in Fig. 3.6 for a tube with an axial notch used as an example. The axisymmetric waves initiated at the left end of the tube interact with

the notch, which generates the scattered field as indicated. These reflected waves are recorded at the measurement points distributed equally around the circumference at the outer surface at the left end of the tube.

Even though the waves are excited at the beginning of the tube, the notch can be viewed as the origin of the scattered field. The defect acts as a source where the scattered waves are generated during the interaction with the initial wave pulse. The fact that the length of the notch in Fig. 3.6 is in the range of the wavelength of the excited waves is only coincidence.
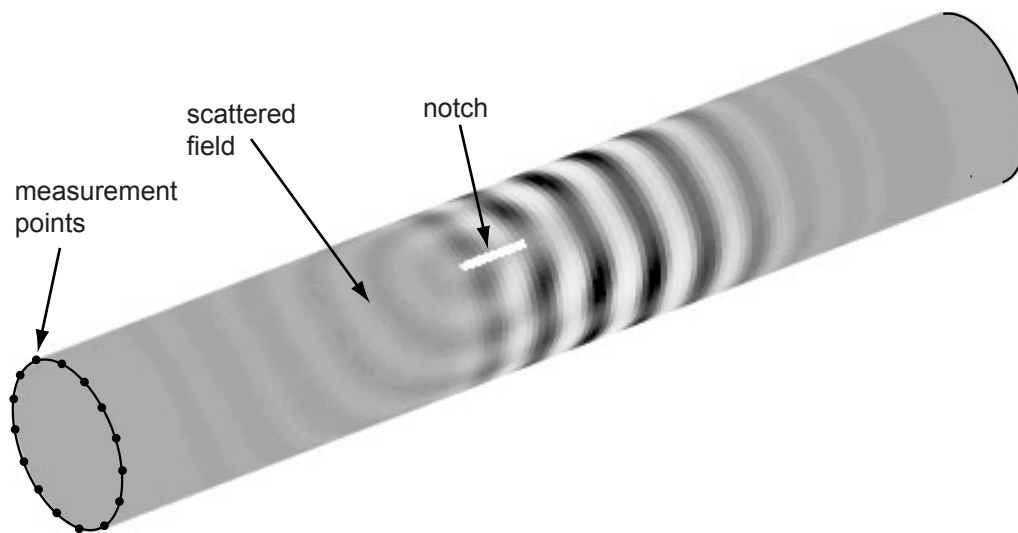

Figure 3.6: Diagram of the recording of the scattered field from a notch at several points distributed equally around the circumference at the outer surface of the tube at the left end. The length of the notch is only by coincidence similar to the wavelength.

According to the previous plate example, the time reversed displacement measurements are used to determine their origin. If the recorded displacement histories are reversed in time and used as excitation signals at the appropriate measuring positions, the waves travel back through the structure and interfere with each other.

In order to obtain the correct location of the maximum amplitude, the structure used for playing back the time reversed signals must be identical with respect to material parameters, boundary conditions, and geometry, and the measuring and retransmission positions must be the same.

The maximum amplitude which results from the constructive interference is obtained at the position of the source, which is exactly the beginning of the notch. Fig. 3.7 shows a diagram of the played back waves at the time with maximum interference. The position of the notch is indicated by the dashed rectangle.

As noted previously, the time reversal method only works properly, if all displacement components are recorded at the measuring positions. In the case of cylindrical structures, these are the radial, tangential, and axial displacements u_r, u_φ, and u_z. As shown with different simulations, it is sufficient to record the three displacements only on the outer surface of the structures, as long as the wavelength is large compared to the thickness of the tube. The reason is that for this frequency range, the wave propagation directions are mainly axial and circumferential.
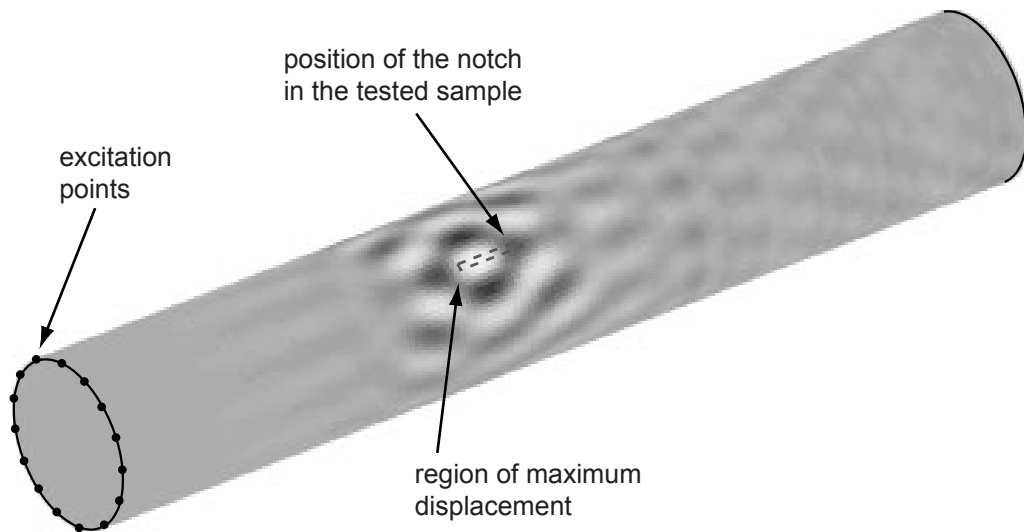
Figure 3.7: Diagram of the played back waves at the time with the maximum interference. All three displacement histories are time reversed and played back in the corresponding locations on the outer surface of the tube. The highest amplitude occurs at the origin of the scattered field which is the beginning of the defect. The position where the notch was located during the first step is indicated by the dashed rectangle.

The recording of the three displacement components in the first step can be done experimentally, using a special laser interferometer which is described in Chapter 4.1. However, for the playback part, imposing precise displacements in three directions at the measuring positions of the structure is difficult in an experiment, especially when dealing with small samples.

Another challenge is the detection of the amplitude increase due to the interference within the structure. If the playback is done experimentally, the tube must be scanned in order to find the maximum amplitude. This procedure is performed by Ing et al. [26] who use a laser interferometer to find the origin of time reversed lamb waves in thin plates. Since the main goal of this thesis is the development of a new method for the fast NDT of large structures, the aim is to eliminate such

steps. For this reason, and also to avoid the complex excitation of the displacements and the scanning of the sample, the playback part is replaced by a numerical simulation. This enables also the visualization of the position of the maximum amplitude. In this case, imposing the time reversed displacement histories is easy. As long as the simulated structure shares the same geometrical and material parameters and the same boundary conditions as the sample used in the experiment, the reverse wave propagation can be calculated numerically. To obtain accurate results, the physics of the wave propagation phenomenon must be described appropriately by the simulation. To fulfill this requirement, a three-dimensional code in cylindrical coordinates with a high accuracy must be used. The finite-difference codes described in Chapter 2. meet these demands.

One important characteristic of the time reversal method is that even though no defect is present in the simulated structure used in the playback step, the waves interfere constructively, and the maximum displacement or stress takes place at the position where the defect is located in the sample used for the recording. This is one of the key features of the TRNS method. It means that measured signals obtained in an experiment performed on a defective structure can be time reversed and used as input signals in a notch-free simulation to determine the position of a defect within a large structure. A summary of the major steps of the TRNS method is provided below:

- In a physical experiment, guided waves are excited in a defective tube. Compared to other NDT methods using guided waves, the initiation of the waves is not a crucial step in this approach. It is not necessary to excite one specific mode. Basically, any method that generates scattered waves at the defect is applicable.

- The amplitudes of the scattered waves that are generated at the defect are measured as a function of time at different positions. All three displacement components must be recorded, which is done by using a three-dimensional laser interferometer. It is sufficient to measure points on the surface of the tube only.

- A structure with the same geometrical and material parameters is implemented in the simulation code. This structure is free of defects and must have the same boundary conditions as the sample used in the experiment.

- The recorded signals are time reversed and used as excitation signals in the simulation. Therefore, the points in the simulated structure that correspond

to the measuring positions are driven simultaneously in all three directions, with the corresponding signals and the appropriate time delays.

- The waves start to propagate back through the structure and begin to interfere with each other. During the playback simulation the displacement amplitudes are observed in order to determine the time and position of the maximum interference.

- From this location in the simulated structure, the axial and circumferential coordinates of the defect within the defective tube are calculated by using the corresponding discretization parameters. Since the time signals are not analyzed directly, it is neither necessary to determine any time differences nor to identify the scattered wave modes or their group velocities.

Until now, the time reversal method was either used for strictly theoretical examples or as a tool for investigations where both steps, recording and retransmitting, are performed experimentally on the same sample. In contrast to the applications found in literature, the TRNS method at hand combines experiments and numerical simulations. The result of this new combination is an efficient and accurate method for the detection of defects in real structures. Since scanning the sample is eliminated by using simulations, the present approach can also be applied to tubes with insulation or limited access. The experiments performed and results achieved are presented and discussed in Chapter 4.

3.3 Verification of the method using simulated data

To validate the TRNS method, the whole procedure is simulated. Accordingly, the first two steps are performed in a simulation as well instead of an experiment. The defect is approximated by a notch implemented into the FDM code as described in Chapter 2.2.4. Then, this simulation of the defective structure is excited, and the scattered field is recorded at the measuring points. The next steps are performed following the standard procedure of the TRNS method.

This verification allows the user to check the concept and applicability of the TRNS method to large structures and to test the accuracy of the introduced approach. Thanks to the simulation of all steps, the following uncertainties and errors encountered during the experiment can be eliminated:

- The material parameters and the geometry of the defective structure used for the generation of the scattered field are known in detail due to their exact definition in the simulation code. This prior knowledge eliminates the determination and measurement of these values in the sample to be tested.

- The recording positions are identical to the retransmission points, and the three displacement directions match the radial, tangential, and axial components. Errors resulting from the three-dimensional laser interferometer and positioning deviations are excluded.

- The excitation of purely axisymmetric wave modes is possible in the simulation. Although this is not necessary, it simplifies the interpretation of the recorded time histories. Another advantage is that the implemented structure is homogeneous, geometrically axisymmetric, completely straight and of even wall thickness. This assures that the structures used to record and play back the waves are identical except for the notch.

- Since no measuring equipment, excitation transducers, interferometer and optical devices are used for the verification, the recordings are free of noise or offsets, and the piezo element has no influence.

An aluminum tube (mass density $\rho = 2700 \, \text{kg/m}^3$, Young's modulus $E = 6.9 \cdot 10^{10} \, \text{N/m}^2$, Poisson's ratio $\nu = 0.34$) with a wall thickness of $h = 0.002 \, \text{m}$, with a radius of midplane $R = 0.015 \, \text{m}$, and a length of $l = 2 \, \text{m}$, is used for the validation. A part-through circumferential notch is implemented at a distance of $0.8 \, \text{m}$ from the excitation location at the left end. The notch starts at the outside of the structure, is $1 \, \text{mm}$ deep and $1 \, \text{mm}$ wide. The circumferential extent is $9.5 \, \text{mm}$ which corresponds to approximately $34°$. 4, 106, and 2000 cells are used in radial, circumferential, and axial directions, respectively. The left end of the tube is excited axisymmetrically in axial direction across the wall thickness with 10 cycles of a sine wave at a frequency of $200 \, \text{kHz}$. According to the dispersion diagram in Fig. 1.1, two wave modes [L(0,1) and L(0,2)] are expected for the applied axisymmetric excitation at the chosen frequency. The driving function is multiplied by a Hanning window before being applied. This is equivalent to the experiment described in Chapter 4.5.1.

Four snapshots of the axial displacement at different times are shown in Fig. 3.8. Since the excitation is above the first cutoff frequency, the L(0,2) mode exists and is clearly visible. Of course the L(0,1) mode also occurs but is barely visible in this representation of the axial displacement. This is due to the ratio
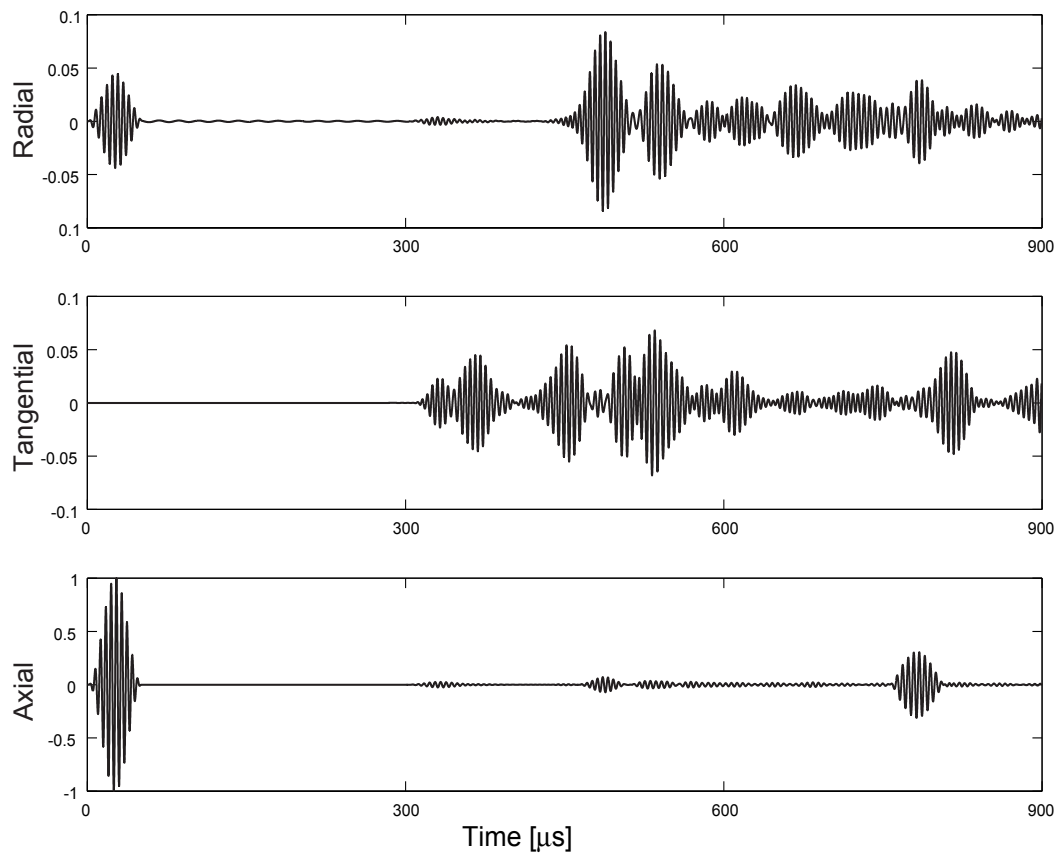
between the radial and axial displacements of the two modes. For the geometry and frequency in this example, the axial displacements of L(0,1) at the outer surface are much smaller than those of L(0,2).
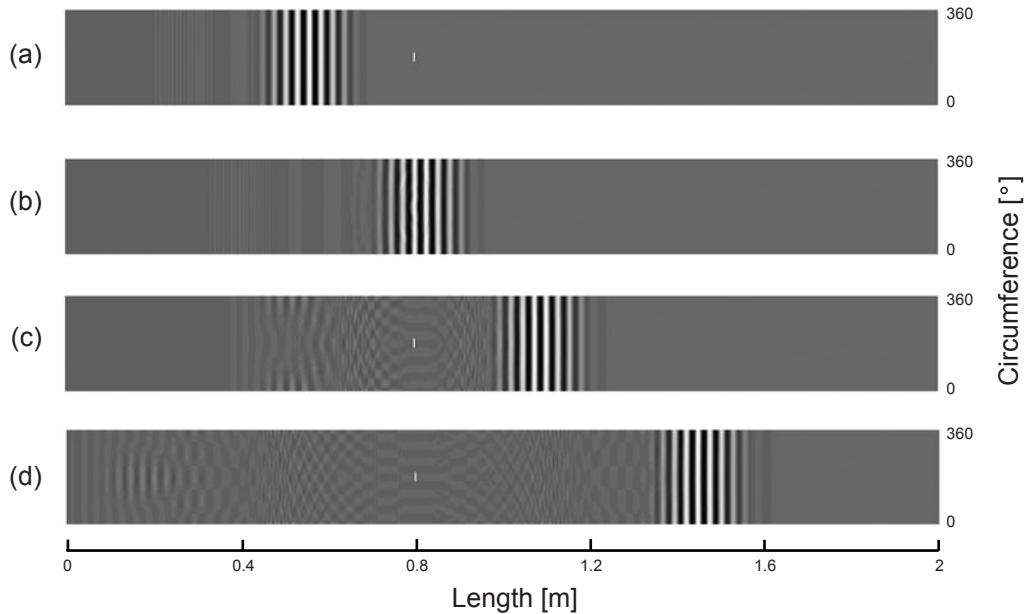
Figure 3.8: Interaction with a circumferential part-through notch that is 0.8 m away from the left end of an aluminum tube (see Table A.2 in Appendix A.1) of 2 m length. The axial displacements at the outer surface are shown at 130 µs (a), 180 µs (b), 231 µs (c), and 300 µs (d) after the axial excitation at 200 kHz at the left end. The tube is plotted in a developed view, with the axial length on the horizontal, and the circumference on the vertical axis. The circumference is enlarged for better visualization.

To display the entire tube surface, a developed view is chosen with the axial and circumferential extent on the horizontal and vertical axis, respectively. For better visualization, the circumference, which is about 0.1 m for the present tube, is enlarged relative to the length of 2 m. The amplitudes are represented as different gray values with a constant range for all four snapshots.

During the simulation, radial, tangential, and axial displacements are recorded in 106 points distributed equally around the circumference on the outer surface at the left end. Fig. 3.9 shows the recorded time histories in one measuring location. The amplitudes are normalized with respect to the maximum excitation in axial direction. The amplitude ranges of the three displacements are different.

Figure 3.9: Recorded time histories of the radial, tangential, and axial displacements in one of the measuring points at the outer surface at the left front side of the tube. The amplitudes are normalized with respect to the maximum applied excitation in axial direction.

The time histories are recorded for a duration of $900\,\mu s$. The wave packet in the axial displacement at around $800\,\mu s$ corresponds to the first reflection of the L(0,2) mode from the right end. Between the excitation and the first reflection, many different wave packets exist, and the time signals are difficult to interpret.

Fig. 3.10 shows the group velocity dispersion curves for the simulated tube for circumferential orders $n = 0,1,...,10$ and mode numbers $m = 0,1,...,10$. Since L(0,2) is the fastest mode in the selected frequency range, all waves between the excitation and the first reflection from the end must correspond to reflections from the defect and therefore have the same propagation direction.
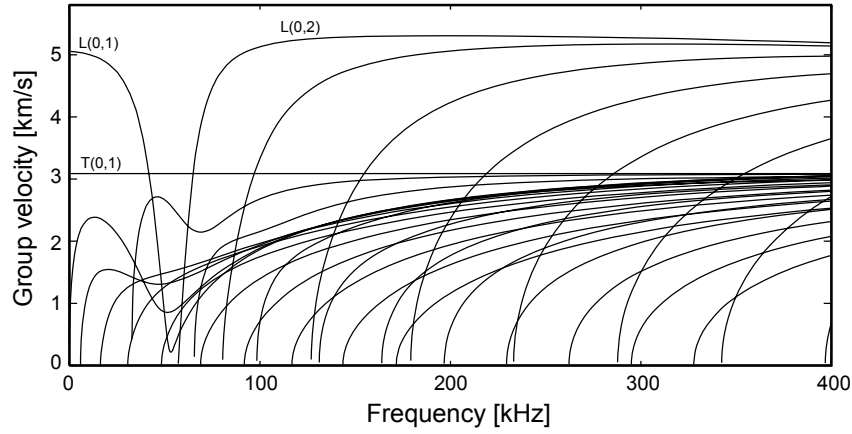
Figure 3.10: Group velocity dispersion curves for the tested aluminum tube (data see Table A.2 in Appendix A.1) for longitudinal L(0,*m*), torsional T(0,*m*), and flexural F(*n*,*m*) modes. The curves for mode numbers *m=0,1,...,10* and circumferential order *n=0,1,...,10* are plotted. The unlabeled lines correspond to flexural modes.

Since the excitation is perfectly axisymmetric, the first non-axisymmetric signals must be reflections from the notch. They are most visible in the tangential displacement, which is zero until around $300\,\mu s$. After this first reflection from the notch, many more wave packets arrive at the measurement positions. Since the scattered field is generated at the notch, which is a *quasi point source*, it changes from position to position and cannot be described by plane waves near the defect. Even far away from the notch, only the first wave packets in the time histories can be assigned to specific modes. The reflections at later times can no longer be classified since the waves modes are not separated. Therefore, the determination of their group velocities from dispersion diagrams becomes very ambiguous.

As described in Chapter 2.2, the stress components are also calculated explicitly in the present FDM code. The disadvantage of this approach in terms of memory requirements and computational time turns out to be an advantage for the TRNS method. The interaction of the excited waves with a defect are most visible in the stress components. As examples, the six stress components are plotted in Fig. 3.11 and Fig. 3.12 at four different times during the generation step of the scattered field. The same times are chosen here that were used for the snapshots of the axial displacements in Fig. 3.8. The notch is plotted as a white line, and the amplitudes are normalized with respect to the highest stress that occurs during the simulation. For the current excitation in axial direction, these are the axial normal stresses σ_{zz}.
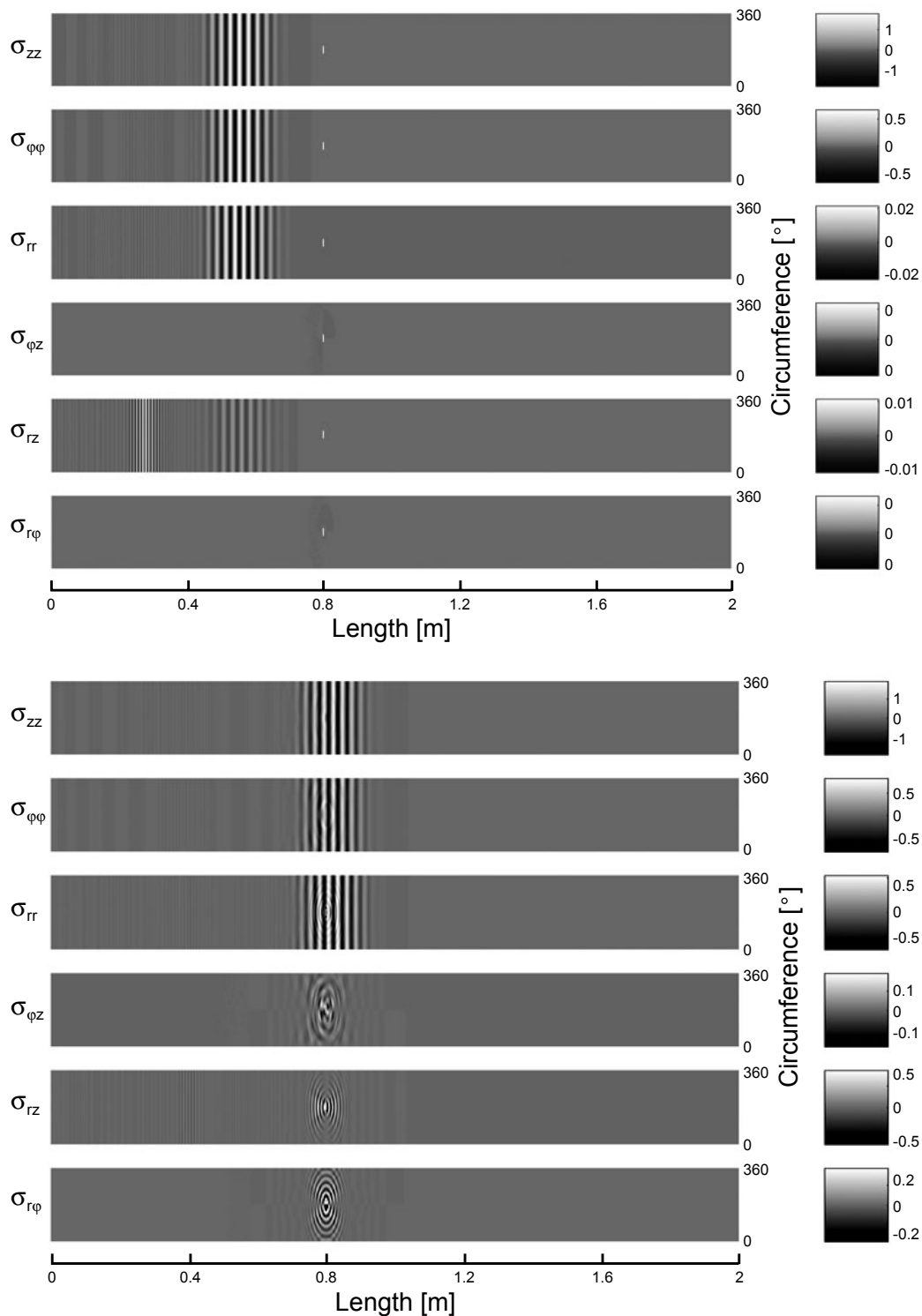
Figure 3.11: Snapshots of the stress components below the outer surface are shown 130 μs (top) and 180 μs (bottom) after the axial excitation at 200 kHz at the left end.
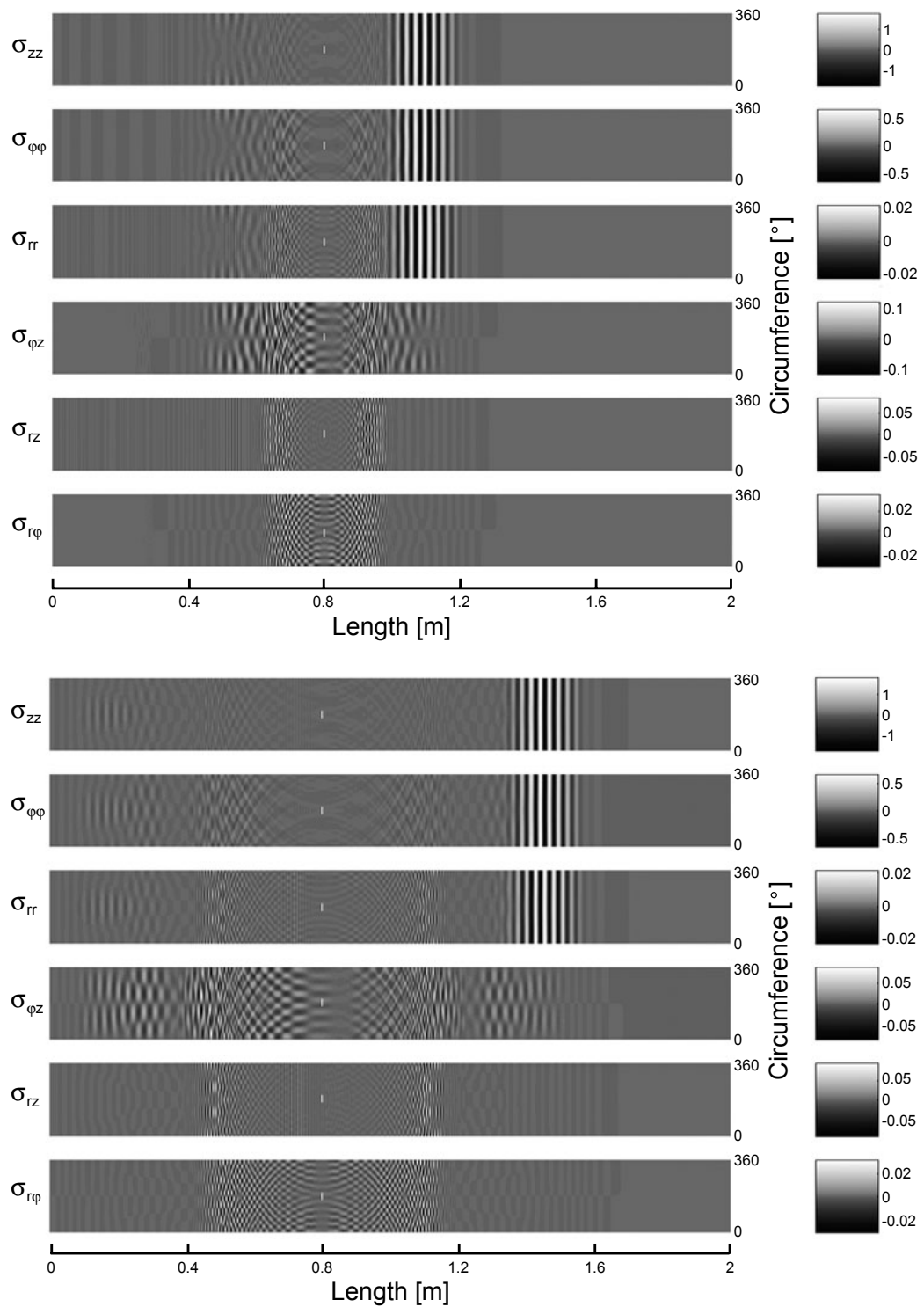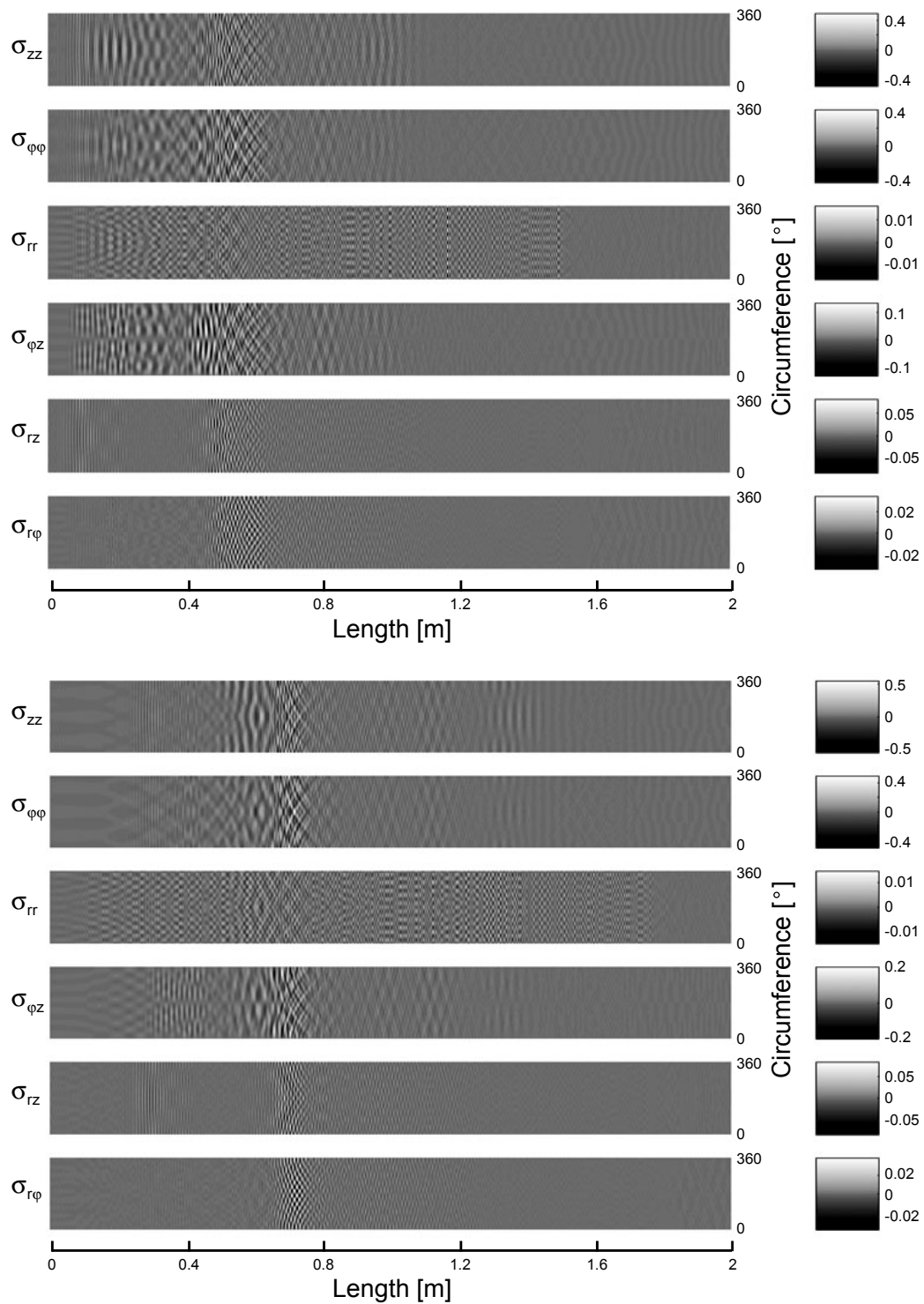
Figure 3.12: Snapshots of the stress components below the outer surface are shown 231 µs (top) and 300 µs (bottom) after the axial excitation at 200 kHz at the left end.

The scattered field is much more visible in the stress components than in the axial displacements of Fig. 3.8. Even the L(0,1) mode is apparent in the shear stress component σ_{rz} in Fig. 3.11 (top). The reason for this is that the range of this component is small enough before the L(0,2) mode reaches the notch. At 180 μs after the excitation (Fig. 3.11 bottom), the L(0,2) mode interacts with the notch. The beginning of the scattered field at the defect is most visible in the shear components, which are very small or zero before the interaction with the notch for the chosen axisymmetric excitation. After the L(0,2) packet has crossed the notch region, a part of the scattered field propagates back towards the left end. The other part travels in the same direction as the initial waves (Fig. 3.12 top) but at a lower speed than the original L(0,2) mode. The excited L(0,2) mode is always faster than all other wave modes generated at the notch, which is visible in the dispersion diagram in Fig. 3.10. Since the scattered field consists of a superposition of many wave modes, it changes with time and space. The different group velocities become apparent by comparing the snapshots of Fig. 3.12, top and bottom.

In the next step, the notch is removed from the previously used structure, and another simulation is performed. For excitation, the time reversed signals recorded at the 106 positions at the left end, are applied simultaneously at the corresponding points. In the example at hand, the first 750 μs of the displacement histories are played back, excluding the reflections from the right end. As a result, the scattered waves travel back along the tube. Snapshots taken at four different times during the playback simulations are depicted in Fig. 3.13 and Fig. 3.14. Again, the absolute times are irrelevant and depend only on the duration of the recording and the used time origin. At the top and bottom of Fig. 3.13, the snapshots are shown at 456 μs and 531 μs. The various wave packets and their different group velocities can be seen. The snapshot at the top of Fig. 3.14 depicts the stress components at the time when the maximum amplitudes occur. The wave field is focused on one location, which corresponds exactly to the position of the defect at 0.8 m from the left end. The position is clearly visible in all stress components. At later times, the waves start to separate again (see Fig. 3.14, bottom). The amplitudes of the stress components are normalized with respect to the maximum value that occurs during the TRNS. This is the axial normal stress σ_{zz} at 573 μs. The comparison of the stress amplitudes during the playback simulation shows an intense increase of up to 100% when the waves reach the location of the defect. This enables an accurate determination of the axial and circumferential position of the notch.

Figure 3.13: Snapshots of the stress components 456 µs (top) and 531 µs (bottom) after the start of the playback of the recorded displacement histories.
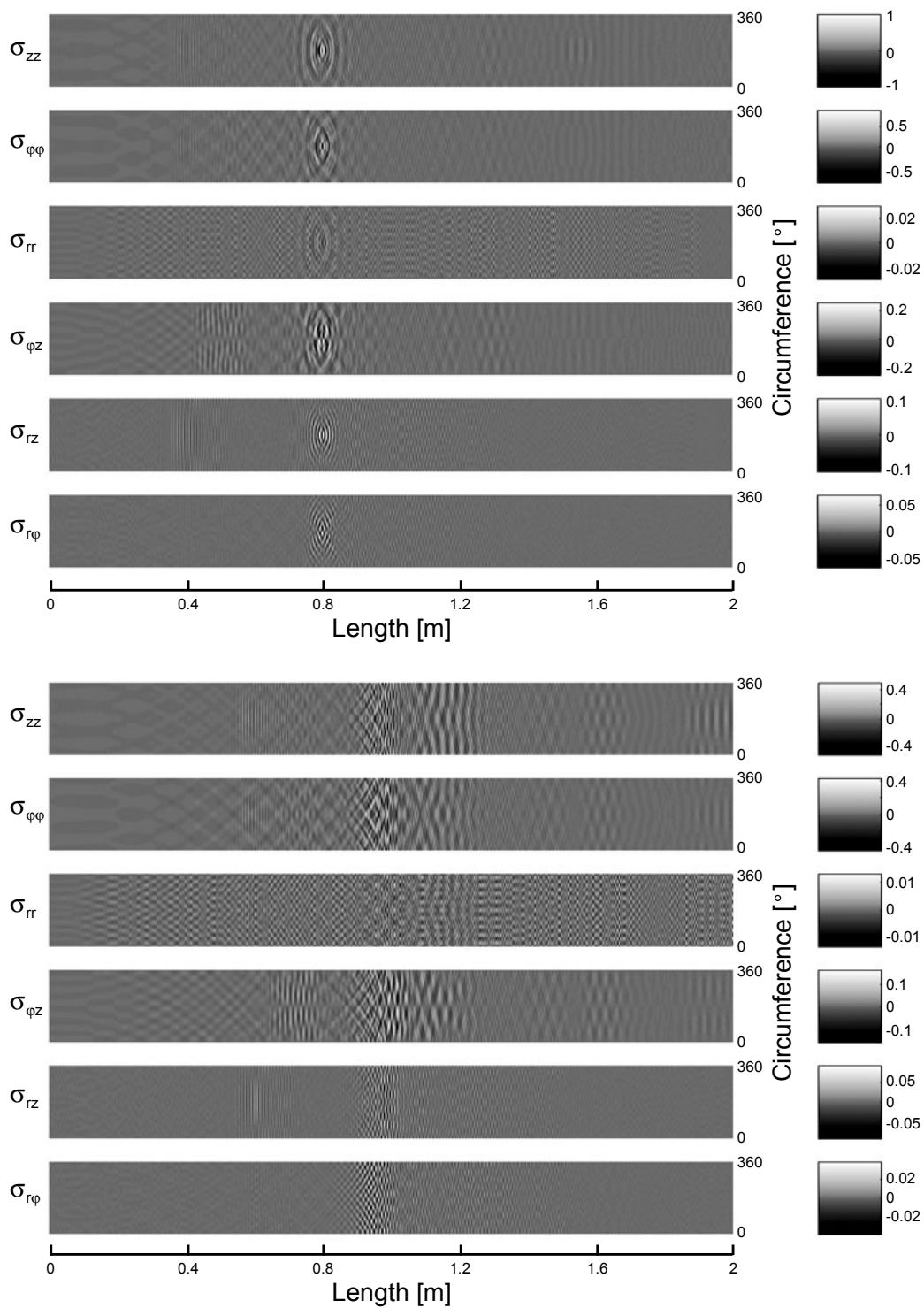
Figure 3.14: Snapshots of the stress components 573 μs (top) and 648 μs (bottom) after the start of the playback. The top picture shows the time when the maximum amplitude occurs. The position of the notch is clearly visible and matches the exact location.

Since the scattered field is generated in a simulation, the recorded time signals and the TRNS method in its entirety are of high quality. Accordingly, the position of the defect can also be detected by observing the displacements. Fig. 3.15 (top) shows the developed view of the structure with the defect that was used for the generation of the scattered field. The bottom picture displays the axial displacement field at the time with maximum interference. The position of the notch is clearly visible and matches the exact location.
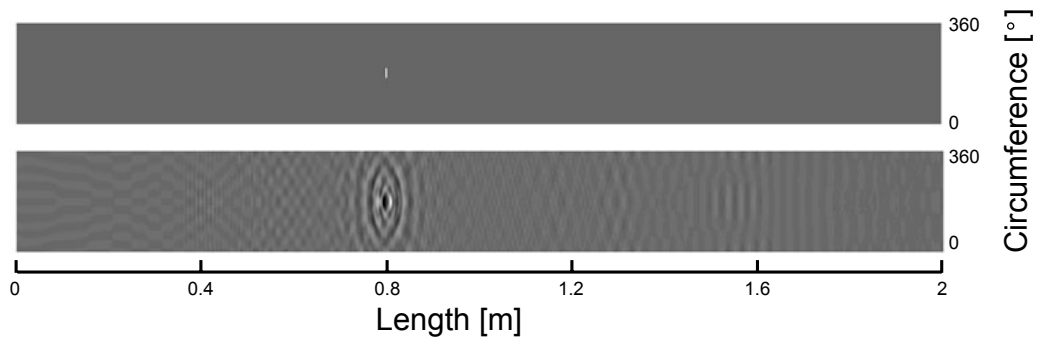
Figure 3.15: Developed view of the unexcited structure with the notch (top) and the axial displacement field at the time of maximum interference (bottom). The waves are focused on a location which matches the exact position of the notch in axial as well as circumferential direction.

However, in real experiments, the positions can be determined from the displacement signals only with difficulty, which is why the stress components are observed there.

It is important to play back only direct reflections from the defect. If reflections of the transmitted field from the end of the structure are retransmitted as well, the defect cannot be located correctly. Assume, for this example, that the displacements are recorded for a duration of $2000\,\mu s$. These histories also include the first reflection of the L(0,2) mode from the right end (after $800\,\mu s$) and the fastest transmitted wave packets which were generated at the notch and reflected at the right end. Since these reflections travel along the whole structure twice before reaching the recording positions, they arrive much later. In the playback part, this is compensated for by exciting them first. The played back reflected waves from the end are also reflected at the right end in the time reverse simulation and travel back towards the recording or excitation positions. On their way back, they cross the direct reflections from the defect that are retransmitted later at the left end. Even if the time delays are appropriate, the two fields do not interfere constructively at the

position of the defect. This is due to the fact that the reflections from the end of the structure pass the defect twice before being recorded. When played back, they cannot interact with the defect on their first path because no defect is present in the sample used for the time reversed simulation. This changes the path of the waves so that they can no longer interfere correctly. Therefore, it is important to only play back signals that interacted just once with the defect. For this example, this means that only the first $750\,\mu\text{s}$ of the recorded displacements are time reversed and retransmitted.

3.4 Conclusions

Since elastic wave propagation is described by time-reversal-invariant equations, wave phenomena can be reversed in time and played back. This is demonstrated for the example of flexural waves in a plate, where the recorded wave field is time reversed and played back. The retransmitted waves interfere and reach a maximum amplitude at the position of their origin, which can be either a source or a notch. This is the key element of the developed time reverse numerical simulation (TRNS) method. Structural waves are generated in a defective sample, and the scattered field that results from the interaction with the defect, is recorded at several positions. Then, these signals are time reversed and used as excitation signals in a numerical simulation of the same structure, but without a defect. The played back waves refocus at the position of the defect as long as all three displacement components are excited simultaneously. It is found that it is sufficient to only record the displacements on the surface of the structure. The advantage of using a simulation for the playback part is that the position and time of the maximum amplitude can be determined by observing the displacement and stress components during the simulation. Hereby, the time-consuming scanning of the structure, which would require overall access and the removal of any possible insulations, is eliminated. The simulation of a complete experiment allows the verification of the TRNS method and its applicability to the NDT of large structures.

4. EXPERIMENTS AND RESULTS

4.1 Three-dimensional vibrometer

To perform a TRNS from an experiment, it is necessary to know the radial, tangential, and axial displacement histories in the recording points distributed circumferentially and equally on the outer surface of the structure at a fixed axial position. In order to measure the scattered field without disturbing the wave propagation, a non-contact method is chosen. In this thesis, a heterodyne laser interferometer (Polytec OFV 303) is used, a device which is well-established at the Center of Mechanics. Since the vibrometer measures only the displacement component parallel to the beam, three measurements must be taken from different directions to determine the complete displacement vector in one point. To avoid time-consuming repositioning of the laser head and to improve the repeatability and the focus on a single point, the laser beam is split into three separate rays. This is achieved by using the optical setup shown in Fig. 4.1.
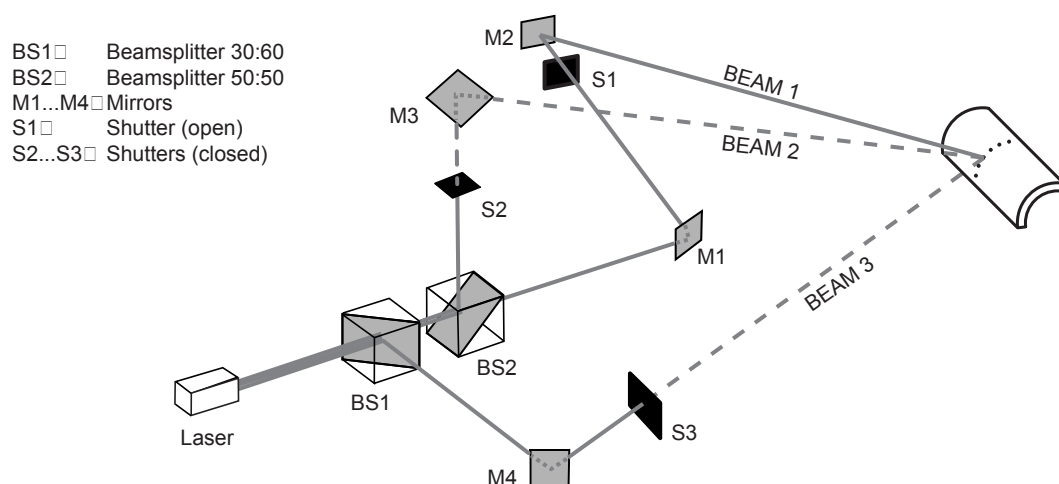

Figure 4.1: Diagram of the optical setup of the three-dimensional vibrometer.

The laser beam is first divided into two rays by passing the beamsplitter BS1 (broadband hybrid beamsplitter cube, 30:60, 440-680 nm, Coherent). The ratio of reflected and transmitted intensity is 30:60. The transmitted ray passes another beamsplitter BS2 (laser non-polarizing cube beamsplitter, 50:50, 633 nm, Coherent), which splits it into two equal beams. Each of the three beams contains about 30% of the laser energy.

Then, these three beams are guided onto one spot, using the mirrors M2 to M4 (dielectric mirrors, reflectivity > 99%, 632.8 nm, Newport) to adjust the directions. All optical components are chosen to match the helium-neon (HeNe) laser wavelength of 633 nm. Although the beams reflected back to the laser head contain less than 9% of the initial energy, the displacements can still be measured, provided that very good reflectivity at the sample is guaranteed. This is achieved by gluing retro-reflective tape onto the surface of the sample.

Fig. 4.2 shows a picture of the optical setup used in the experiments. The components are labelled according to the diagram in Fig. 4.1. The ray paths are outlined with white lines (solid line for the patched-through beam and dashed lines for the rays blocked by the shutters).
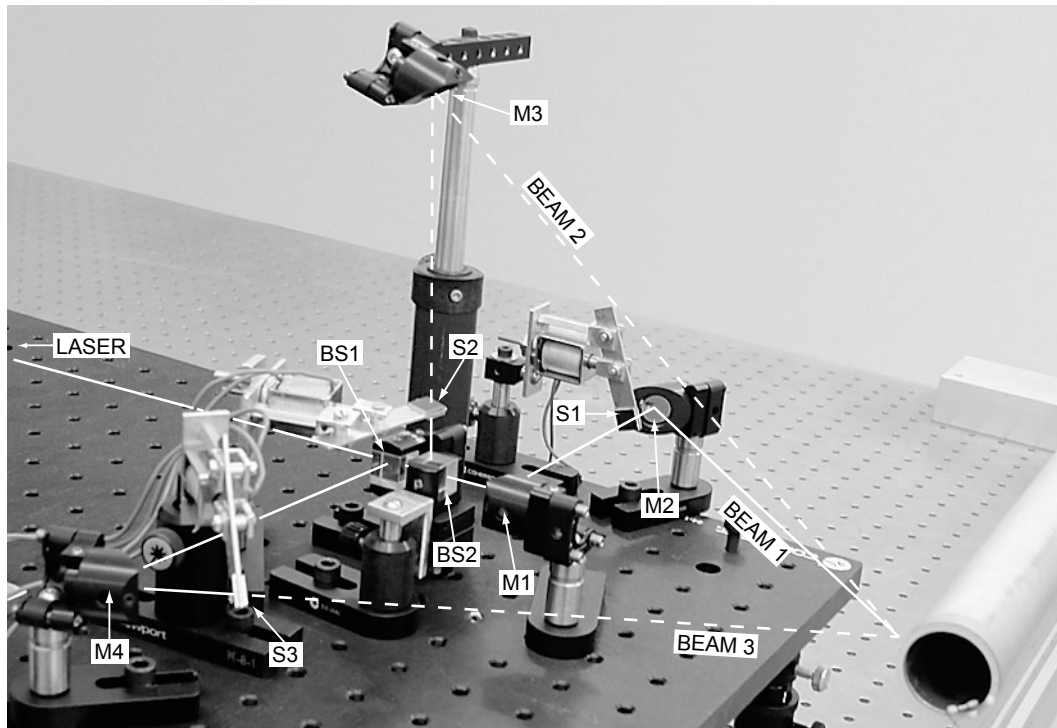
Figure 4.2: Optical setup with the components labelled according to the previous diagram. The three ray paths are outlined with white lines (solid line for the patched-through beam and dashed lines for the rays blocked by the shutters).

The working principle of the vibrometer only allows the measurement of one direction at a time. Therefore, each optical path is equipped with a shutter (S1 to S3), which enables sequential patch-through of the three beams. The shutters (Fig. 4.3 left) are lifting magnets that are driven by the computer via the serial interface using a self-made shutter control (Fig. 4.3 right). This is an important step in the automation of the whole experiment. A circuit diagram and a description of the functionality of the control are provided in Appendix A.4. To minimize reflections from the closed shutters, their ends are coated with dull black anodized aluminum.
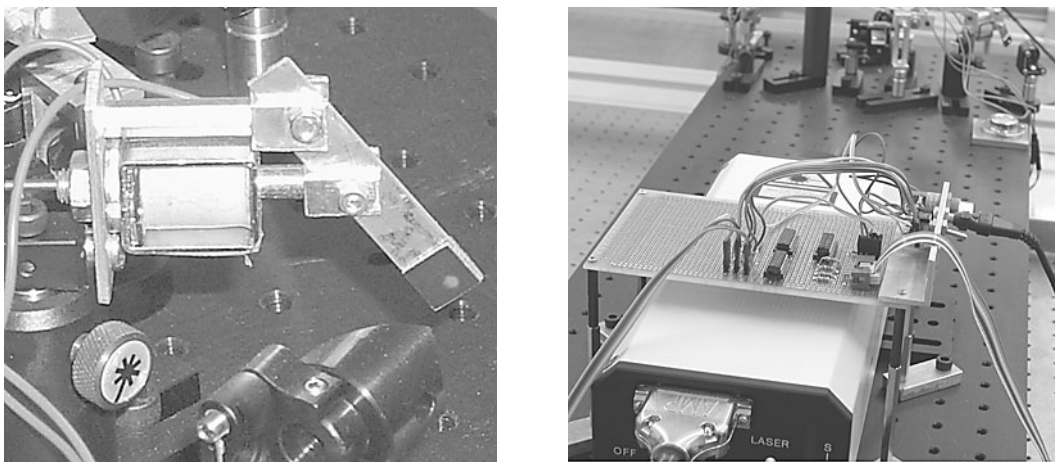
Figure 4.3: Close-up view of a shutter in its closed position (left). The ends are coated with dull black anodized aluminum to minimize reflections of the laser beam. The right picture shows the shutter control mounted above the laser head and the optical setup in the background.

To ensure focussing of all three rays and to simplify the adjustments onto one spot, the optical components must be arranged in such a way that the three beam paths are of equal length. For this reason, another mirror M1 (same characteristics as M2 to M4) is inserted to extend the path of beam 1. In addition to these precautions, an auto-focussing routine is implemented into the measuring procedure to eliminate small focussing deviations between the different positions. Although the laser could be completely refocused automatically after every beam change, much time can be saved by arranging the components in an appropriate way. The exact positioning of the optical components is provided in Appendix A.5.

4.1.1 Determination of the displacement histories

The three measured displacement components u_1, u_2, and u_3, which correspond to the beams 1 to 3, contain the superpositions of the projections of the radial, tangential, and axial displacements onto these directions. It is necessary to distinguish between the displacement components at the measuring position $\tilde{u}_r$, $\tilde{u}_\varphi$, and $\tilde{u}_z$ and the staggered components u_r, u_φ, and u_z which are used in the TRNS. The measured displacements are given as

$$
\begin{aligned}
u_1 &= \tilde{u}_r \cdot cos\alpha - \tilde{u}_z \cdot sin\alpha \\
u_2 &= \tilde{u}_r \cdot cos\gamma + \tilde{u}_\varphi \cdot sin\gamma \\
u_3 &= \tilde{u}_r \cdot cos\beta + \tilde{u}_z \cdot sin\beta
\end{aligned}
\tag{4.1}
$$

where α, β, and γ are the angles between the measuring directions and the coordinate axis according to Fig. 4.4. While beam 1 and beam 3 are positioned in the r, z-plane, ray 2 is an element of the r, φ-plane. The laser head is aligned with the r-axis.
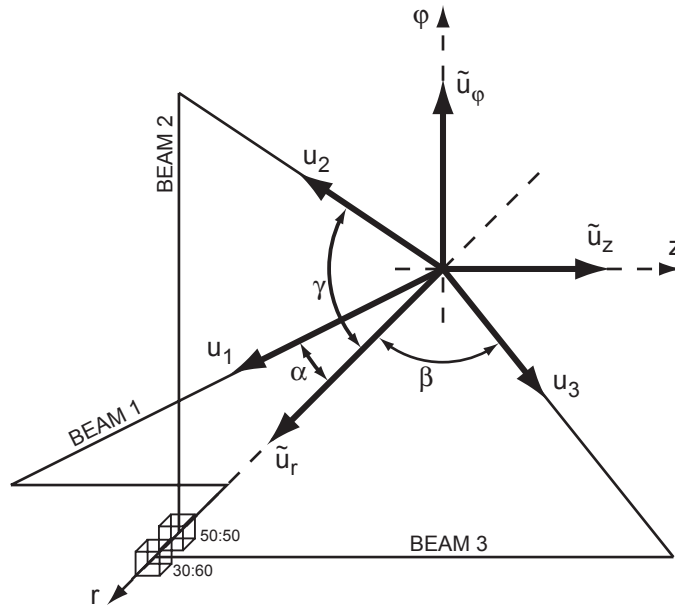
Figure 4.4: The three angles α, β, and γ define the directions of the three measurement beams with respect to the coordinate system used for the tube.

The displacement components in the r, φ, z-system can be calculated from the measured values as

$$\tilde{u}_r = \frac{u_1 \cdot sin\beta + u_3 \cdot sin\alpha}{sin(\alpha + \beta)} \qquad (4.2)$$

$$\tilde{u}_\varphi = \frac{u_2}{sin\gamma} - \frac{u_1 \cdot sin\beta + u_3 \cdot sin\alpha}{tan\gamma \cdot sin(\alpha + \beta)} \qquad (4.3)$$

$$\tilde{u}_z = \frac{u_3 \cdot cos\alpha - u_1 \cdot cos\beta}{sin(\alpha + \beta)} \qquad (4.4)$$

The angles α, β, and γ must be determined from the optical setup used for the experiment. The applied procedure is explained in Appendix A.6.

Due to the staggered grid in the finite-difference code, the time reversed displacement histories must be applied at different locations in the simulation. The grid is deliberately chosen so that the axial and tangential components are positioned on the surface of the structure and the radial displacement is shifted in radial direction by half a cell. The distribution is shown in Fig. 4.5.
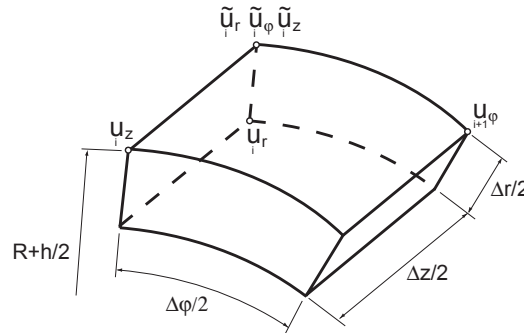
Figure 4.5: Allocation of the measured and simulated displacement components.

As a first approximation and for fine grids and long wavelength, the measured values $\tilde{u}_r$, $\tilde{u}_\varphi$, and $\tilde{u}_z$ can directly be used as u_r, u_φ, and u_z which are shifted by half the spatial step sizes.

However, the radial and tangential components can be approximated more accurately using the following assumptions. Since the measuring positions are distributed around the circumference, the appropriate values for the tangential displacements, which have the same axial and radial coordinates as the measuring positions, can be linearly interpolated from two neighboring points. This works if the grid size $\Delta\varphi$ corresponds to the angular step between the measuring locations.

The radial displacements are calculated by solving the boundary condition Eq. (2.10) (σ_{rr} must vanish on the surface). Therefore, Eq. (2.6) is discretized and solved for the radial displacements, using linear interpolation in radial direction to determine the fictitious values. Neglecting the deviations of the axial displacement in axial direction, yields

$$
u_{r_i} = \left(1 + \frac{\Delta r \cdot \nu}{2(1-\nu)\left(R+\frac{h}{2}\right)} \right) \cdot \tilde{u}_{r_i} + \frac{\Delta r \cdot \nu}{2\Delta\varphi(1-\nu)\left(R+\frac{h}{2}\right)} \cdot \left(u_{\varphi_{i+1}} - u_{\varphi_{i-1}} \right) \quad (4.5)
$$

R, h, Δr, $\Delta\varphi$, and ν denote radius of midplane, wall thickness, radial, and tangential discretization parameters, and Poisson's ratio, respectively. The index i defines the circumferential position.

Good results are obtained with this method. To achieve even better accuracy, additional measurements must be taken at a second circumference, shifted in axial direction by Δz.

4.2 Experimental setup

The applied method for measuring wave propagation phenomena in cylindrical structures experimentally was used at the Center of Mechanics over the years ([10], [22], [56]). In the present case, waves are excited using piezoelectric elements. The displacement amplitudes, which are in the nanometer range, are measured by laser interferometry. For better accuracy, a high resolution phase demodulator based on the idea of Goodbread [19] and described in detail by Dual et al. [11], is used. To dampen vibrations transmitted by the building, the measurements are performed on an optical table (Newport RS4000).
The experiments are computer-controlled using the software LabView (National Instruments). The electronic devices and the computer communicate via the IEEE 488 (GPIB) interface and the serial data interface.

The experimental setup is shown in Fig. 4.6 and consists of the sample mounted in the rotational axis, the three-dimensional vibrometer, the piezoelectric excitation and the electronic devices. While the setup of the test specimen and the excitation are described in Chapter 4.2.1, the other steps of the experiment are explained below:
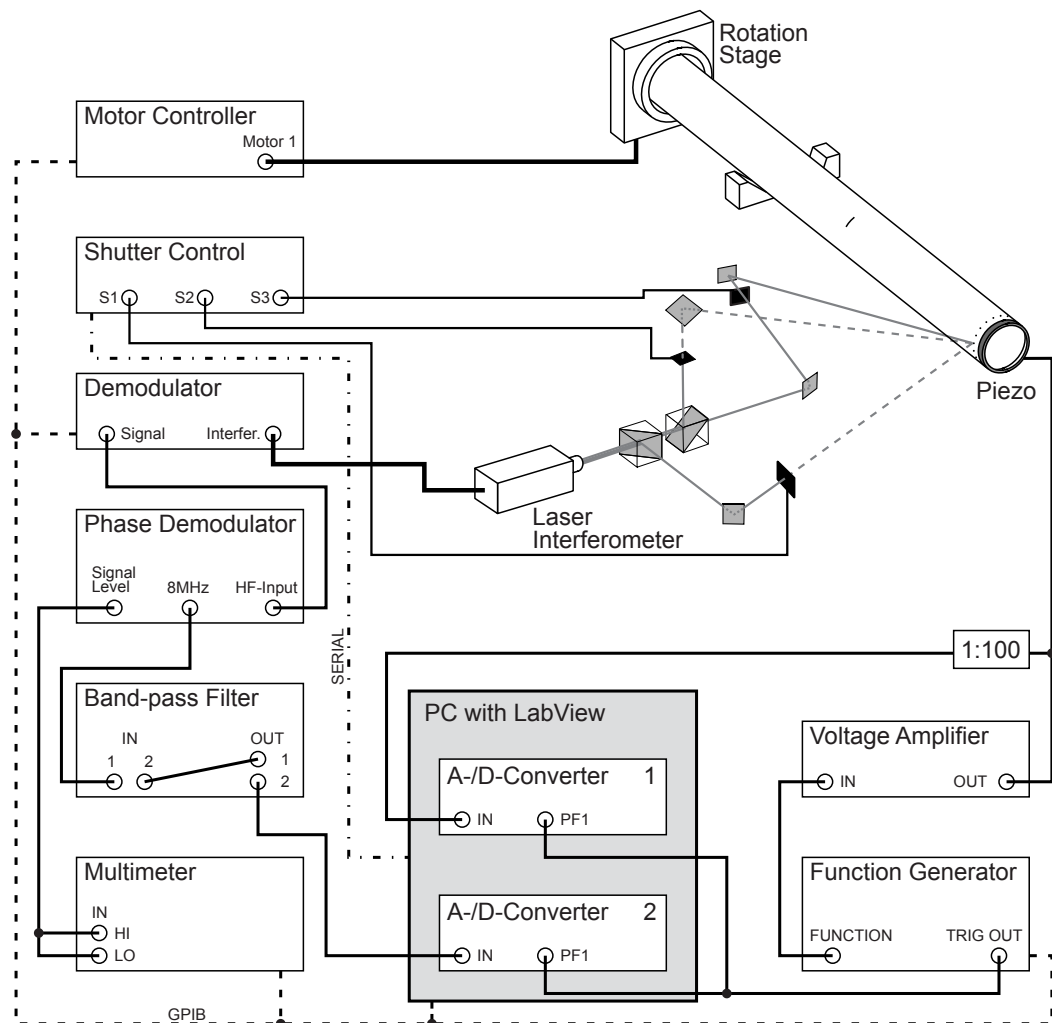
Figure 4.6: Experimental setup

- The excitation signal is generated in the computer, and the discrete values are loaded via GPIB into the function generator (Stanford DS345). The analog output signal is transferred to the amplifier. The SRS DS345 also generates the trigger signal (20 Hz).

- The signal from the function generator has an amplitude of ± 1 V and is amplified by the voltage amplifier (Krohn-Hite 7500) by a factor of 100.

- This excitation signal is used to drive the piezoelectric transducer which generates waves in the samples (Chapter 4.2.1). To monitor the amplified signal, it is attenuated by a factor of 100 and transferred to the computer.

There, it is digitized with an analog-digital converter (National Instruments NI 5911). The vertical resolution is 12 bits at the chosen sampling frequency of $12.5\,\mathrm{MHz}$. The converter is activated using the trigger signal from the function generator.

- The displacements of the surface of the tube are measured with the laser interferometer (Polytec OFV 303) and the optical setup. The shutter control, which is activated by the computer via the serial interface, allows the patching-through of the three beams.

- The signal from the laser is transferred to the original demodulator (Polytec OFV 3001). However, to obtain more accurate results, a high-resolution phase demodulator (MHPD 004) which was developed at the Center of Mechanics is used for the demodulation of the signal. The OFV 3001 is only used for the computer-controlled focussing of the laser.

- The voltage signal from the demodulator, which is proportional to the surface displacement, is analog band-pass filtered (Krohn-Hite 3988).

- A second analog-digital converter (NI 5911) is used to digitize the filtered displacement signal.

- The value of the signal level from the MHPD 004 is proportional to the focussing status of the laser. It is read out by a multimeter (Fluke 8842A) and transferred to the computer via GPIB. The implemented auto-focussing routine is based on this parameter.

- The rotation stage (Newport M-URM 100ACC) is driven by the motor controller (Newport MM 100 DC) and allows for the accurate rotation of the test specimen with a resolution of $1/1000^\circ$.

4.2.1 Specimen setup and excitation

Instead of moving the laser and the optical setup, the test specimen is mounted in a rotation stage at one end. The tube is clamped into position with three screws, covered with silicone caps to minimize reflections (Fig. 4.7 left). In addition to the clamping, the sample is supported by a styrofoam v-block which generates only negligible reflections. It is important to keep the distance between the rotating sample and the three-dimensional vibrometer constant. Otherwise, the rays cannot be focused into one point for all measuring locations. For this purpose, the tube must be aligned exactly with the rotational axis of the stage. This is achieved by adjust-

ing the three screws until the tube and the rotation stage are concentric with an esti-mated accuracy of about 0.1 mm. A gauge is used for verification. The position of the styrofoam support is tuned with two translation stages.

The three-dimensional vibrometer is mounted completely on a separate plate to avoid long setup times. The plate can be positioned by using a rail system horizon-tally and adjustable posts vertically. In the next step, the three laser beams are guided onto one spot by trimming the mirrors.
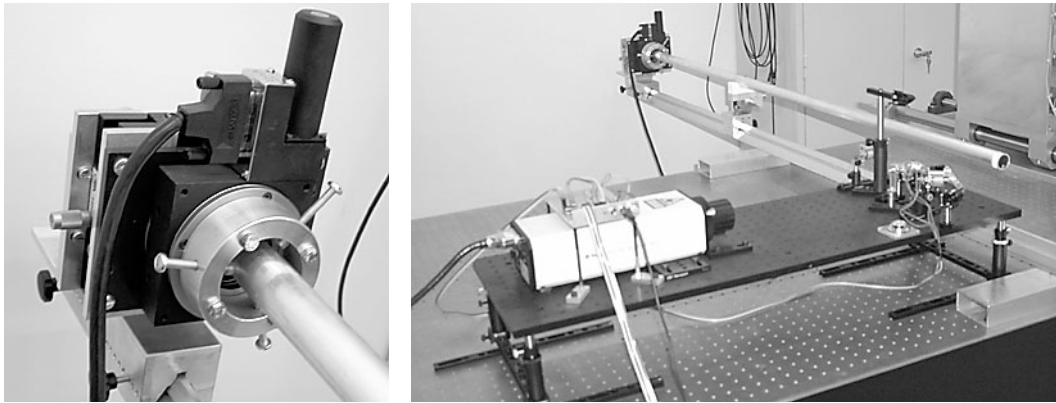
Figure 4.7: Rotation stage with mounted tube. Three screws are used for positioning. Rubber caps minimize reflections (left). The right picture shows the experimental setup on the optical table. The three-dimensional vibrometer is mounted on a separate plate, adjustable in the horizontal plane and in height.

Since the laser rays are not perpendicular to the surface of the sample, retro-reflec-tive tape must be used to guarantee reflection into the incident direction. The dis-placement histories are measured at the beginning of the tube, right adjacent to the piezo element. This allows the separation of the excitation signal and the scattered field and, thus, the determination of the propagation direction.

A piezoelectric transducer is used for the excitation of the waves. A longitudi-nally polarized piezoceramic ring (Ferroperm, Pz26) is glued to the front surface at one end of the tube with a fast-cure two-component epoxy (Perma Bond, double bubble). The radius and the thickness of the piezo match the dimensions of the test specimen, while the length is 2 mm. An electric field with an axial polarization is applied to the piezo. With this configuration, mainly the axial displacements are excited. Even though the radius of the piezo ring is chosen to match the tube, it is impossible to achieve a perfectly axisymmetric excitation due to geometrical and positioning inaccuracies and the effect of the glue.

In the following experiments, 10 cycles of a sine at a center frequency of 200 kHz, multiplied with a Hanning window, are used as excitation functions.

4.3 Measuring sequence

The entire experiment is controlled via the computer and LabView and is fully automated. An outline of the measuring sequence is shown in Fig. 4.8.
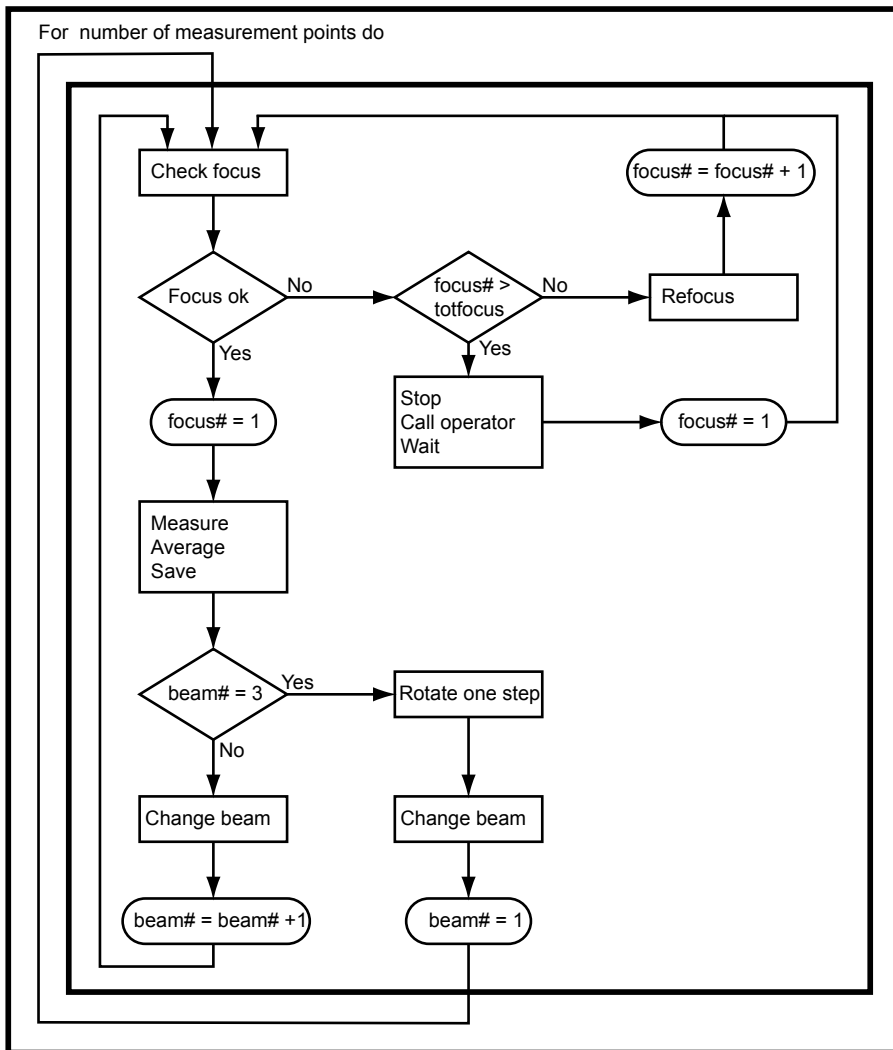
Figure 4.8: Measuring sequence

This sequence is repeated for all measuring positions on the circumference. Prior to every laser measurement, the focus is checked. If the signal level of the demodulator MHPD 004 is below a pre-defined threshold, the auto-focussing routine starts. It refocuses the laser and re-checks the level. This procedure is repeated until the required signal level is reached or the number of refocus attempts (*focus#*)

is larger than the specified number *totfocus*. In this case, the sequence stops and the operator is notified to focus the laser manually.

If the reflection is above the desired level, the measuring routine for the patched-through beam is initiated. The measurements are averaged and saved on the computer. Then, the next beam is selected by activating the shutter control, and the sequence starts again. After the third beam is measured, the tube is rotated to the next measuring position.

4.4 Test specimen

The tested samples are drawn and warm-hardened aluminum tubes with a wall thickness of $h = 2 \text{ mm}$ and a radius of midplane $R = 0.015 \text{ m}$. The material is an aluminum alloy (Alusuisse Extrudal-043 AlMgSi0.5), with Young's modulus $E = 6.9 \cdot 10^{10} \text{ N/m}^2$, mass density $\rho = 2700 \text{ kg/m}^3$, and Poisson's ratio $\nu = 0.34$, according to the manufacturer. The tolerances of the geometrical dimensions conform to DIN 1795. The length of the specimens is approximately 2 meters.

Since the influence of the material parameters is quite large (see Chapter 4.6), the actual values are determined experimentally. The Young's modulus is obtained by observing longitudinal resonance frequencies in the low frequency range (1 - 10 kHz). In this frequency regime waves propagate in tubes as they do in bars (see Dual [10]). Poisson's ratio is determined from wave propagation experiments in the higher frequency range. The phase velocity dispersion diagrams are obtained from experimental data using a *Matrix Pencil* algorithm which is described by Gsell [22] and is based on the *Linear Prediction* method. Since in the isotropic case the phase velocity of the L(0,2) mode approaches the velocity of the first symmetrical plate mode for high wave numbers (Dual [10]), Poisson's ratio can be determined using the known Young's modulus. The determined values are given in Appendix A.1.

Defects are introduced by machining notches of different extents and orientations into the tube. This is done with a small carbide end mill of 0.5 mm and 1 mm diameter (Hitachi Miniature carbide end mill, hyper square long neck, HPSLN-2005C).

4.4.1 Positions and dimensions of the notches

The results of three different notch types are given and discussed in this chapter. The samples are numbered as tube #2, #3, and #5, and the exact dimensions, positions and orientations of the notches are given in the following drawings. The tubes are plotted in a developed view (Fig. 4.9, Fig. 4.10, and Fig. 4.11) with the length on the horizontal and the circumference on the vertical axis. A sectional view of the notch is provided on the right in each case. The unit of the dimensions is mm. The indicated angles on the left vertical axis define the orientation of the notch relative to the circumferential position of the first measurement location (which is always at $0°$).

A longitudinal part-through notch is machined into tube #2 (Fig. 4.9, data see Table A.2 in Appendix A.1). The notch is 1 mm deep and originates from the outside. It is 20 mm long and 0.5 mm wide. This results in approximately 0.26% of the cross-sectional area.
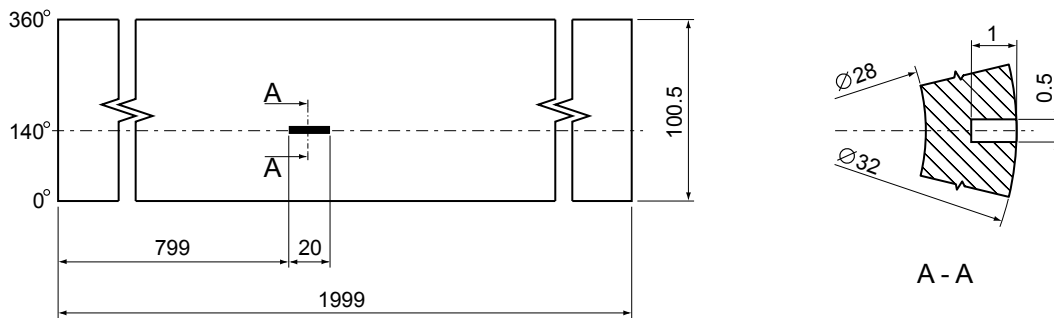
Figure 4.9: Tube #2 with a longitudinal part-through notch.

A circumferential part-through notch with depth 1 mm is machined into tube #3 (Fig. 4.10, data see Table A.2 in Appendix A.1). It is 1 mm wide and has a circumferential extent of 8.5 mm which corresponds to approximately $30°$. About 4.3% of the cross-sectional area are removed in this case.

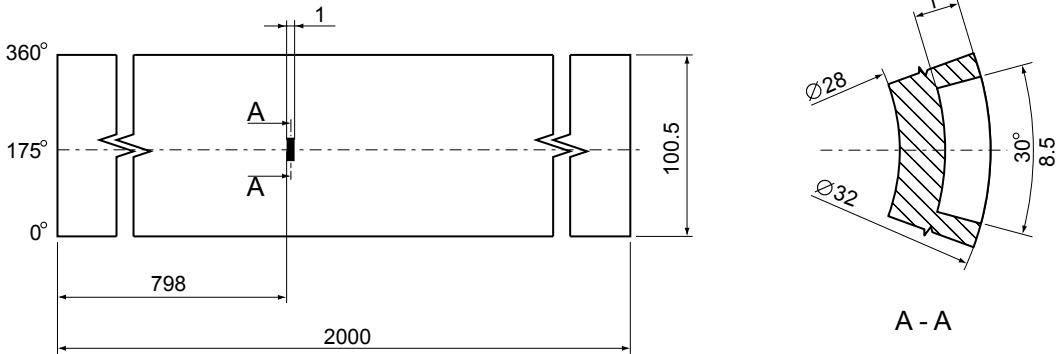**Figure 4.10:** Tube #3 with a circumferential part-through notch.

Tube #5 (data see Table A.2 in Appendix A.1) contains a part-through notch (1 mm deep) which is orientated at a 45 degree angle with respect to the axial direction (Fig. 4.11). The notch is 0.5 mm wide and 11 mm long.
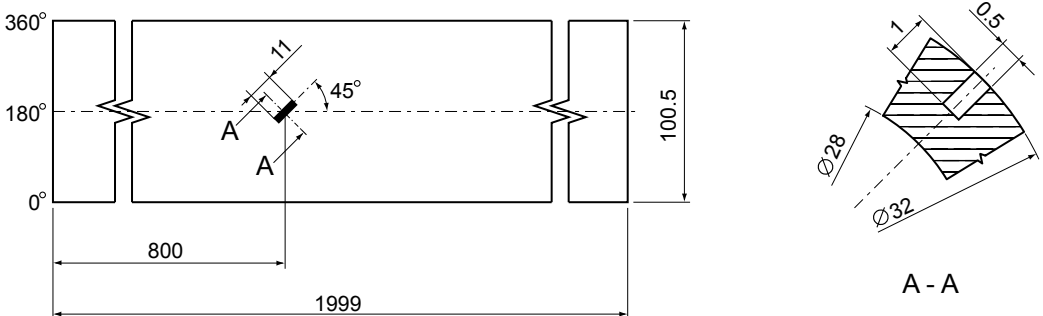

Figure 4.11: Tube #5 with a part-through notch, orientated at a 45 degree angle with respect to the axial direction.

4.5 Results

As excitations in the performed experiments, 10 cycles of a sinusoid at $200\,\text{kHz}$ are multiplied with a Hanning window and applied to the transducer. The piezo element (Ferroperm Pz26) is fixed to the left end of the tubes (see Chapter 4.2.1). The right ends of the samples are clamped in the rotation stage, and the styrofoam block is positioned $1.1\,\text{m}$ away from the piezo ring. The band-pass filter is set to $10\,\text{kHz}$ and $400\,\text{kHz}$, respectively. Each measurement is averaged 150 times (if not stated otherwise) with a trigger frequency of $20\,\text{Hz}$. The displacements are recorded along a circumference approximately $5\,\text{mm}$ away from the piezo at the left end.

4.5.1 Circumferential notch

A first experiment is performed with tube #3 (see Fig. 4.10) with a circumferential part-through notch. In this case, the measurements are taken in 53 points distributed equally along the entire circumference. The center of the notch is positioned at an angle of approximately $175°$ relative to the first measurement location. Fig. 4.12 shows the radial, tangential, and axial displacements as a function of time in one of the measuring positions. They are calculated from the recorded displacements u_1, u_2, and u_3, using Eqs. (4.2) - (4.4). The displacements are normalized with respect to the maximum axial amplitude.

This experiment corresponds to the numerical simulation used for the verification of the TRNS method (Chapter 3.3). Therefore, the measured time histories can be compared to the ones recorded during the simulation (Fig. 3.9). During the excitation, the tangential displacement is not zero in the experiment and the radial displacement is larger than in the simulation. This is due to the non-axisymmetric positioning and the coupling between axial and radial displacements in the piezoelectric ring. The scattered field originating from the notch is non-axisymmetric and its start at around $350\,\mu s$ is best determined from the tangential displacements. This matches the findings of the corresponding simulation.
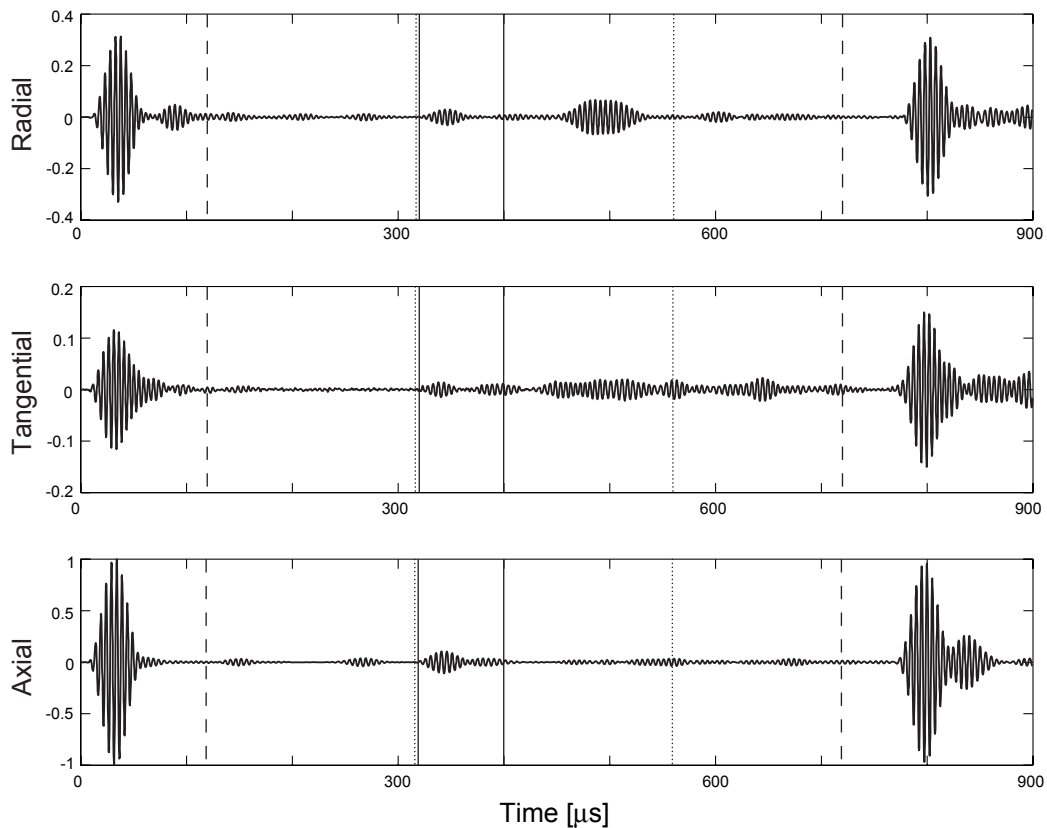
Figure 4.12: Recorded displacement histories of the scattered field from a circumferential notch in tube #3 (data see Table A.2 in Appendix A.1). The measurement is taken in one point on the outer surface of the tube at the left end close to the piezo element. The solid, dotted, and dashed vertical lines define the portions of the signals which are played back. The signals are normalized with respect to the maximum recorded axial displacement.

In a first TRNS, the time histories between $320\,\mu s$ and $400\,\mu s$, marked by the solid vertical lines in Fig. 4.12, are used for the simulation. This corresponds to the first reflections from the notch. A structure with material and geometrical parameters (see Table A.2 in Appendix A.1) equivalent to the values of tube #3 (but without the notch) is implemented in the fourth-order finite-difference code. The selected time range of the displacements of all 53 measuring locations are time reversed and applied at the corresponding circumferential positions on the outer surface at the left end. The simulation parameters used are provided in Chapter 4.6. The focussing of the played back waves is again most visible in the stress components which are shown in Fig. 4.13 at the time when the maximum amplitude occurs. In Fig. 4.13 and the following figures, the tube is plotted in a developed

view, with the axial length on the horizontal and the circumference on the vertical axis. For better visualization, the circumference is enlarged.
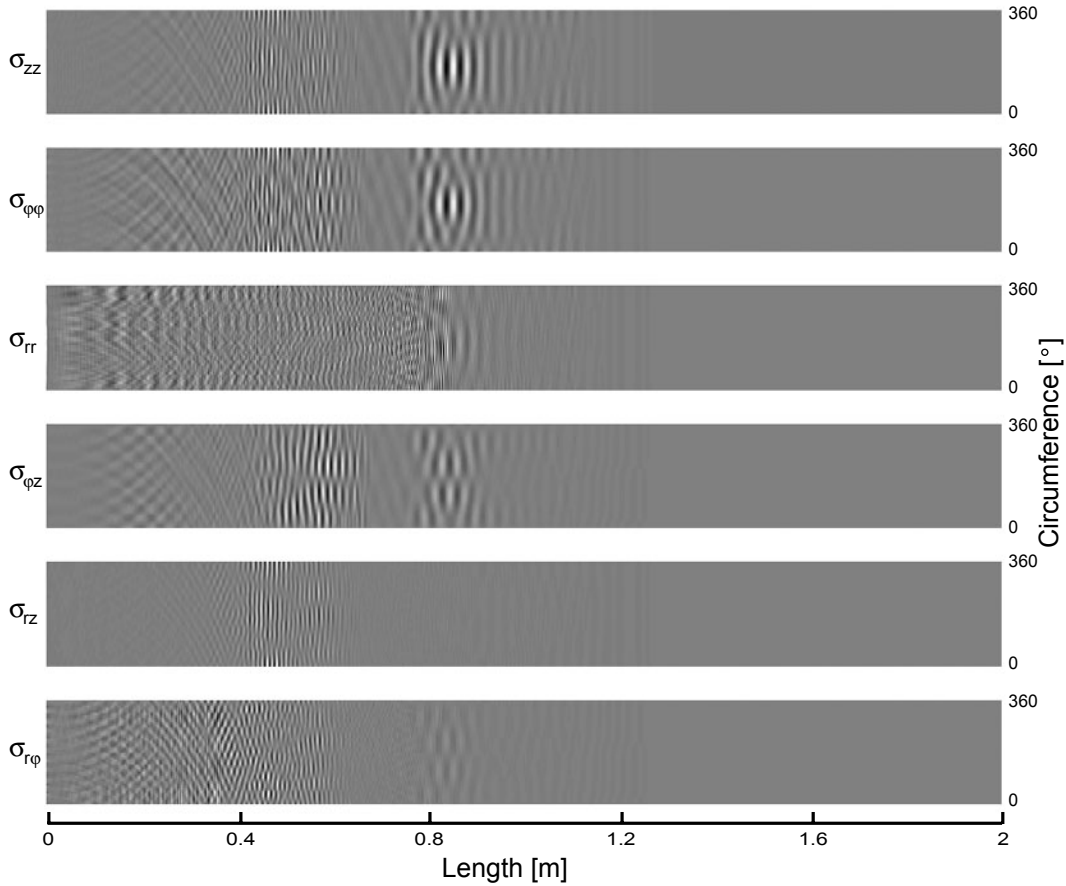
Figure 4.13: Stress components of the TRNS of an aluminum tube (see Table A.2 in Appendix A.1) with a circumferential part-through notch 0.8 m from the left end. The first reflections of the scattered field measured in 53 points distributed around the circumference are played back. The axial and tangential positions of the notch are clearly visible and can be determined. Again, the tube is plotted in a developed view, and the circumference is enlarged for better visualization.

The axial and circumferential position and the orientation of the notch are visible in the stress components. The stress components σ_{zz} and $\sigma_{\varphi z}$ are shown in detail at the position of the notch in Fig. 4.14 (a) and (b), respectively. The axial position is determined in the axial normal stress component. The notch originates at the axial position with the largest difference between dark and white. The absolute values of the positions are calculated by using the known geometry of the test sample and the discretization parameters. For the present experiment, this is at a length of 0.839 m [Fig. 4.14 (a)].
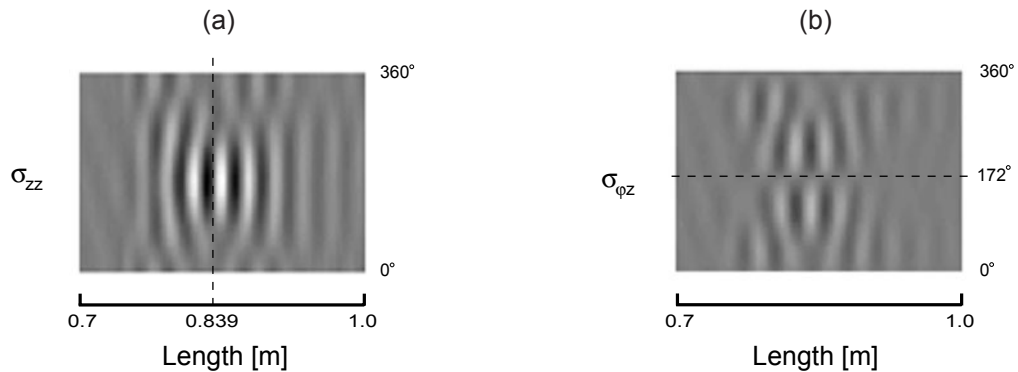
Figure 4.14: Detailed view of the stress components σ$_{zz}$ (a) and σ$_{φz}$ (b) at the position of the notch for the TRNS with 53 points excited. The axial and circumferential position of the notch are marked with dashed black lines in the normal stress component σ$_{zz}$ and the shear stress component σ$_{φz}$, respectively. The absolute values can be determined according to the known discretization parameters and the geometry of the sample.

The tangential position can be determined from the shear stress component $\sigma_{\varphi z}$, seen again, at the border between dark and white. The circumferential position of the center of the notch turns out to be at $172°$ relative to the first measurement location. While the tangential position is quite accurate, small deviations in the axial location of the notch are observed. However, the accuracy is within the range of the wavelength. Possible explanations for this deviation in the axial position are given in Chapter 4.6.

To obtain a higher accuracy, one can play back not only the first reflections, which can be interpreted as the fastest wave mode (with large wavelength) generated at the defect, but also the slower modes with shorter wavelengths. Therefore, the time signals between $320\,\mu s$ and $560\,\mu s$ are played back (marked by the dotted vertical lines in Fig. 4.12). This time range contains the first, mainly axial reflection and also the mode with dominant radial displacement at around $500\,\mu s$. The obtained stress component σ_{zz} is shown in Fig. 4.15.
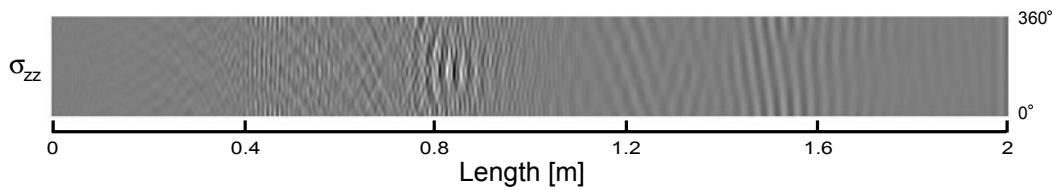
Figure 4.15: Stress component σ_{zz} of the TRNS with the first two reflected modes played back. Despite a higher noise level, the circumferential and axial positions of the notch can be determined more accurately thanks to the smaller wavelength and the interference of the two modes.

Because more noise and measurement errors are included in the longer retransmitted signals, the overall impression of the TRNS is less clear now. However, since the region of the notch is known from the previous TRNS, one can zoom onto this part to determine the position and extent of the notch, as shown in Fig. 4.16.
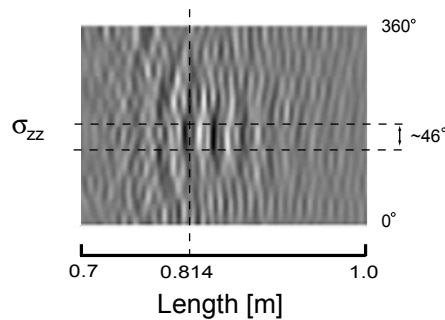
Figure 4.16: Detailed view of stress component σ_{zz} at the position of the notch for the TRNS with 53 points excited. The axial and circumferential positions of the notch are marked with dashed black lines.

Even with the smaller wavelength, a slight axial offset is detected. However, the deviation is smaller than 2%. Possible reasons for this axial offset are discussed in Chapter 4.6.

In a next TRNS, the same part of the recorded displacements that was used in the first simulation for this sample are played back. However, this time only ten points distributed equally around the circumference at the left end are excited. The retransmitted waves are still focused at the position of the notch as can be seen in the axial normal stress component in Fig. 4.17.
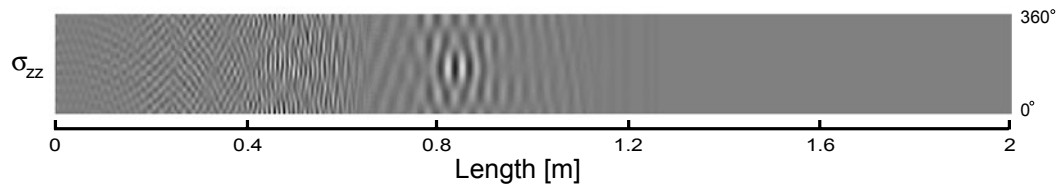
Figure 4.17: Stress component σ_{zz} of the TRNS when only ten points distributed equally around the circumference at the left end are excited. The circumferential and axial positions of the notch can still be determined with the known discretization parameters.

When measuring only a few points along the circumference, special care must be taken when calculating the displacement values to apply in the simulation from the measured displacements (see Chapter 4.1.1). Since the circumferential step $\Delta\varphi$ is much larger, Eq. (4.5) is no longer accurate. Therefore, at each circumferential position, two more measurements should be taken at locations with a small angular step size. Using these three-point groups, the correct excitation values for the TRNS can be calculated.

In a last TRNS of tube #3, the complete recorded displacement histories between the excitation and the first reflection from the right end, which is the range between $120\,\mu s$ and $720\,\mu s$ (marked by the dashed vertical lines in Fig. 4.12), are time reversed and played back. Again, the measurements of all 53 locations are excited in the simulation. The stress components at the time with maximum amplitude are shown in Fig. 4.18. Although increased noise and more errors are contained in these signals, the TRNS still focuses, and the notch and its position can be determined. This is an important finding because it means that the defect can be discovered without interpreting or analyzing the recorded time signals. Especially in cases where the excitation is no longer axisymmetric or if the scattered field is very small, the determination of the first reflected parts from the defect in the measured signals is no longer possible. In this case, the time signals can be played back in their entirety.

σ_zz

360°

0°

0   0.4   0.8   1.2   1.6   2

Length [m]
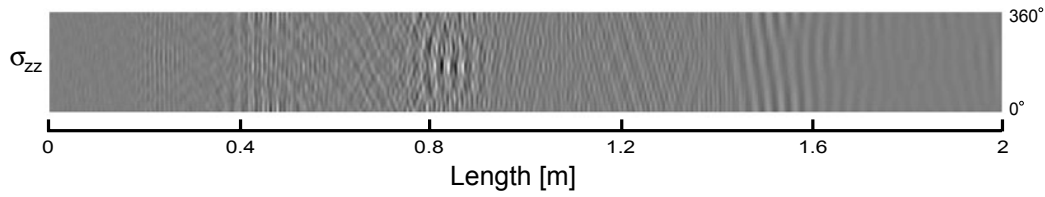
Figure 4.18: Stress component σ_{zz} of the TRNS of an aluminum tube (see Table A.2 in Appendix A.1) with a circumferential part-through notch 0.8 m from the left end. The complete measured displacement histories of the 53 points distributed equally along the circumference are time reversed and played back. The axial and tangential positions of the notch are still visible and can be determined.

4.5.2 Longitudinal notch

The results for the detection of a longitudinal part-through notch (tube #2, Fig. 4.9) are presented next. The notch is positioned at an angle of approximately $140°$ relative to the first measurement location, and 108 points are measured along one circumference.

Fig. 4.19 shows three stress components at the time of the maximum amplitude of a TRNS where the first reflected mode is played back in all 108 points.

σ_zz

360°

0°

σ_φφ

360°

0°

σ_φz

360°

0°

0   0.4   0.8   1.2   1.6   2

Length [m]
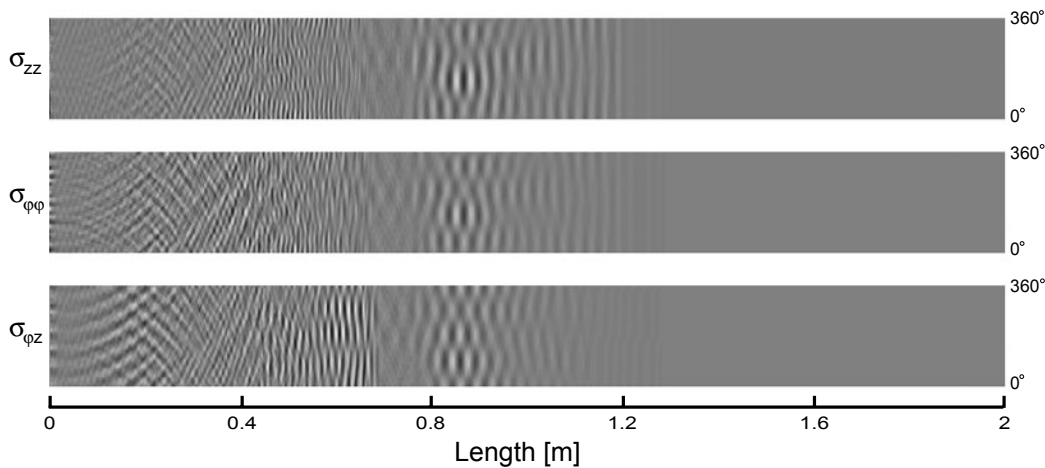
Figure 4.19: Stress components σ_{zz}, $\sigma_{\varphi\varphi}$, and $\sigma_{\varphi z}$ of the TRNS of an aluminum tube (see Table A.2 in Appendix A.1) with a longitudinal part-through notch 0.8 m from the left end. The first reflections of the scattered field measured in 108 points distributed equally around the circumference are played back. The axial and tangential positions of the notch are visible and can be determined.

The axial and circumferential positions of the notch are, once again, determined from the normal stress σ_{zz} and the shear stress $\sigma_{\varphi z}$, which are shown in Fig. 4.20.
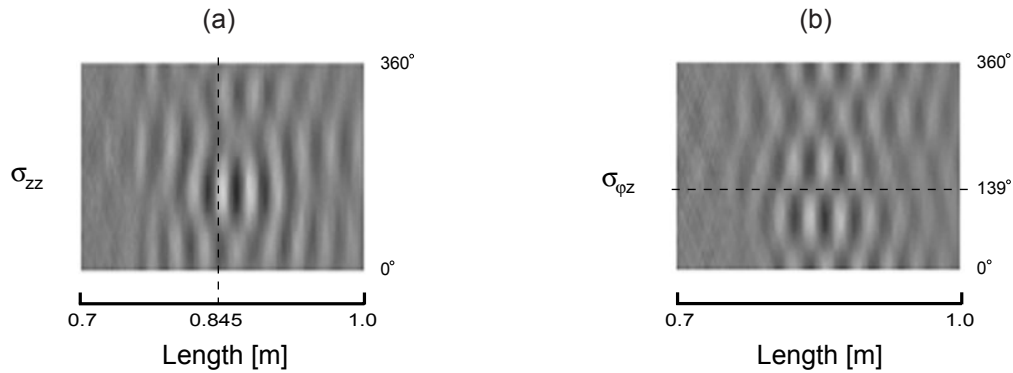
Figure 4.20: Detailed view of the stress components σ_{zz} (a) and $\sigma_{\varphi z}$ (b) at the position of the longitudinal notch for the TRNS with 108 points excited. The axial and circumferential positions of the notch are marked with dashed black lines in the normal stress σ_{zz} and the shear stress component $\sigma_{\varphi z}$, respectively. The absolute values can be determined with the known discretization parameters and the geometry of the sample.

Even for this very small defect (only 0.26% of the cross-sectional area are removed), the axial and circumferential positions can be determined. While the circumferential location is correct, the beginning of the notch is detected to be slightly too far away in axial direction.

Fig. 4.21 shows the normal stress component σ_{zz} when the complete recorded displacement histories between the excitation and the reflection from the right end are retransmitted. In spite of the noise, the position of the notch is still detectable with some TRNS experience.
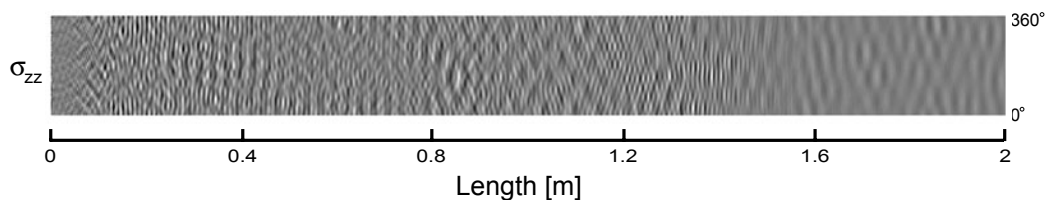
Figure 4.21: Axial normal stress component of the TRNS of an aluminum tube (see Table A.2 in Appendix A.1) with a longitudinal part-through notch 0.8 m from the left end. The complete measured displacement histories of the 108 points distributed equally along the circumference are time reversed and played back. The axial and tangential positions of the notch are still visible and can be determined.

Again, one can obtain the axial position from the zoom-picture of the axial normal stress in the notch region as shown in Fig. 4.22. No interpretation of the time signal is necessary.
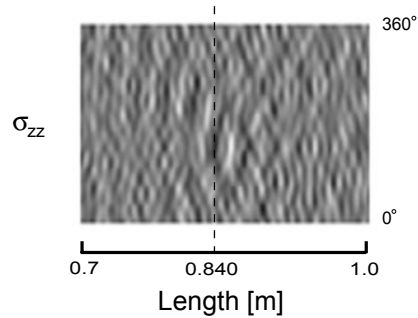
Figure 4.22: Detailed view of stress component σ_{zz} at the position of the notch for the TRNS with 108 points excited. The axial positions of the notch can still be determined with some TRNS experience.

Since the complete recorded signal is played back the parts with smaller wavelength are also included. Therefore, the accuracy of the axial position can be increased. The longitudinal notch is determined to be located at an axial distance of 0.84 m. However, because more noise is retransmitted as well the interpretation is more difficult. Although the deviation is in the range of 5%, this very small defect is still successfully detected. Possible reasons for this axial offset are discussed in Chapter 4.6.

4.5.3 45-degree notch

To check the ability of the TRNS method to detect the orientation of the notches, tube #5 (see Table A.2 in Appendix A.1)with a part-through notch at an angle of $45°$ with respect to the axial direction is investigated (Fig. 4.11). Therefore, the displacements are recorded in 108 points, and each measurement is averaged 300 times. The center of the notch is positioned at an angle of approximately $180°$ relative to the first measurement location. Since the notch is also 0.8 m away from the measurement positions, the same time range used for the circumferential notch is played back. The stress components σ_{zz} and $\sigma_{\varphi\varphi}$ are shown in Fig. 4.23 at the time with the maximum amplitudes.

Figure 4.23: Stress components σ_{zz} and $\sigma_{\varphi\varphi}$ of the TRNS of an aluminum tube (see Table A.2 in Appendix A.1) with a part-through notch at 45⁰, 0.8 m from the left end. The first reflections of the scattered field measured in 108 points distributed along the circumference are played back. The axial and tangential positions and the orientation of the notch are visible and can be determined.

In addition to the axial and tangential positions of the notch, the orientation is also derived from the normal stress component as shown in Fig. 4.24.
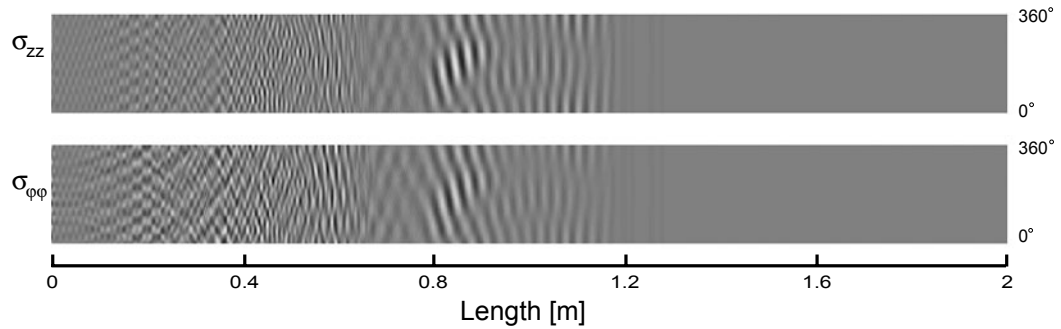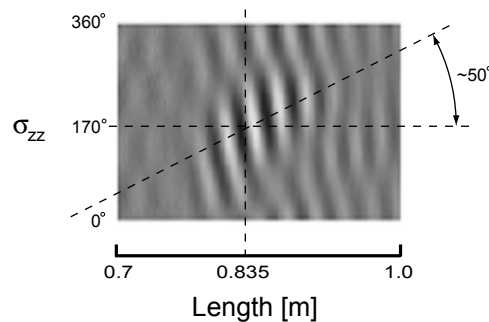

Figure 4.24: Detailed view of the stress component σ_{zz} at the position of the part-through notch for the TRNS with 108 points excited. The axial and circumferential positions as well as the orientation can be determined using the known discretization parameters and the geometry of the sample.

Since the circumferences are plotted enlarged in all previous TRNS pictures, one must use the discretization parameters to calculate the orientation angle, which is detected to be approximately $50°$. The deviation of the axial position is again in the range of the wavelength of the first played back mode.

Therefore, a second TRNS is performed where the reflections from the first two modes are played back. The axial normal stress component σ_{zz} for this case is shown in Fig. 4.25.
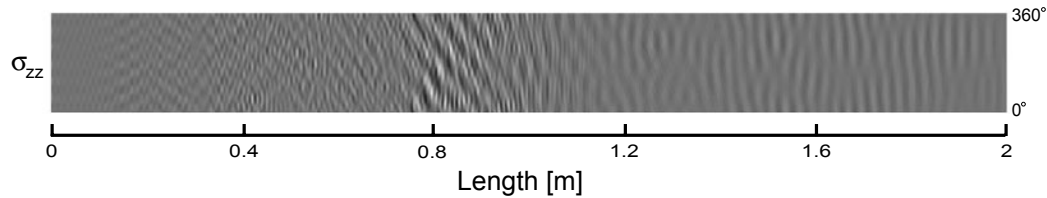
Figure 4.25: Axial normal stress component of the TRNS of an aluminum tube (see Table A.2 in Appendix A.1) with a part-through notch at 45°, 0.8 m from the left end. The first two reflected modes are played back in 108 points distributed along the circumference. The axial positions can be determined more accurately due to the smaller wavelength.

Again, one can obtain the axial position from the zoom-picture of the axial normal stress in the notch region as shown in Fig. 4.22. No interpretation of the time signal is necessary.
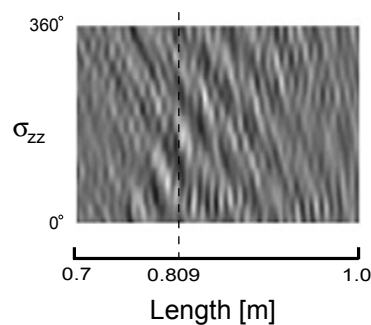
Figure 4.26: Detailed view of stress component σ_{zz} at the position of the part-through notch at 45° for the TRNS with 108 points excited. Since the first two modes are played back and in spite more noise in the signal, the axial position of the defect can be determined more accurately.

The smaller wavelength allows a more accurate detection of the axial position of the notch which is determined to be at a distance of 0.809 m. This corresponds to an error of approximately 1%.

4.6 Discussion of the results

The true positions of the notches in the experiments can only be accurately determined if the time reverse numerical simulations are highly accurate. Since the fine grid which would be necessary for the second-order algorithm exceeds the capacity of currently available computational hardware, the fourth-order code is used for all of the above TRNS. In radial and axial directions three and 1250 cells are used in all TRNS, while the number of grid points in circumferential direction corresponds to the number of measurement points (53 locations for the circumferential and 108 points for the longitudinal and 45-degree notches). The tubes are implemented with stress-free boundaries, and neither the piezo element nor the styrofoam block nor the rotational stage are included in the simulation.

The performed experiments show that the defects are detected in all cases and that even for very small defects, the TRNS method delivers reliable results for the axial and circumferential position and the orientation of notches which are situated far away from the measurement locations. Several reasons can cause the deviations in the circumferential and axial coordinates, which are 9 mm and 14 mm for the 45-degree and the circumferential notches, respectively. This results in an error which is less than 2%. A larger deviation of 40 mm, which corresponds to 5%, is obtained for the longitudinal notch. However, since this notch is very small (only 0.26% of the cross-sectional area are removed), already the detection of it is a good result.

One possibility are errors in the material parameters, which affect the wave propagation. Variations of Young's modulus show a detectable influence on the positions of the maximum interference. Therefore, the material parameters were determined experimentally as described in Chapter 4.4. The used parameters are given in Table A.2 in Appendix A.1.

In a next step, the wall thickness and the radius of midplane of the tube are varied. While the variation of the wall thickness showed only negligible influence on the position of the maximum amplitudes, the radius of midplane effects the location remarkably.

Another possible reason for the axial offset might be the missing piezo element in the simulations and the influence of the retro-reflective tape. The measured signals are used to excite the outside circumference at the free end of the sample in the TRNS. Almost no differences are observed in the axial position of the focussing when the position of the excited circumference is varied within the first 5 mm of the tube, which corresponds to the region of the retro-reflective tape in the experiments. However, the presence of the piezo at the end influences the stiffness of the

tube and therefore the wave propagation phenomena.

The used aluminum test samples are drawn and warm-hardened tubes. Especially the drawing-process influences the material behavior and the resulting tubes are no longer isotropic. However, the implemented finite-difference code for the TRNS of the performed experiments is written for isotropic materials. This might be another cause for errors in the determined positions of the notches. Therefore, the implementation of an anisotropic material law in the simulation code might improve the accuracy of the results.

The TRNS method allows the determination of the beginning of a notch, as well as its circumferential extent and orientation, also with only a few measurement points. To establish the length of the defects, an additional experiment and TRNS from the other side of the tube can be performed, which returns the position of the end of the notch.

5. CONCLUSIONS AND OUTLOOK

The experimental results show the applicability of the present TRNS method to the long-range non-destructive testing of large structures. Not only the axial and circumferential positions but also the orientation of defects can be determined. Both, the excitation and the measurements can be reduced to a small area of the structure, which is an important advantage with respect to limited access. Another benefit of the developed method is the elimination of the time-consuming scanning of the whole structure. Since the recorded time signals of the scattered wave field are not analyzed directly, the TRNS method is also applicable for very complex reflected signals. Therefore, it is not necessary to try to excite only a few, or, in the best case scenario, one specific wave mode. Basically, any excitation that generates a scattered field can be applied. Below, some suggestions are listed which aim to further improve the accuracy of the procedure. Finally, some ideas to extend the applicability of the TRNS method are proposed.

- To investigate the influence of the piezo element in the simulations, it could be implemented into the FDM code. This was done by Gsell [22] for the second-order finite-difference algorithm. However, the impact of the layer of glue between piezo and tube is very difficult to describe and has not been taken into consideration.

- Another possible approach is the non-contact excitation of structural waves using electromagnetic acoustical transducers (EMAT) [53], or the point source excitation of the structure with a small piezo element or a laser. However, since the experiments are repeated several times, the damage of the structure by the laser must be prevented.

- To further improve the method, the detection of the time and region with maximum amplitude could be automated. Since the refocussing sequence has a characteristic pattern, a picture recognition method could possibly be implemented. A simple search for the maximum value of the different stress components did not work reliably due to high amplitudes during the excitation of the recorded time histories and reflections from boundaries. Especially for low signal-to-noise ratios, only ambiguous maxima were detected by a simple maximum search. However, by carefully observing the development of the retransmitted field the exact position could nevertheless be determined. This step, in particular, demands some experience and a thorough understanding of the TRNS method.

- Especially when dealing with larger reflections, it is conceivable that the ratio of the maximum refocused amplitude and the excited amplitude are factors for the characterization of the defect. If the maximum refocused amplitude is normalized with respect to the number of retransmitted points and the damping coefficients are known, it might be possible to determine the depth of the defect by comparing the results with the reflection coefficients for different notches. This would be an important finding for the quantitative non-destructive evaluation (QNDE). The reflection coefficients for guided waves from circumferential defects are studied by Alleyne et al. [1] using a membrane model for through-thickness notches and an axisymmetric model for part-through notches which extend over the full circumference. For the investigation of the coefficients of cracks, a fracture mechanics approach must be used as is done e.g. by Ditri [9].

- It is possible that the detectability can be improved by incorporating modelling information about the occurring wave modes in the tube at a particular frequency. An idea is that not only the ring on the surface of the simulation is excited, but the entire cross-sectional area at the measurement position. Therefore, the distribution of the displacement components as a function of the radial coordinate must be determined. Since the reflected signals are relatively narrowband in frequency, one can imagine the measured circumferential displacement distribution on the surface as a superposition of the corresponding displacements of all existing wave modes at the particular frequency. The idea is to determine the number of wave modes and their amplitudes by fitting the superimposed amplitudes at the surface on to the measured displacement field at each specific time. With the known amplitude ratios, number of waves, and geometrical and mate-

rial parameters of the sample, the displacement distributions for each mode can be calculated using the numerical analytical method described in Chapter 1.2. The superimposed displacement field can then be applied as an excitation for the entire cross-sectional area. Even though this might lead to an increase of the amplitude maxima, as was shown for a purely simulated experiment, it results in many additional calculation steps, since the amplitude ratios and wave modes must be determined for each time step during the retransmission sequence.

- If only a part of a large structure is of interest, the implementation of absorbing boundary conditions (see Chapter 2.1) might be very helpful in the truncation of the computational domain.

- In order to apply the TRNS method to tubes filled with fluid, the interaction between the solid structure and the fluid must be implemented in the simulation code. This is the subject of another project currently conducted at the Institute of Mechanical Systems by Frank May.

- In order to successfully use the playback concept, one must ensure that the simulated structure corresponds exactly to the performed experiment. This includes not only the tube itself, but also the environment. Therefore, known objects, e.g. welding seams, isolation, or surrounding soil must be taken into account.

- Even if multiple defects are present in the tested sample, the TRNS method should theoretically still be capable to detect all of them. In that case, the recorded time signals contain several scattered fields from the different defects. When playing back the time reversed signals into the simulated structure, the result is a refocussing at the position of the closest defect. However, because the refocussing is also achieved if only parts of a scattered field are retransmitted, an amplitude increase should also be detectable at the positions of the other defects. This works as long as some of the scattered fields from defects further away arrive at the measuring locations and are being recorded and retransmitted. First examples of completely simulated experiments with two notches showed that both defects can be detected successfully.

- For further applications and the wide use of the TRNS method for NDT and QNDE, the relations between the minimum number of recording positions, the maximum signal to noise ratio (SNR) and the minimum detectable defect size must be determined. Therefore, an experimental and numerical study with different notch sizes and variable numbers of recording points distributed around the circumference must be performed and evaluated.

- The developed TRNS method is not at all restricted to the NDT of the cylindrical structures described in the present work. It can be applied to any structure, as long as the sample is represented accurately in a numerical simulation with respect to geometry, boundary conditions, and material law. Possible applications are the NDT of rods or plates as well as the interpretation of classical UT signals.

APPENDIX

A.1 Data tables

The material, geometrical, and discretization parameters of the performed and discussed simulations, examples, and experiments are given in the two tables below.

name	dispersion curves	numerical example #1	numerical example #2	stability analysis	numerical dispersion
chapter	1.2	2.2.5	2.2.5	2.3	2.4.1
figure(s)	1.1 - 1.5	2.4	2.5	2.6	2.7, 2.13
Young's modulus [N/m^2]	$6.9*10^{10}$	$7.2*10^{10}$	$7.2*10^{10}$	$7.2*10^{10}$	$7.2*10^{10}$
mass density [kg/m^3]	2700	2700	2700	2700	2700
Poisson's ratio	0.34	0.33	0.33	0.33	0.33
radius of mid-plane [m]	0.016	0.016	0.016	0.016	0.016
wall thickness [mm]	2	2	2	2	2
length [m]	-	0.6	0.3	0.08	0.72
notch	-	-	tangential	-	-
notch length / width / depth [mm]	-	-	10 / 1 / 1	-	-
radial / tangential / axial cells	-	3 / 30 / 750	5 / 100 / 300	6 / 120 / 100	3 / 3 / variable

Table A.1: Material, geometrical, and discretization parameters

name	comparison 2nd-4th	plate example	verify TRNS	tube #2	tube #3	tube #5
chapter	2.5.3	3.1.3	3.3	4.5.2	4.5.1	4.5.3
figure	2.14, 2.15	3.1 - 3.5	3.8 - 3.15	4.19 - 4.21	4.12 - 4.18	4.23, 4.24
Young's modulus [N/m^2]	7.2*10^{10}	7.2*10^{10}	6.9*10^{10}	6.78*10^{10}	6.78*10^{10}	6.78*10^{10}
mass density [kg/m^3]	2700	2700	2700	2700	2700	2700
Poisson's ratio	0.33	0.33	0.34	0.35	0.35	0.35
radius of midplane [m]	0.012	-	0.015	0.0149	0.0149	0.0149
wall thickness [mm]	2	2 (plate)	2	2.1	2.1	2.1
length [m]	0.15	0.3*0.3	2	1.999	2.000	1.999
notch	-	-	tangential	axial	tangential	45 degree
notch length / width / depth [mm]	-	-	9.5 / 1 / 1	20 / 0.5 / 1	8.5 / 1 / 1	11 / 0.5 / 1
radial/tangential/ axial cells	3/400/ 750(2nd) 3/80/150(4th)	600/600 (x/y)	4 / 106 / 2000	3 / 108 / 1250	3 / 53 / 1250	3 / 108 / 1250

Table A.2: Material, geometrical, and discretization parameters

A.2 Coefficient vectors for the second-order code

As an example, the complete form of the explicit Eq. (2.5) for the calculation of the radial displacement components at the next time step for second-order scheme and the components of the vectors $\boldsymbol{a}_r$ are given below:

$$
\begin{aligned}
\overset{n+1}{\underset{j,i,k}{u_r}} = {}& 2 \cdot \overset{n}{\underset{j,i,k}{u_r}} - \overset{n-1}{\underset{j,i,k}{u_r}} + \frac{\Delta t^2}{\rho}\left(\frac{1}{2 \cdot r_k} - \frac{1}{\Delta r}\right) \cdot \overset{n}{\underset{j,i,k-1}{\sigma_{rr}}} + \frac{\Delta t^2}{\rho}\left(\frac{1}{2 \cdot r_k} + \frac{1}{\Delta r}\right) \cdot \overset{n}{\underset{j,i,k+1}{\sigma_{rr}}} \\[2em]
& - \frac{\Delta t^2}{2 \cdot \rho \cdot r_k} \cdot \overset{n}{\underset{j,i,k-1}{\sigma_{\varphi\varphi}}} - \frac{\Delta t^2}{2 \cdot \rho \cdot r_k} \cdot \overset{n}{\underset{j,i,k+1}{\sigma_{\varphi\varphi}}} - \frac{\Delta t^2}{\rho \cdot \Delta\varphi \cdot r_k} \cdot \overset{n}{\underset{j,i-1,k}{\sigma_{r\varphi}}} \\[2em]
& + \frac{\Delta t^2}{\rho \cdot \Delta\varphi \cdot r_k} \cdot \overset{n}{\underset{j,i+1,k}{\sigma_{r\varphi}}} - \frac{\Delta t^2}{\rho \cdot \Delta z} \cdot \overset{n}{\underset{j-1,i,k}{\sigma_{rz}}} + \frac{\Delta t^2}{\rho \cdot \Delta z} \cdot \overset{n}{\underset{j+1,i,k}{\sigma_{rz}}}
\end{aligned} \tag{A.1}
$$

With the vector $\boldsymbol{\sigma}_s$ defined for the present case as

$$
\overset{n}{\underset{j,i,k}{\boldsymbol{\sigma}_s}} = \left\{ \overset{n}{\underset{j,i,k-1}{\sigma_{rr}}} , \; \overset{n}{\underset{j,i,k+1}{\sigma_{rr}}} , \; \overset{n}{\underset{j,i,k-1}{\sigma_{\varphi\varphi}}} , \; \overset{n}{\underset{j,i,k+1}{\sigma_{\varphi\varphi}}} , \; \overset{n}{\underset{j,i-1,k}{\sigma_{r\varphi}}} , \; \overset{n}{\underset{j,i+1,k}{\sigma_{r\varphi}}} , \; \overset{n}{\underset{j-1,i,k}{\sigma_{rz}}} , \; \overset{n}{\underset{j+1,i,k}{\sigma_{rz}}} \right\}^T \tag{A.2}
$$

the vector $\boldsymbol{a}_r$, which is dependent on the discretization parameters Δr, $\Delta\varphi$, Δz, Δt, the mass density ρ, and the radial coordinate r_k, is given as

$$
\begin{aligned}
\underset{k}{\boldsymbol{a}_r} = {}& \left\{ \frac{\Delta t^2}{\rho}\left(\frac{1}{2 \cdot r_k} - \frac{1}{\Delta r}\right), \frac{\Delta t^2}{\rho}\left(\frac{1}{2 \cdot r_k} + \frac{1}{\Delta r}\right), -\frac{\Delta t^2}{2 \cdot \rho \cdot r_k}, -\frac{\Delta t^2}{2 \cdot \rho \cdot r_k}, \right. \\[2em]
& \left. -\frac{\Delta t^2}{\rho \cdot \Delta\varphi \cdot r_k}, \frac{\Delta t^2}{\rho \cdot \Delta\varphi \cdot r_k}, -\frac{\Delta t^2}{\rho \cdot \Delta z}, \frac{\Delta t^2}{\rho \cdot \Delta z} \right\}^T
\end{aligned} \tag{A.3}
$$

The vectors $\boldsymbol{a}_\varphi$ and $\boldsymbol{a}_z$ for the calculation of the tangential and axial components are derived accordingly.

The written out form of Eq. (2.9) to calculate the radial normal stress components yields to

$$
\overset{n}{\underset{j,i,k}{\sigma_{rr}}} = \frac{E \cdot (\nu \cdot \Delta r - 2 \cdot r_k \cdot (1 - \nu))}{2 \cdot r_k \cdot \Delta r \cdot (1 - \nu - 2 \cdot \nu^2)} \cdot \overset{n}{\underset{j,i,k\text{-}1}{u_r}}
$$

$$
+ \frac{E \cdot (\nu \cdot \Delta r + 2 \cdot r_k \cdot (1 - \nu))}{2 \cdot r_k \cdot \Delta r \cdot (1 - \nu - 2 \cdot \nu^2)} \cdot \overset{n}{\underset{j,i,k+1}{u_r}}
$$

$$
- \frac{E \cdot \nu}{\Delta\varphi \cdot r_k \cdot (1 - \nu - 2 \cdot \nu^2)} \cdot \overset{n}{\underset{j,i\text{-}1,k}{u_\varphi}} + \frac{E \cdot \nu}{\Delta\varphi \cdot r_k \cdot (1 - \nu - 2 \cdot \nu^2)} \cdot \overset{n}{\underset{j,i+1,k}{u_\varphi}}
$$

$$
- \frac{E \cdot \nu}{\Delta z \cdot (1 - \nu - 2 \cdot \nu^2)} \cdot \overset{n}{\underset{j\text{-}1,i,k}{u_z}} + \frac{E \cdot \nu}{\Delta z \cdot (1 - \nu - 2 \cdot \nu^2)} \cdot \overset{n}{\underset{j+1,i,k}{u_z}}
$$

(A.4)

With the vector $\boldsymbol{u}_s$ defined for the present case as

$$
\overset{n}{\underset{j,i,k}{\boldsymbol{u}_s}} = \left\{ \overset{n}{\underset{j,i,k\text{-}1}{u_r}} , \overset{n}{\underset{j,i,k+1}{u_r}} , \overset{n}{\underset{j,i\text{-}1,k}{u_\varphi}} , \overset{n}{\underset{j,i+1,k}{u_\varphi}} , \overset{n}{\underset{j\text{-}1,i,k}{u_z}} , \overset{n}{\underset{j+1,i,k}{u_z}} \right\}^T
$$

(A.5)

the vector $\boldsymbol{b}_{rr}$, which is dependent on the discretization parameters Δr, $\Delta\varphi$, Δz, the material parameters E and ν, and the radial coordinate r_k, is given as

$$
\underset{k}{\boldsymbol{b}_{rr}} = \left\{ \frac{E \cdot (\nu \cdot \Delta r - 2 \cdot r_k \cdot (1 - \nu))}{2 \cdot r_k \cdot \Delta r \cdot (1 - \nu - 2 \cdot \nu^2)}, \frac{E \cdot (\nu \cdot \Delta r + 2 \cdot r_k \cdot (1 - \nu))}{2 \cdot r_k \cdot \Delta r \cdot (1 - \nu - 2 \cdot \nu^2)}, \right.
$$

$$
- \frac{E \cdot \nu}{\Delta\varphi \cdot r_k \cdot (1 - \nu - 2 \cdot \nu^2)}, \frac{E \cdot \nu}{\Delta\varphi \cdot r_k \cdot (1 - \nu - 2 \cdot \nu^2)},
$$

(A.6)

$$
\left. - \frac{E \cdot \nu}{\Delta z \cdot (1 - \nu - 2 \cdot \nu^2)}, \frac{E \cdot \nu}{\Delta z \cdot (1 - \nu - 2 \cdot \nu^2)} \right\}^T
$$

The coefficient vectors for the calculation of the other stress components are derived accordingly.

A.3 Coefficient vectors for the fourth-order code

Analogous to the second-order scheme, the explicit equations for the calculation of the displacement and stress components are of the same form as Eqs. (2.5) and (2.9). The vectors σ_s and a_r for the calculation of the radial displacement are given below as an example.

$$
\sigma_s\big|_{j,i,k}^{n} = \left\{ \sigma_{rr}\big|_{j,i,k-1}^{n}, \; \sigma_{rr}\big|_{j,i,k+1}^{n}, \; \sigma_{\varphi\varphi}\big|_{j,i,k-1}^{n}, \; \sigma_{\varphi\varphi}\big|_{j,i,k+1}^{n}, \; \sigma_{r\varphi}\big|_{j,i-3,k}^{n}, \; \sigma_{r\varphi}\big|_{j,i-1,k}^{n} \right.
$$

$$
\left. \sigma_{r\varphi}\big|_{j,i+1,k}^{n}, \; \sigma_{r\varphi}\big|_{j,i+3,k}^{n}, \; \sigma_{rz}\big|_{j-3,i,k}^{n}, \; \sigma_{rz}\big|_{j-1,i,k}^{n}, \; \sigma_{rz}\big|_{j+1,i,k}^{n}, \; \sigma_{rz}\big|_{j+3,i,k}^{n} \right\}^{T}
$$

(A.7)

$$
a_r\big|_{k} = \left\{ \frac{\Delta t^2 \cdot (\Delta r - 2 \cdot r_k)}{2 \cdot \rho \cdot \Delta r \cdot r_k}, \frac{\Delta t^2 \cdot (\Delta r + 2 \cdot r_k)}{2 \cdot \rho \cdot \Delta r \cdot r_k}, -\frac{\Delta t^2}{2 \cdot \rho \cdot r_k}, -\frac{\Delta t^2}{2 \cdot \rho \cdot r_k}, \right.
$$

$$
\frac{\Delta t^2}{24 \cdot \rho \cdot \Delta\varphi \cdot r_k}, -\frac{9 \cdot \Delta t^2}{8 \cdot \rho \cdot \Delta\varphi \cdot r_k}, \frac{9 \cdot \Delta t^2}{8 \cdot \rho \cdot \Delta\varphi \cdot r_k}, -\frac{\Delta t^2}{24 \cdot \rho \cdot \Delta\varphi \cdot r_k},
$$

(A.8)

$$
\left. \frac{\Delta t^2}{24 \cdot \rho \cdot \Delta z}, -\frac{9 \cdot \Delta t^2}{8 \cdot \rho \cdot \Delta z}, \frac{9 \cdot \Delta t^2}{8 \cdot \rho \cdot \Delta z}, -\frac{\Delta t^2}{24 \cdot \rho \cdot \Delta z} \right\}^{T}
$$

The vectors $\boldsymbol{u}_s$ and $\boldsymbol{b}_{rr}$ for the calculation of the radial normal stress for the fourth-order scheme are given below as an example.

$$
\boldsymbol{u}_{s_{j,i,k}}^{n} = \left\{ \begin{array}{l}
u_{r_{j,i,k-1}}^{n}, \quad u_{r_{j,i,k+1}}^{n}, \quad u_{\varphi_{j,i-3,k}}^{n}, \quad u_{\varphi_{j,i-1,k}}^{n}, \quad u_{\varphi_{j,i+1,k}}^{n}, \quad u_{\varphi_{j,i+3,k}}^{n}, \\[2em]
u_{z_{j-3,i,k}}^{n}, \quad u_{z_{j-1,i,k}}^{n}, \quad u_{z_{j+1,i,k}}^{n}, \quad u_{z_{j+3,i,k}}^{n}
\end{array} \right\}^{T}
\tag{A.9}
$$

$$
\begin{aligned}
\boldsymbol{b}_{rr_{k}} = \left\{ \right. & \frac{E \cdot (v \cdot \Delta r - 2 \cdot r_k \cdot (1-v))}{2 \cdot r_k \cdot \Delta r \cdot (1-v-2\cdot v^2)}, \frac{E \cdot (v \cdot \Delta r + 2 \cdot r_k \cdot (1-v))}{2 \cdot r_k \cdot \Delta r \cdot (1-v-2\cdot v^2)}, \\[1.5em]
& \frac{E \cdot v}{24 \cdot \Delta\varphi \cdot r_k \cdot (1-v-2\cdot v^2)}, -\frac{9 \cdot E \cdot v}{8 \cdot \Delta\varphi \cdot r_k \cdot (1-v-2\cdot v^2)}, \\[1.5em]
& \frac{9 \cdot E \cdot v}{8 \cdot \Delta\varphi \cdot r_k \cdot (1-v-2\cdot v^2)}, -\frac{E \cdot v}{24 \cdot \Delta\varphi \cdot r_k \cdot (1-v-2\cdot v^2)}, \\[1.5em]
& \frac{E \cdot v}{24 \cdot \Delta z \cdot (1-v-2\cdot v^2)}, -\frac{9 \cdot E \cdot v}{8 \cdot \Delta z \cdot (1-v-2\cdot v^2)}, \\[1.5em]
& \frac{9 \cdot E \cdot v}{8 \cdot \Delta z \cdot (1-v-2\cdot v^2)}, -\frac{E \cdot v}{24 \cdot \Delta z \cdot (1-v-2\cdot v^2)} \left. \right\}^{T}
\end{aligned}
\tag{A.10}
$$

A.4 Shutter control

To choose between the laser beams, three shutters are used in the setup for blocking the ray paths. Therefore, dull black anodized aluminum plates are attached to the ends of lifting magnets (Farnell Keyswitch Lifting Magnet SM00 12VDC). The shutters (S1 to S3) are controlled via the serial interface, which can be controlled with LabView. Two pins of the serial interface can be easily actuated by changing the output from 0 to 5V. These are *Data Terminal Ready* (DTR, pin 4) and *Request to Send* (RTS, pin 7). In addition to the three beams, an adjustment case is also implemented, where all ray paths are patched-through. This yields four states that can be selected with a logical combination of the two programmable pins according to the following table.

DTR	RTS	OPEN
0	0	S1
1	0	S2
0	1	S3
1	1	S1 / S2 / S3

Table A.3: Logic table for the four states to choose between the three laser beams

The circuit diagram of the shutter control is shown in Fig. A.1. For the logical operations two digital integrated circuits (IC) are used, one with inverters (Motorola MC14049B, Hex Inverter/Buffer) and one with logical NAND gates (Motorola MC14011B, Quad 2-Input NAND Gate). The 12V lifting magnets are driven with a high-voltage, high-current darlington array (SGS-Thomson ULN2004A). To enable the adjustment of the mirrors without running LabView, a manually operated switch opens all shutters. Three LEDs indicate the status of the shutters.
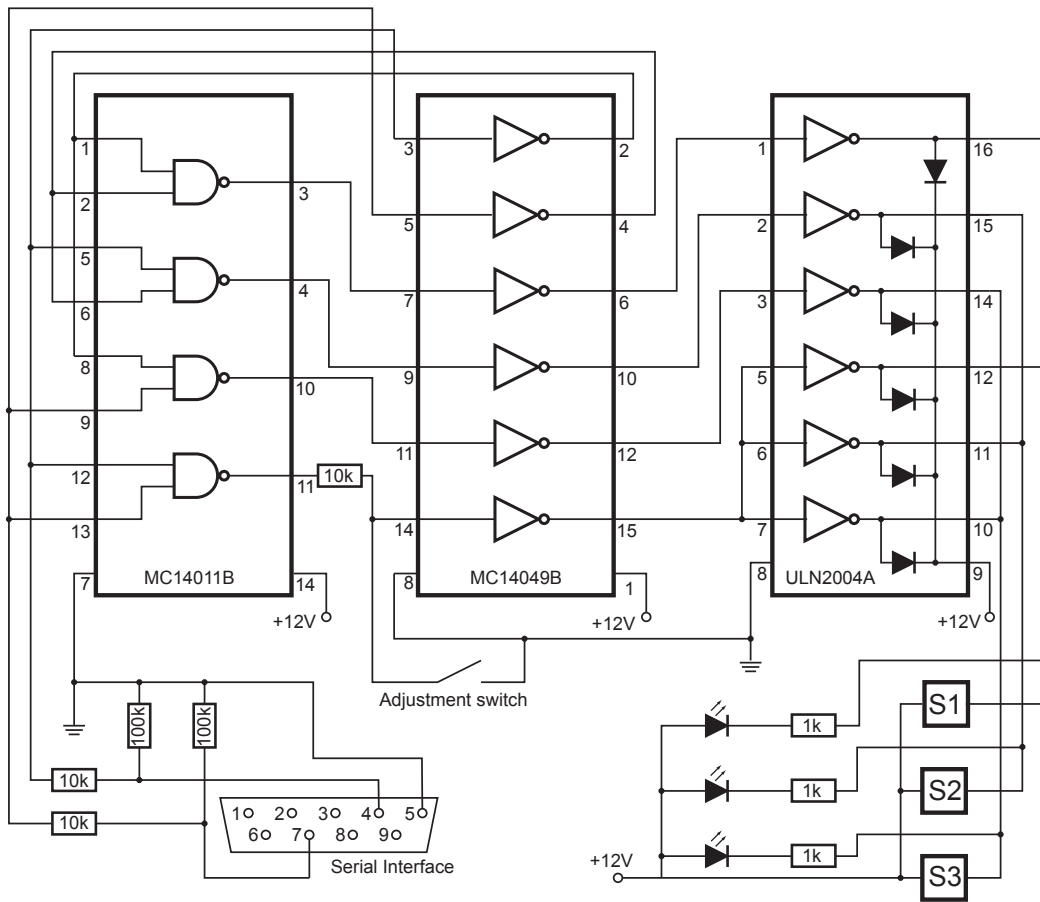
Figure A.1: Circuit diagram of the self-made shutter control.

A.5 Positioning of the optical components

To avoid or minimize the time-consuming auto-focussing of the laser, the three beams must have equal length. The distance a from the beamsplitter BS1 to the surface of the object and the angles α, β, and γ can be chosen. The three-dimensional diagram, side elevation and plan view are shown in Fig. A.2. In the present approach the values $a = 20\,\text{cm}$, $\alpha = 41°$, $\beta = 35°$, and $\gamma = 37°$ are used. The distance b between the beamsplitter BS1 and the mirror M1, and the gap c between the two beamsplitters are the parameters that need to be adjusted properly in order to ensure consistent lengths of the ray paths.
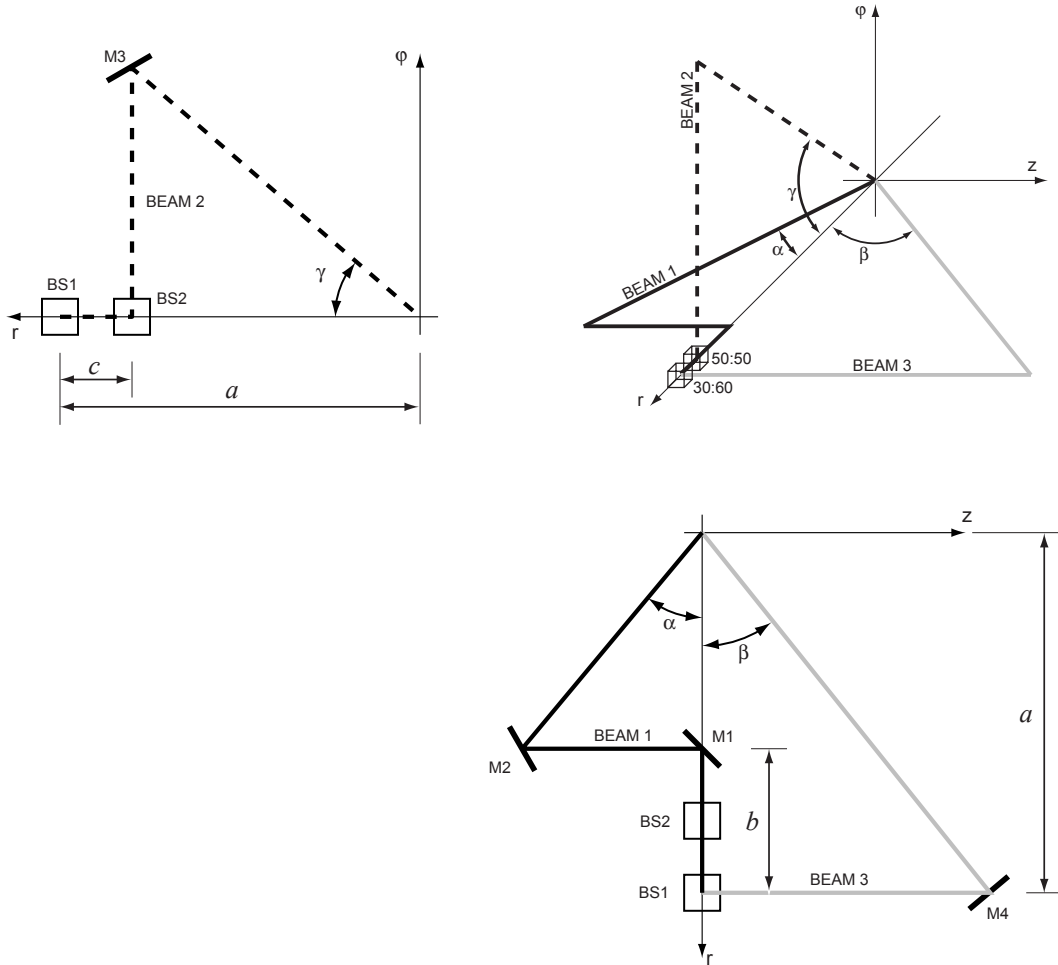
Figure A.2: Positioning of the optical components to achieve equal ray path length for beam 1 (solid black), beam 2 (dashed black), and beam 3 (solid gray). The side elevation (upper left) and the plan view (lower right) of the three-dimensional (upper right) diagram are shown.

They are calculated as

$$b = \frac{tan\beta + \dfrac{1}{cos\beta} - tan\alpha - \dfrac{1}{cos\alpha}}{1 - tan\alpha - \dfrac{1}{cos\alpha}} \cdot a \tag{A.11}$$

$$c = \frac{tan\beta + \dfrac{1}{cos\beta} - tan\gamma - \dfrac{1}{cos\gamma}}{1 - tan\gamma - \dfrac{1}{cos\gamma}} \cdot a \tag{A.12}$$

A.6 Experimental determination of the angles

To calculate the displacement components in radial, circumferential, and axial directions [Eqs. (4.2) - (4.4)], the angles α, β, and γ must be known. Since the exact distances between the optical components are difficult to determine, the three angles are measured directly. For this purpose, a sheet of millimeter paper is mounted parallel to the φ,z-plane on a translation stage, moving into the r-direction. The plane with the paper is positioned and aligned between the optical setup and the sample, and all shutters are opened. Fig. A.3 shows the setup and the paper sheet at two different positions (plane E and F).
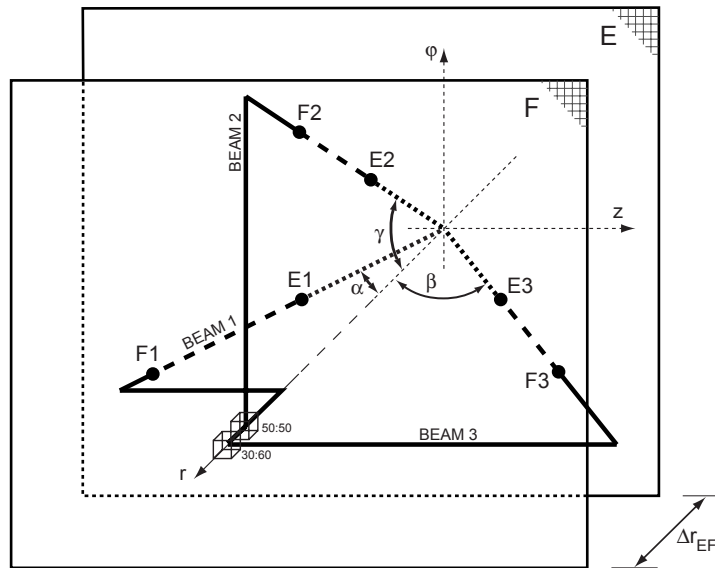

Figure A.3: Setup to determine the three angles. A sheet of millimeter paper is positioned between the laser beams and the sample at two different locations (plane E and F), and the points of intersection are marked on the paper (E1, E2, E3, F1, F2, F3).

At the first location (plane E), the positions where the three laser beams hit the plane are marked on the millimeter paper (points E1, E2, and E3). Then, the sheet is moved into the radial direction by the distance Δr_{EF} using the translation stage (plane F). Again, the locations of the intersection points are marked on the same sheet (F1, F2, and F3). Fig. A.4 shows the millimeter paper with the marked intersection points.
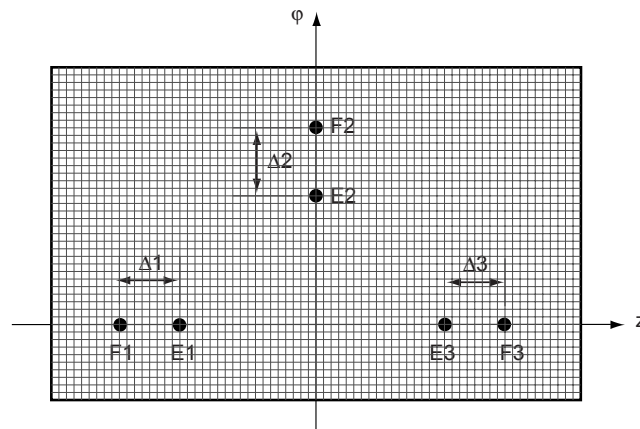

Figure A.4: Millimeter sheet with the marked intersection points of plane E (E1, E2, and E3) and plane F (F1, F2, and F3).

The distances $\Delta 1$, $\Delta 2$, and $\Delta 3$ are measured on the millimeter paper. With the known geometry shown in the two views in Fig. A.5 and the distance Δr_{EF} between the two planes E and F, the three angles can be calculated.
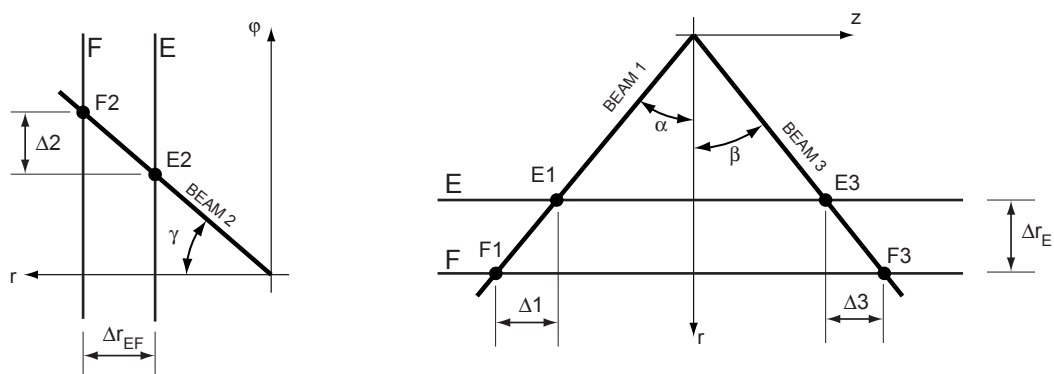
Figure A.5: Side elevation (left) and plan view (right) to determine the angles α, β, and γ from the measured distances.
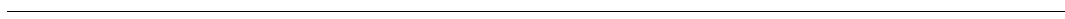
BIBLIOGRAPHY

[1]   Alleyne, D.N., Lowe, M.J.S., and Cawley, P., *The reflection of guided waves from circumferential notches in pipes*, Journal of Applied Mechanics, 65(3), 635-641, 1998.

[2]   Alleyne, D.N., Cawley, P., Lank, A.M., and Mudge, P.J., *The lamb wave inspection of chemical plant pipework*, Review of Progress in Quantitative Nondestructive Evaluation, 16, 1269-1276, 1997.

[3]   Bar-Cohen, Y., *Emerging NDT technologies and challenges at the beginning of the third millennium, part 1 & 2*, Materials Evaluation, 58(1), 17-30, and 58(2), 141-150, 2000.

[4]   Bathe, K.J., *Finite element procedures*, Prentice-Hall Inc., Englewood Cliffs, New Jersey, 1996.

[5]   Berenger, J.P., *A perfectly matched layer for the absorption of electromagnetic waves*, Journal of Computational Physics, 114(2), 185-200, 1994.

[6]   Chen, Y.-H., and Chew, W.C., *A three-dimensional finite-difference code for the modeling of sonic logging tools*, Journal of the Acoustical Society of America, 103(2), 702-712, 1998.

[7]   Dablain, M.A., *The application of higher-order differencing to the scalar wave equation*, Geophysics, 51(1), 54-66, 1986.

[8]   Derode, A., Roux, P., and Fink, M., *Robust acoustic time reversal with high-order multiple scattering*, Physical Review Letters, 75(23), 4206-4209, 1995.

[9] Ditri, J., *Utilization of guided elastic waves for the characterization of circumferential cracks in hollow cylinders*, Journal of the Acoustical Society of America, 96(6), 3769-3775, 1994.

[10] Dual, J., *Experimental methods in wave propagation in solids and dynamic viscometry*, Diss. ETH No. 8659, Zürich, 1988.

[11] Dual, J., Hägeli, M., Pfaffinger, M.R., and Vollmann, J., *Experimental aspects of quantitative nondestructive evaluation using guided waves*, Ultrasonics, 34, 291-295, 1996.

[12] Dual, J., Sayir, M., Winkler, A., and Staudenmann, M., *Nondestructive evaluation of defects in beams by guided waves*, in Elastic Waves and Ultrasonic Nondestructive Evaluation, Datta, S.K., et al., 191-196, North-Holland, Amsterdam, 1990.

[13] Fellinger, P., Marklein, R., Langenberg, K.J., and Klaholz, S., *Numerical modeling of elastic wave propagation and scattering with EFIT - elastodynamic finite integration technique*, Wave Motion, 21(1), 47-66, 1995.

[14] Fink, M., *Time reversal in acoustics*, Contemporary Physics, 37(2), 95-109, 1996.

[15] Fink, M., *Time-reversed acoustics*, Scientific American, 281(5), 91-97, 1999.

[16] Fink, M., Cassereau, D., Derode, A., Prada, C., Roux, P., Tanter, M., Thomas, J.-L., and Wu, F., *Time-reversed acoustics*, Reports on Progress in Physics, 63(12), 1933-1995, 2000.

[17] Ganzha, V.G., and Vorozhtsov, E.V., *Computer-aided analysis of difference schemes for partial differential equations*, John Wiley & Sons Inc., New York, 1996.

[18] Gazis, D.C., *Three-dimensional investigation of the propagation of waves in hollow circular cylinders. I. Analytical foundation. II. Numerical results*, Journal of the Acoustical Society of America, 31(5), 568-578, 1959.

[19] Goodbread, J., *Mechanical properties of spongy bone at low ultrasonic frequencies*, Diss. ETH No. 5856, Zürich, 1976.

[20] Graff, K.F., *Wave motion in solids*, Oxford University Press, London, 1975.

[21] Graves, R.W., *Simulating seismic wave propagation in 3D elastic media using staggered-grid finite-differences*, Bulletin of the Seismological Society of America, 86(4), 1091-1106, 1996.

[22] Gsell, D., *Nicht axialsymmetrische Wellenausbreitung in anisotropen zylindrischen Strukturen*, Diss. ETH No.14733, Zürich, 2002.

[23] Gsell, D., Leutenegger, T., and Dual, J., *Modeling three-dimensional elastic wave propagation in circular cylindrical structures using a finite-difference approach*, submitted to Journal of the Acoustical Society of America, March 2001.

[24] Harker, A.H., *Numerical modelling of the scattering of elastic waves in plates*, Journal of Nondestructive Evaluation, 4(2), 89-106,1984.

[25] Higdon, R.L., *Absorbing boundary conditions for difference approximations to the multi-dimensional wave equations*, Mathematics of Computation, 47(176), 437-459, 1986.

[26] Ing, R.K., and Fink, M., *Time recompression of dispersive lamb waves using a time reversal mirror - application to flaw detection in thin plates*, IEEE Ultrasonics Symposium Proceedings, 1, 659-663, 1996.

[27] Lax, P.D., and Ritchmyer, R.D., *Survey of the stability of linear finite-difference equations*, Communications on Pure and Applied Mathematics, 9, 267-293, 1956.

[28] Leutenegger, T., and Dual, J., *Detection of defects in cylindrical structures using a time reverse method and a finite-difference approach*, Ultrasonics, 40, 721-725, 2002.

[29] Leutenegger, T., Schlums, D.H., and Dual, J., *Structural Testing of Fatigued Structures,* Proceedings of Smart Structures and Integrated Systems, SPIE 3668(2), 987-997, Newport Beach, California, 1-5 March 1999.

[30] Liao, Z.P., Wong, H.L., Yang, B., and Yuan, Y., *A transmitting boundary for transient wave analysis*, Scientia Sinica, Series A, 27(10), 1063-1076, 1984.

[31] Lindman, E.L., *"Free-space" boundary conditions for the time dependent wave equation*, Journal of Computational Physics, 18, 66-78, 1975.

[32] Lowe, M.J.S., Alleyne, D.N., and Cawley, P., *Defect detection in pipes using guided waves*, Ultrasonics, 36(1-5), 147-154, 1998.

[33] Madariaga, R., *Dynamics of an expanding circular fault*, Bulletin of the Seismological Society of America, 66(3), 639-666, 1976.

[34] Marklein, R., *Numerische Verfahren zur Modellierung von akustischen, elektromagnetischen, elastischen und piezoelektrischen Wellenausbreitungsproblemen im*

Zeitbereich basierend auf der Finiten Integrationstechnik, Shaker Verlag, Aachen, 1997.

[35] Meitzler, A.H., *Mode coupling occurring in propagation of elastic pulses in wires*, Journal of the Acoustical Society of America, 33(4), 435-445, 1961.

[36] Mindlin, R.D., *Influence of rotatory inertia and shear on flexural motions of isotropic, elastic plates*, Journal of Applied Mechanics, 18, 31-38, 1951.

[37] Mohr, W., and Höller, P., *On inspection of thin-walled tubes for transverse and longitudinal flaws by guided ultrasonic waves*, IEEE Transactions on Sonics and Ultrasonics, 23(5), 369-374, 1976.

[38] Nelson, R.B., Dong, S.B., and Kalra, R.D., *Vibrations and waves in laminated orthotropic circular cylinders*, Journal of Sound and Vibration, 18(3), 429-444, 1971.

[39] Qian, S., and Chen, D., *Joint time-frequency analysis*, Prentice-Hall Inc., Upper Saddle River, New Jersey, 1996.

[40] Rose, J.L., *Ultrasonic waves in solid media*, Cambridge University Press, Cambridge, 1999.

[41] Rose, J.L., *Standing on the shoulders of giants: an example of guided wave inspection*, Materials Evaluation, 60(1), 53-59, 2002.

[42] Rose, J.L., Ditri, J.J., Pilarski, A., Rajana, K., and Carr, F., *A guided wave inspection technique for nuclear steam generator tubing*, NDT&E International, 27(6), 307-310, 1994.

[43] Schubert, F., Pfeiffer, A., and Köhler, B., *The elastodynamic finite integration technique for waves in cylindrical geometries*, Journal of the Acoustical Society of America, 104(5), 2604-2614, 1998.

[44] Shin H.J., and Rose, J.L., *Guided wave tuning principles for defect detection in tubing*, Journal of Nondestructive Evaluation, 17(1), 27-36, 1998.

[45] Shlager, K.L., Maloney, J.G., Ray, S.L., and Peterson, A.F., *Relative accuracy of several finite-difference time-domain methods in two and three dimensions*, IEEE Transactions on Antennas and Propagation, 41(12), 1732-1737, 1993.

[46] Shlager, K.L., and Schneider, J.B., *A selective survey of the finite-difference time-domain literature*, IEEE Antennas and Propagation Magazine, 37(4), 39-56, 1995.

[47] Silk, M.G., and Bainton, K.F., *The propagation in metal tubing of ultrasonic wave modes equivalent to Lamb waves*, Ultrasonics, 17, 11-19, 1979.

[48] Strang, G., and Nguyen, T., *Wavelets and filter banks*, Wellesley-Cambridge Press, Wellesley, Massachusetts, 1996.

[49] Strauss, W.A., *Partial differential equations - an introduction*, John Wiley & Sons Inc., New York, 1992.

[50] Strikwerda, J.C., *Finite-difference schemes and partial differential equations*, CRC Press LLC, Florida, 1999.

[51] Taflove, A., *Computational electrodynamics - the finite-difference time-domain method*, Artech House Inc., Norwood, 1995.

[52] Temple, J.A.G., *Modelling the propagation and scattering of elastic waves in inhomogeneous anisotropic media*, Journal of Physics D: Applied Physics, 21, 859-874, 1988.

[53] Thompson, R.B., *Physical principles of measurements with EMAT transducers*, in Ultrasonic Measurement Methods, Thurston, R.N., and Pierce, A.D., 157-200, Academic Press, Boston, 1990.

[54] Virieux, J., *SH-wave propagation in heterogeneous media: velocity-stress finite-difference method*, Geophysics, 49(11), 1933-1957, 1984.

[55] Virieux, J., *P-SV wave propagation in heterogeneous media: velocity-stress finite-difference method*, Geophysics, 51(4), 889-901, 1986.

[56] Vollmann, J., *Wave propagation in viscoelastic and anisotropic, cylindrical structures*, Diss. ETH No. 11762, Zürich, 1996.

[57] Weaver, W., and Johnston, P.R., *Structural dynamics by finite elements*, Prentice-Hall Inc., Englewood Cliffs, New Jersey, 1987.

[58] Weisweiler F.J., and Sergeev, G.N., *Non-destructive testing of large-diameter pipe for oil and gas transmission lines*, VCH Verlagsgesellschaft, D-Weinheim, 1987.

[59] Yee, K.S., *Numerical solution of initial boundary value problems involving Maxwell's equations in isotropic media*, IEEE Transactions on Antennas and Propagation, 40(3), 302-307, 1966.
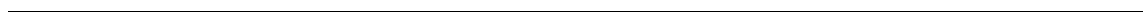
CURRICULUM VITAE

Tobias Fortunat Leutenegger

Born on May 7, 1971 in Basel, Switzerland
Citizen of Switzerland

1998 - 2002	Doctoral student, research and teaching assistant at the Institute of Mechanical Systems (formerly Institute of Mechanics) of the ETH Zürich
2001	Awarded the RWB Stephens Student Prize at the Ultrasonics International Conference, Delft, The Netherlands, July 2001
May 1995 - Jan. 1996	Practical training at Synthes (USA), Exton, USA
May 1994 - Feb. 1998	Tutoring assistant at the Institute of Mechanical Systems (formerly Institute of Mechanics) of the ETH Zürich
1992 - 1998	Studies at the Mechanical Engineering Department of the Swiss Federal Institute of Technology ETH, Zürich, Switzerland. Graduation with honors with the degree Dipl. Masch.-Ing. ETH
1984 - 1991	Kantonsschule Chur, Switzerland. Graduation with a matura, type C
1978 - 1984	Primary school in Münchenstein/BL, Trimmis/GR, and Chur/GR, Switzerland